TESTS OF TWO, ASPECT RATIO 6, HYDROFOILS AT REYNOLDS NUMBERS FROM 0.8×10^5 TO 2.69×10^5

LAWRENCE F. HICKS
AND
WILBUR J. MAHONY

TESTS OF TWO, ASPECT RATIO 6, HYDROFOILS AT REYNOLDS NUMBERS FROM 0.8×10^5 TO 2.69×10^5

****

A THESIS SUBMITTED TO THE
FACULTY OF WEBB INSTITUTE OF NAVAL ARCHITECTURE
IN PARTIAL FULFILLMENT OF
THE REQUIREMENTS FOR A DEGREE OF MASTER OF SCIENCE
IN NAVAL ARCHITECTURE

****

BY
LT. LAWRENCE F. HICKS, USN
AND
LT. WILBUR J. MAHONY, USN

****

9 JUNE 1958

ACKNOWLEDGEMENTS

The authors are very much indebted to Professor Cedric Ridgely-Nevitt for his patient and sincere interest and many valuable suggestions during both the testing and analytical phases of this thesis.

The authors wish to thank the research engineers of the Hydrodynamics Division of the Langley Laboratory of the National Advisory Committee for Aeronautics for their helpful technical suggestions and patient explanations of the major portion of the theory on which the predictions included in the thesis are based.

The authors are also indebted to Lt. D.L. Soracco for his foresight and attention to detail in designing and constructing the balance used to conduct these tests. Mr. Duncan Robb offered innumerable suggestions regarding shop practices, which saved the authors many hours during the balance modification phase.

Grateful acknowledgement is also given to the David Taylor Model Basin for providing at no small expense the two hydrofoils and strut assembly which served as test vehicles for this investigation.

TABLE OF CONTENTS

INTRODUCTION

It has been known for some time that laminar flow and subsequent laminar separation have a marked effect on the performance of an airfoil. For this reason wind tunnel experiments have, as much as possible, carefully avoided this phenomenon. This procedure has produced a very meager amount of airfoil data below a Reynolds number of 10^6. The wind tunnel experimenter is, of course, justified in his choice since he thereby employs the best capabilities of his test equipment.

The ship model experimenters are not so fortunate. The laws of similitude make avoidance of the low Reynolds number range almost impossible. This is particularly true with respect to the self propelled ship model test, which though often criticized, remains a singularly important tool in the prediction of the performance of the full size ship. One of the key problems in this test is the performance of the propeller when operating behind the model. The laws of similitude dictate its speed of advance, diameter and RPM. Therefore the propeller Reynolds number is fixed. However, the performance of the propeller is often predicted by tests conducted at much higher Reynolds numbers. This fact becomes important when we remember that the model propeller is used as an instrument to measure the effects of the model hull on flow in the region of the propeller.

Since most of the self propelled model tests to date have been run on models of about 20 foot length, the following table will give some average values for representative ship types.

Ship Type	Reynolds Number at 0.7 Radius*
Battleship	1.17×10^6
Cruiser	1.425×10^6
Carrier	$.905 \times 10^6$
Destroyer	1.11×10^6
Submarine	$.915 \times 10^6$
Series 60 (C_b=.60)	$.249 \times 10^6$

*This represents a good average value over the propeller.

Furthermore, for a given propeller there is a variation in Reynolds number from root to tip for a constant RPM and model speed. As an example of this variation, values were calculated over the blade of the Troost propeller used in the Series 60 tests. (Ref. 17) These data also apply to a 20 foot model operating at design speed with the propeller operating at design RPM.

Series 60 Troost Propeller

Location of Section	Reynolds Number
0.2 Rad.	$.913 \times 10^5$
0.4 Rad.	1.560×10^5
0.6 Rad.	2.25×10^5
0.7 Rad.	2.49×10^5
0.8 Rad.	2.57×10^5
0.9 Rad.	2.30×10^5

In the past few years attempts have been made to conduct tests on self propelled models of the order of 10 feet or less in length. Tests at Stevens Institute on the "San Francisco" show propeller Reynolds numbers as low as 5.6×10^4. (Ref. 18)

There are a variety of opinions as to the point at which laminar separation becomes a serious problem. Some expert opinions indicate a value of about 3.5×10^5 for model propellers. Experimental data for airfoil shapes however, indicate that it occurs as high as a value of 10^6. Since separation is as much a function of the geometry of the bodies as the Reynolds number, it seems unlikely that it can be fixed exactly. If we accept 10^6 as a possibility, then a glance at the table of model propeller Reynolds numbers will reveal that all of these propellers might be affected to some degree by laminar separation.

Since the airfoil and propeller are so closely linked in concept and performance, it seemed that the first logical step toward finding the effects of laminar separation on propeller performance would be to study its effect on airfoil performance. Moreover, since this problem is more closely associated with the hydrodynamics of ship models, it seemed proper to move one step closer to the problem by testing hydrofoils.

The desired Reynolds number range imposes two requirements on the test hydrofoil. First it must be small and second it must operate at low speeds. Both of these requirements lead to small forces, and consequently a special test instrument is needed. This instrument, the Two Component Balance, was designed and built at Webb Institute to fulfill thesis requirements for a M.S. degree. The following test series is the first to utilize this balance.

The applications of these tests are not restricted to the model propeller field. Ship models have many appendages, all of which are to some degree subject to low Reynolds number effects. Examples would be rudders, bilge keels, shaft strut arms, stabilizing fins, anti-pitch fins, and submarine control planes. For example, the rudder of a 20 foot model in a turning test might well operate at a Reynolds number of 2×10^5.

The Reynolds number range covered in this test series is $.8 \times 10^5$ to 2.69×10^5. It was hoped this range could be extended up to about 10^6, however, certain physical limitations made this impossible. It is interesting to note that the test range fully covers the Series 60 propeller. The large variations in foil performance over the Reynolds number range tested indicates that the problem of laminar separation is important and not one on mere academic interest.

GENERAL SYMBOLS

ρ Mass Density ($lb\text{-}sec^2/ft^4$)

ν Kinematic viscosity (ft^2/sec)

HYDRODYNAMIC SYMBOLS

C_l' Three dimensional measured lift coefficient. $C_l' = L'/\frac{1}{2}\rho SV^2$

C_l Three dimensional lift coefficient. $C_l = L/\frac{1}{2}\rho SV^2$. $C_l = C_l' \pm C_{ls}$

c_l Two dimensional lift coefficient.

C_{ls} Strut lift coefficient. $C_{ls} = L_s/\frac{1}{2}\rho SV^2$. Where S is based on the projected area of the foil when used to correct experimental data.

C_d' Three dimensional measured drag coefficient. $C_d' = D'/\frac{1}{2}\rho SV^2$.

C_d Three dimensional drag coefficient. $C_d = D/\frac{1}{2}\rho SV^2$. $C_d = C_d' - C_{ds}$.

c_d Two dimensional drag coefficient.

C_{ds} Strut drag coefficient. $C_{ds} = D_s/\frac{1}{2}\rho SV^2$. Where S is based on the projected area of the foil when used to correct experimental data. For the strut alone S is the projected area of the strut.

$C_{ds,w}$ Strut wavemaking drag coefficient. $C_{ds,w} = D_{s,w}/\frac{1}{2}\rho SV^2$.

C_{dp} Profile drag coefficient. C_{dp}(for strut) = $C_{ds} - C_{ds,w}$.

α_o Two dimensional angle of attack.

α Geometric angle of attack. $\alpha = \alpha' \pm \Delta\alpha_r$

α' Measured geometric angle of attack.

$\Delta\alpha_o$ Change in geometric angle of attack due to deflection of strut produced by the drag force.

$\Delta\alpha_L$ Change in measured geometric angle of attack due to strut deflection produced by the lift force.

$\Delta\alpha_T$ Total change in measured geometric angle of attack due to strut deflection. $\Delta\alpha_T = \Delta\alpha_D + \Delta\alpha_L$

D' Measured foil drag (lb)

D Foil drag (lb).

L' Measured foil lift (lb).

L Foil lift (lb).

D_S Strut drag (lb).

L_S Strut lift (lb).

V Free stream velocity, ft/sec. Also equal to the carriage speed.

S Projected area (ft^2).

c Chord (in)

s Semi - span (in)

A Aspect ratio. $A = (2s)^2/S$. $A = 2s/c$ for a rectangular foil.

f Depth of foil (in).

t Thickness (in)

R_c Reynolds number. $R_c = Vc/\gamma$. In this formula c is in ft.

I. APPARATUS AND TEST PROCEDURE

The test series was conducted in the Webb Towing Tank over the periods of 4 October 1957 to 12 December 1957 and 24 March 1958 to 6 May 1958. The test instrument was a special two component balance designed and built at Webb Institute for this purpose. For a complete description of the balance see reference 15 and Appendix II of this paper.

The tests were made on two similar, rectangular, aspect ratio 6 hydrofoils manufactured by the David Taylor Model Basin. The foils were machined from aluminum and polished to a smooth surface. The airfoil section used was the NACA 64-409 series. The foils had the following basic dimensions.

Large Foil	Small Foil
2s = 30 in.	2s = 18 in.
c = 5 in.	c = 3 in.
S = 150 sq. in.	S = 54 sq. in.

The two foils are hereafter identified as "Large foil" and "Small foil". For the table of offsets of the section see Appendix I.

The supporting strut has an ogival section with a chord of $1\frac{1}{2}$ inches and a thickness of 0.401 inches. The strut was raked at an angle of 16.167 degrees from a perpendicular to the nose-tail line of the foil. See Appendix I for a more detailed description of the strut and foil assembly.

The foils were tested over a speed range of 2 - 7 ft./sec. and an angle of attack range from +4 degrees to -2.5 degrees. Two factors limited the maximum testing speeds. The first was the physical strength of the balance. To prevent possible structural damage total lift forces were limited to 10 pounds. The second limitation was the strut spray roach

which impinged on the balance at high speeds and thus produced inaccurate drag measurements. As a result of these limitations the Reynolds number range covered was 0.8×10^5 to 2.7×10^5. This range includes both foils.

Since the Webb Towing Tank has an automatic water heating system all tests were conducted at the same water temperature of 80 degrees F. For this temperature the following values were used in all calculations.

$$\rho = 1.9336 \text{ lb-sec}^2/\text{ft}^4$$

$$\nu = 0.9296 \times 10^{-5} \text{ft./sec}^2$$

A more detailed listing of the accuracies of the balance can be found in Appendix III. Average values are:

Lift	±.005#
Drag	±.005#
Angle of Attack	± 0.10 degrees
Depth of Foil	± 0.10 inches

During testing at low speed, (2 ft/sec or less) drag forces of the order of magnitude of 0.05 pounds were measured. Since the accuracy of the balance is only 10% of this value, the authors feel that data taken at these low speeds are questionable.

No attempt was made to stimulate turbulence during any of the tests. The problem of stimulating turbulent flow on airfoils operating at low Reynolds numbers presents a very interesting basis for future investigations. Reference 16 presents some valuable investigations in the field.

II PRELIMINARY INVESTIGATIONS

Before the hydrofoils themselves could be tested, it was apparent that corrections for the effects of the supporting strut would have to be evaluated. Once the strut corrections were determined, they were used to correct the hydrofoil data to obtain foil characteristics divorced from strut influences. The corrections that were considered are:

1. The angular deflections of the support strut caused by hydrofoil lift and drag forces.
2. The strut lift and drag forces.
3. The strut interference with the flow around the hydrofoil.
4. The effect of the air resistance of the balance on drag readings.

1. Strut Deflection.

The angular deflections of the strut due to the hydrofoil lift and drag forces were measured in terms of angle of attack. Lift and drag forces were simulated by weights suspended at the foil position on the strut, with the strut support bracket clamped rigidly in a shop vice. Figure 1 is a presentation of the variation in angle of attack due to strut support deflections caused by hydrofoil lift and drag forces. The magnitude of this correction can be as large as one-half degree for combinations of lift and drag forces within the range tested.

2. Strut Lift and Drag

Strut lift and drag were determined by a series of tests varying speed from 2 to 7 feet per second and varying strut rake between values corresponding to foil angles of attack from -2.5° to $+4.0^{\circ}$. See figures 2, 3, 4 and 5 for photographs of the strut tests. The strut lift data is plotted

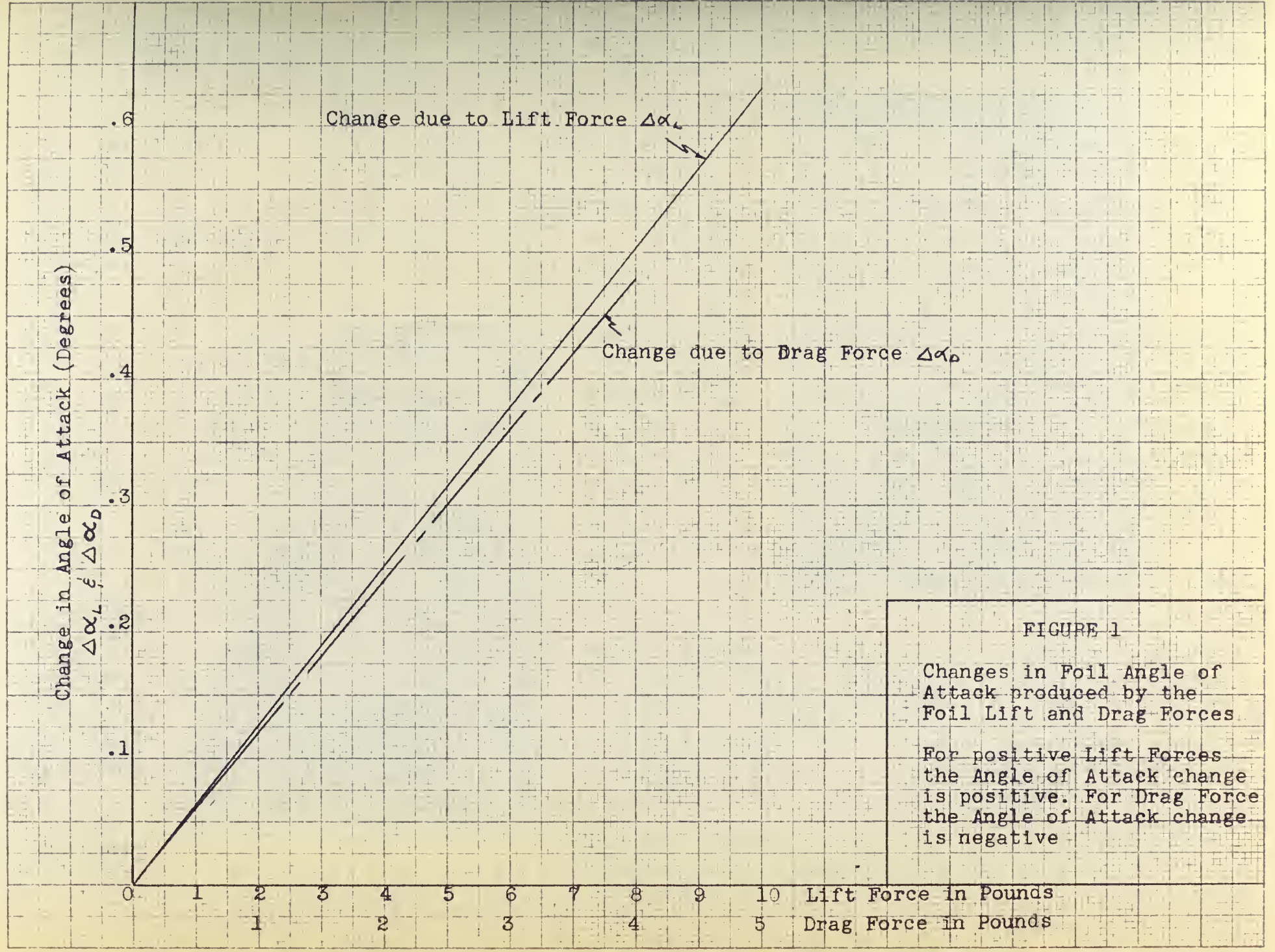

FIGURE 1

Changes in Foil Angle of Attack produced by the Foil Lift and Drag Forces

For positive Lift Forces the Angle of Attack change is positive. For Drag Force the Angle of Attack change is negative

Figure 2

Strut only: $\alpha' = 0°$,

Depth = 13.65",

V = 2'/sec.

Figure 3

Strut only: $\alpha' = 0°$,

Depth = 13.65",

V = 6'/sec.

Figure 4

Strut only: $\alpha' = 4^o$,

Depth = 13.65",

V = 4'/sec.

Figure 5

Strut only: $\alpha' = 4^o$,

Depth = 13.65",

V = 2'/sec.

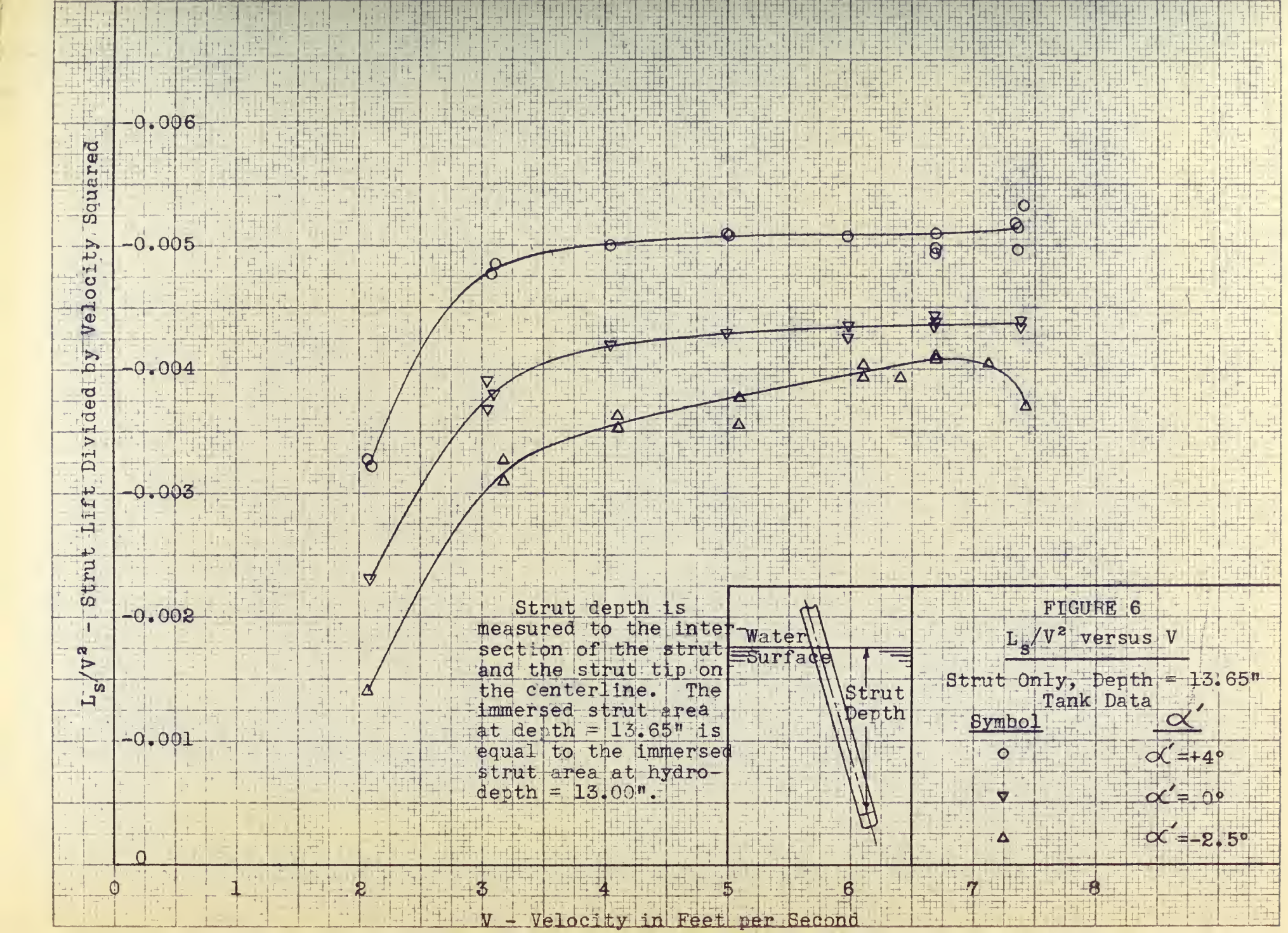
L_s/V^2 - Strut Lift Divided by Velocity Squared
-0.006
-0.005
-0.004
-0.003
-0.002
-0.001
0
0
1
2
3
4
5
6
7
8
V - Velocity in Feet per Second
Strut depth is measured to the intersection of the strut and the strut tip on the centerline. The immersed strut area at depth = 13.65" is equal to the immersed strut area at hydrodepth = 13.00".
Water Surface
Strut Depth
FIGURE 6
L_s/V^2 versus V
Strut Only, Depth = 13.65"
Tank Data
Symbol
α'
$\alpha' = +4°$
$\alpha' = 0°$
$\alpha' = -2.5°$

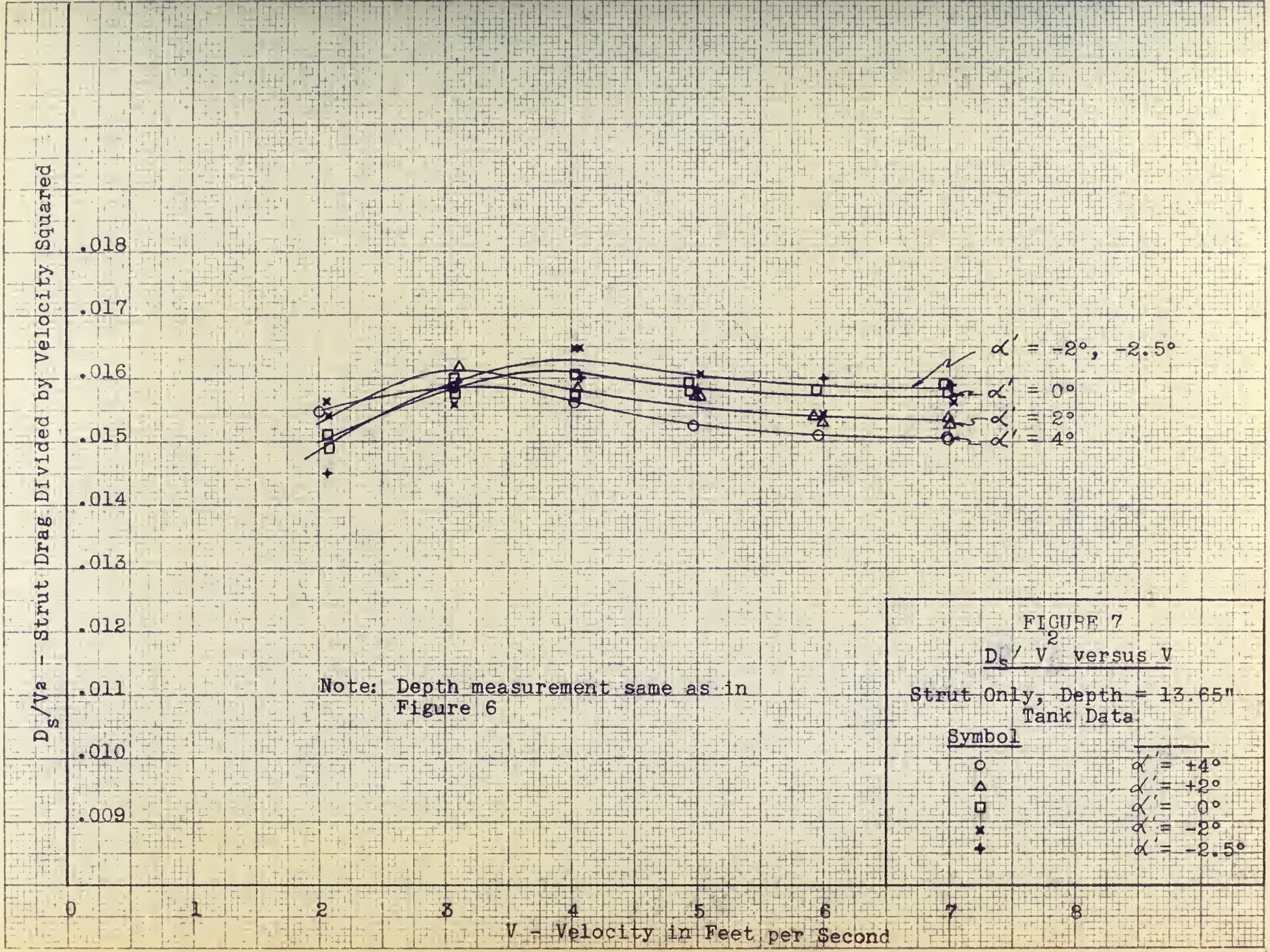

Note: Depth measurement same as in Figure 6

FIGURE 7

D_s/V^2 versus V

Strut Only, Depth = 13.65"
Tank Data

Symbol	
○	α' = +4°
△	α' = +2°
□	α' = 0°
×	α' = -2°
+	α' = -2.5°

as L_s/V^2 versus V in figure 6. The strut drag data is plotted as D_s/V^2 versus V in figure 7.

The quantities L_s/V^2 and D_s/V^2 were converted to strut lift and drag corrections by the multiplication factor $\frac{\rho}{2}S$:

$\frac{\rho}{2}S = 1.006$ for the large foil.

$\frac{\rho}{2}S = 0.362$ for the small foil.

See the sample calculations in Appendix I for an example of the use of these corrections. It should be noted that the strut lift correction represents a negative lift force. Since the strut was oriented with a forward rake over the entire range of angle of attack, the vertical component of the hydrodynamic force on the strut was directed down.

3. Interference Effects

Tests were conducted and reported in reference 5 on a strut in the presence of a 0.25 aspect ratio lifting surface. It was found that:

a. Interference of the strut on the drag of the lifting surface was negligible at all depths.

b. Interference on lift and pitching moment is negligible except at very shallow depths.

Since these tests were all conducted at deep submergence compared to the chord, no correction was considered necessary for strut interference effects.

4. Air Resistance.

A series of runs was made to evaluate the effect of the balance air resistance on the drag measurements. The maximum value of air drag divided by the square of the velocity was approximately 3% of the comparable para-

meter for the strut. For example, at the speed of 7 feet per second:

	Equivalent Drag	Drag / V^2
Air drag of balance	0.023#	0.47×10^{-3}
Strut drag	0.813#	16.3×10^{-3}

Therefore, at 7'/sec.:

$$\% \text{ Air Drag} = \frac{\text{Air drag coefficient}}{\text{Strut drag coefficient}} \times 100 = \frac{0.47}{16.3} \times 100 = 2.9\% \approx 3\%$$

Since the air drag of the balance was negligible compared to either strut or foil drag, no attempt was made to correct for air drag in this investigation. It should be noted, however, that since balance air drag is included in the strut drag data, the strut correction to the hydrofoil drag data automatically corrects for air drag.

Optimum Depth

While it may prove interesting to vary depth in future investigations, depth was held constant for the major portion of these tests. In order to determine an optimum depth for testing, however, a series of runs was conducted at constant speed and a constant angle of attack of approximately + 4.5°. These data are plotted in figure 8 as C_L' versus Depth. Since these particular data were obtained before balance modifications were complete and before an accurate testing procedure was developed, the data are only qualitative. The large foil maintained a constant C_L' over a range of depths greater than two chords, but the C_L' of the small foil varied over the entire range of depths. Since the variation of C_L' with depth decreased as the depth increased, a towing depth of 13 inches, measured to the mid-chord point, was selected. (See Figure 8.) This was the deepest depth practicable without alterations to the balance.

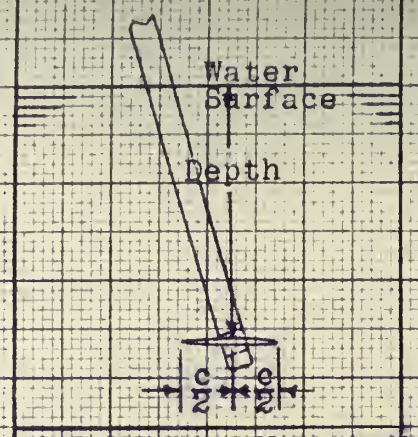

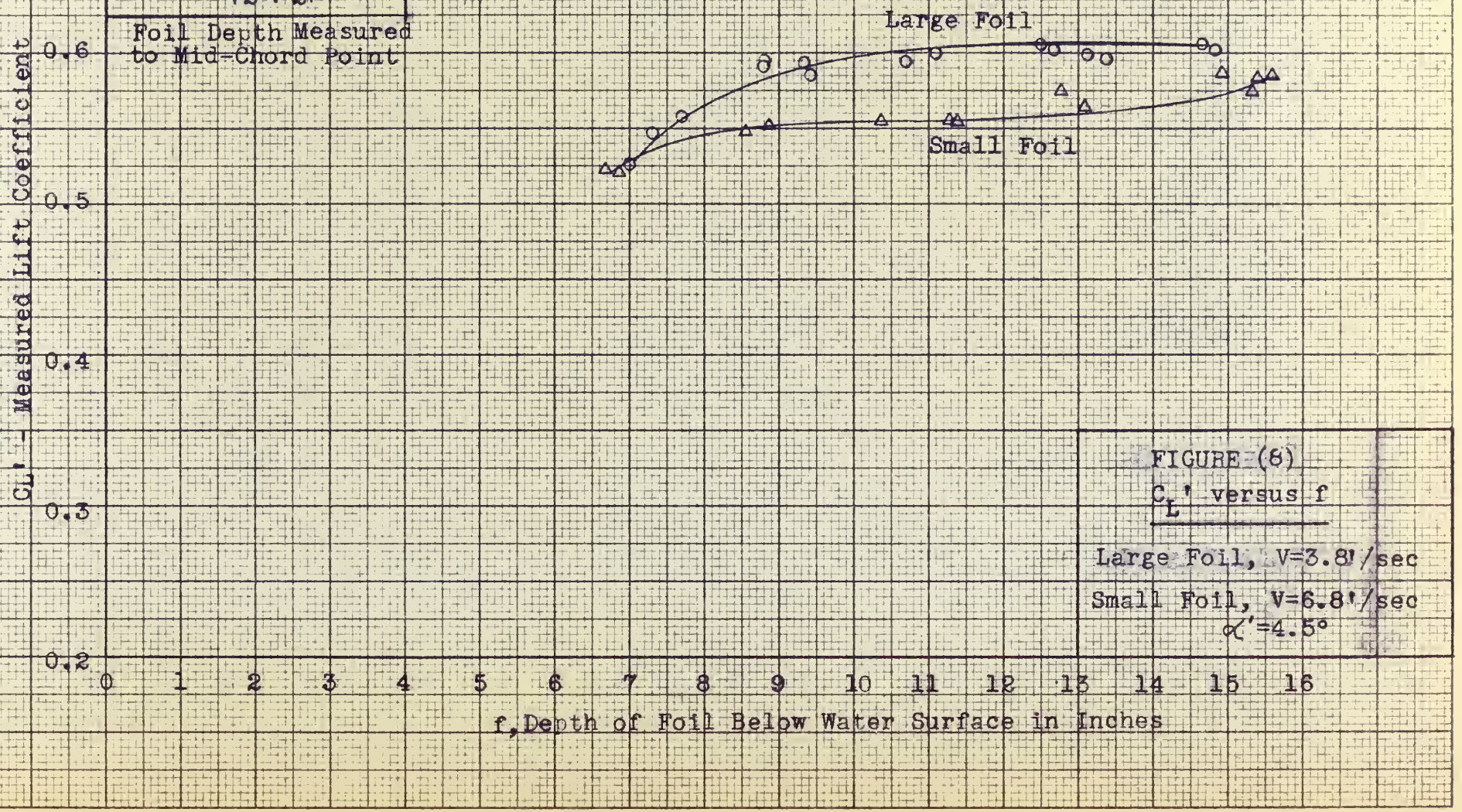

FIGURE (6)

C_L' versus f

Large Foil, V=3.8'/sec

Small Foil, V=6.8'/sec

$\alpha' = 4.5°$

III. EXPERIMENTAL RESULTS

As final data was plotted, it became more and more apparent that the hydrofoils were not conforming to conventional standards. For this reason, it was decided to first present the experimental data without embellishments and discuss its import and ramifications in more detail later.

Figures 9 through 14 are presented to illustrate the rough data as taken in the Model Tank. These figures are intended to be representative of the magnitude of experimental scatter in original data. In general, the small scatter obtained could be directly traced to the accuracy limits of the instrument. The form used to record and compute original data can be found in Appendix I. It is important to note that the faired rough data formed the basis for computation of all final results.

Of particular interest are Figures 13 and 14. In these tests the effect of Reynolds number on the lifting characteristics of the foils was graphically demonstrated. The lift coefficient for a set angle of attack ($\alpha = -2^\circ$) changed from positive to negative as the speed was lowered from 7 ft./sec. to 2 ft./sec.

To present the data in final form the rough data was corrected for strut lift and drag and strut deflections. A detailed example of these computations can be found in Appendix I. Final data plotted in standard form are found in Figures 15 through 20. A glance at these curves will reveal that Reynolds number effects have produced a radical departure from more conventional airfoil behavior. A more complete discussion of these departures will be made later.

Figures 21 through 26 are presented as examples of actual test runs. Figure 26 should give the reader a clearer picture of how the spray roach

from the strut can be a problem at high speeds. As speed increases, the spray height increases until it eventually strikes the flat plate supporting the strut. The authors noted changes in the tank wave pattern as produced by the strut and foil, as opposed to the strut alone. These visual observations, therefore, seemed to indicate that the hydrofoils were subject to some surface wavemaking effects.

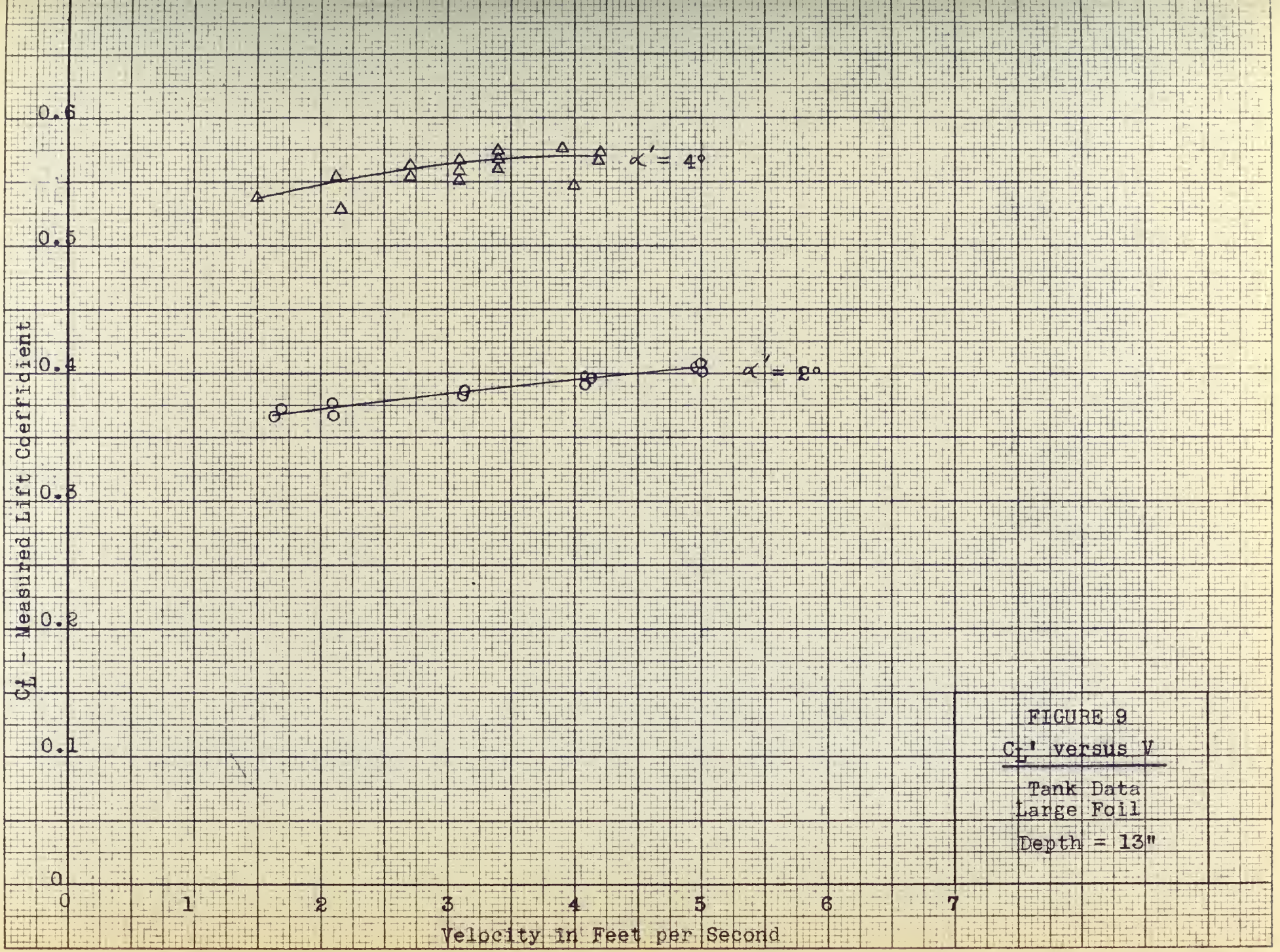

FIGURE 9

C_L' versus V

Tank Data
Large Foil
Depth = 13"

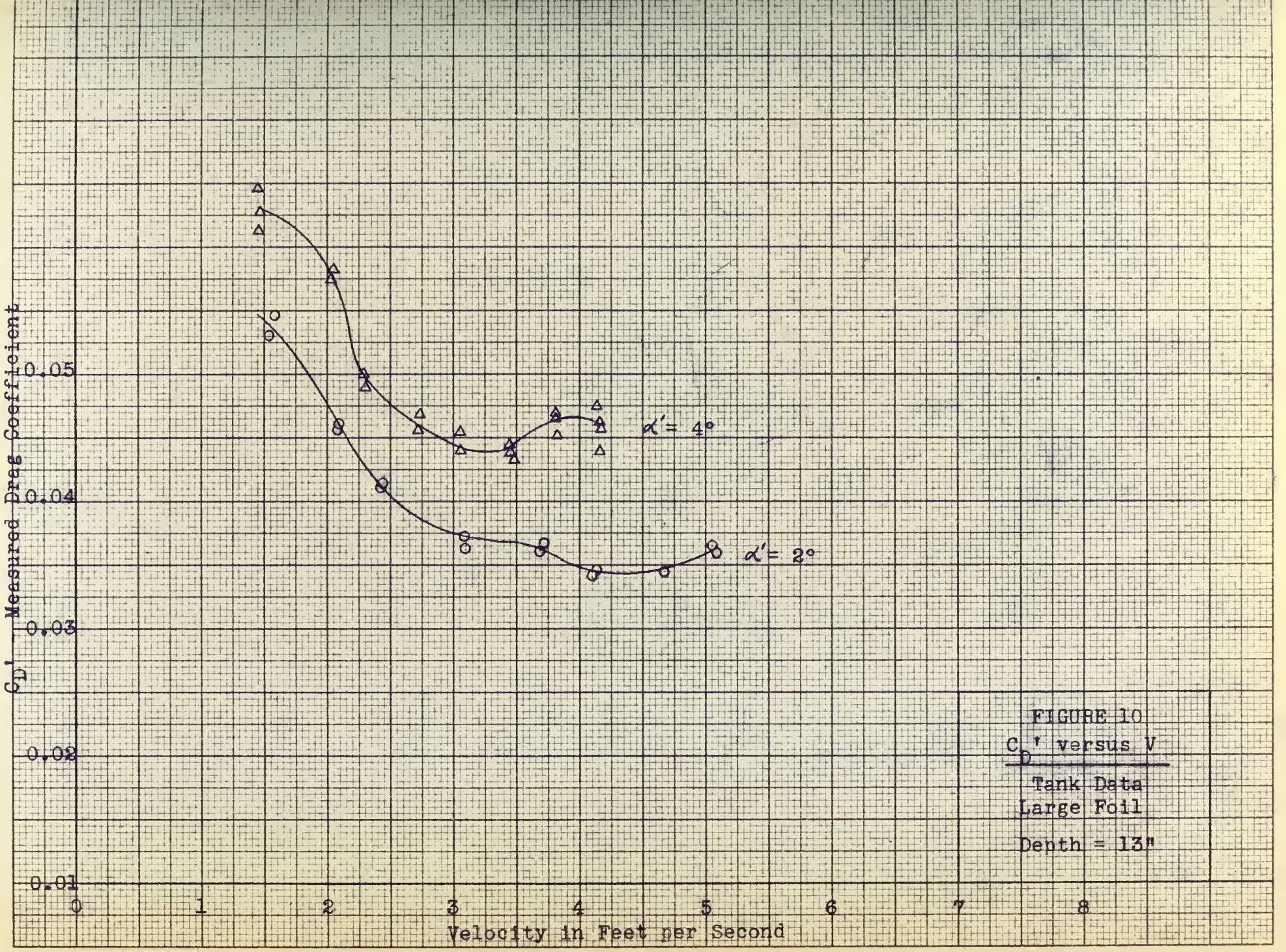

FIGURE 10

C_D' versus V

Tank Data

Large Foil

Depth = 13"

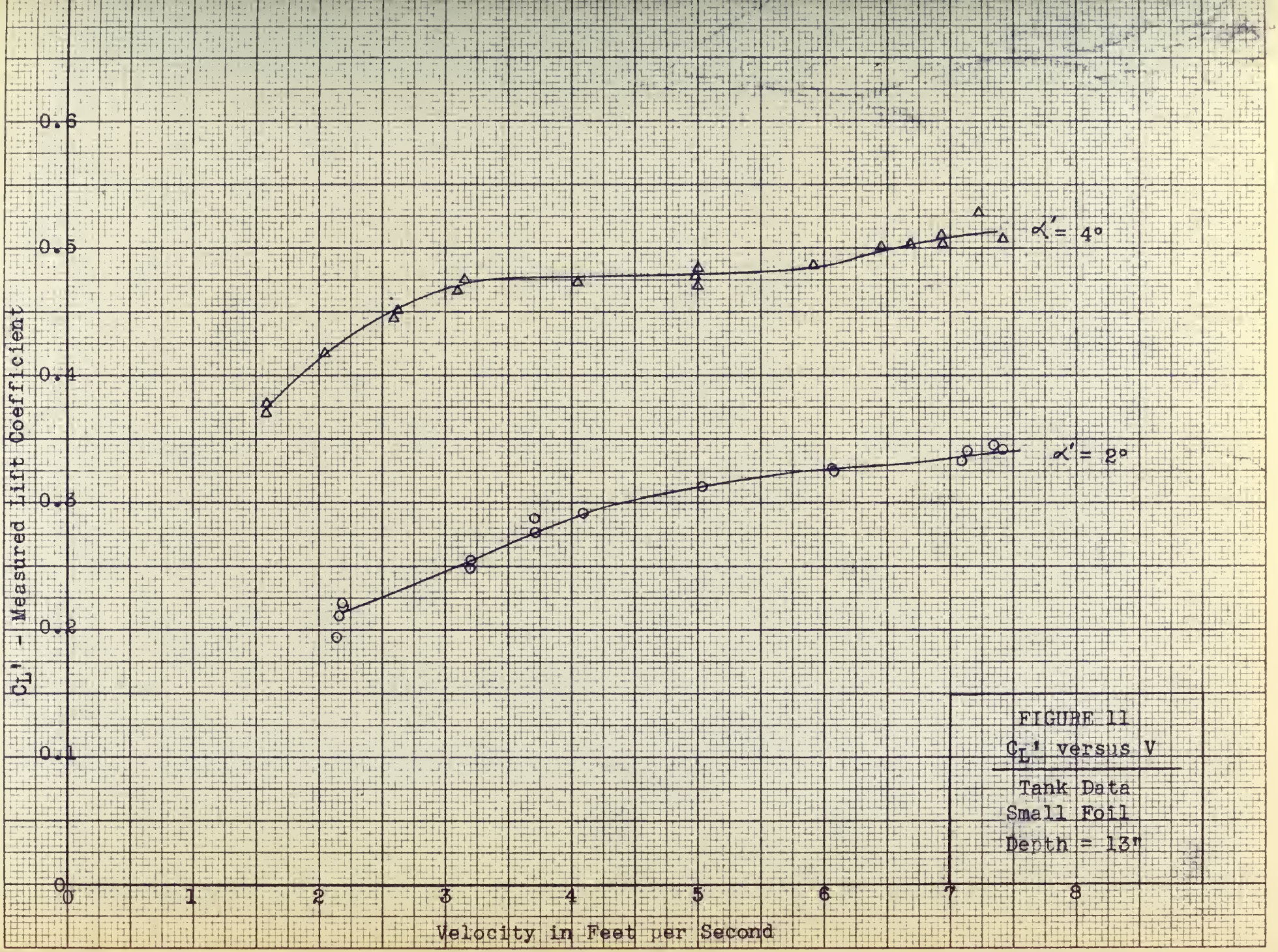

FIGURE 11
C_L' versus V

Tank Data
Small Foil
Depth = 13"

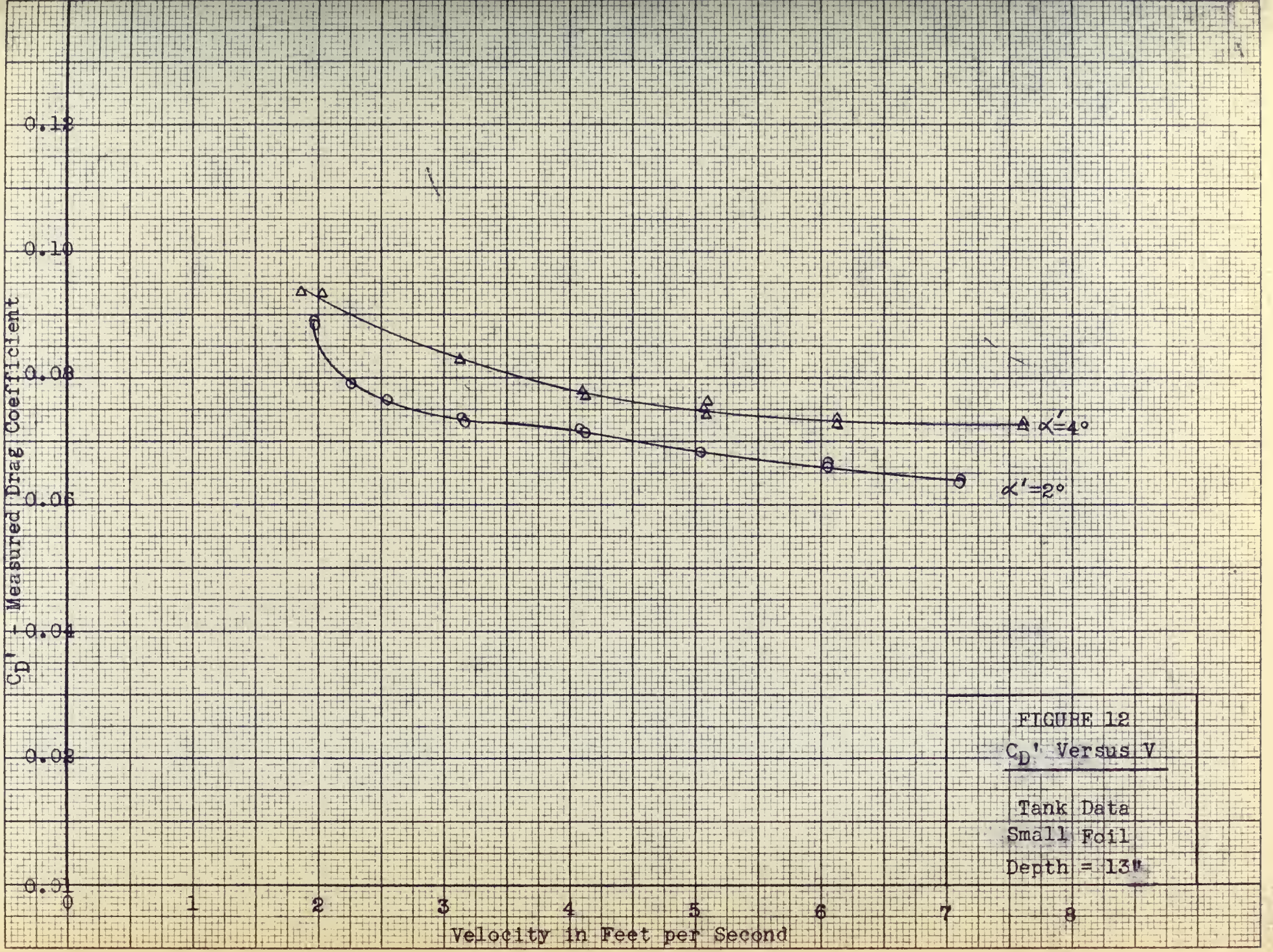

FIGURE 12

C_D' Versus V

Tank Data
Small Foil
Depth = 13"

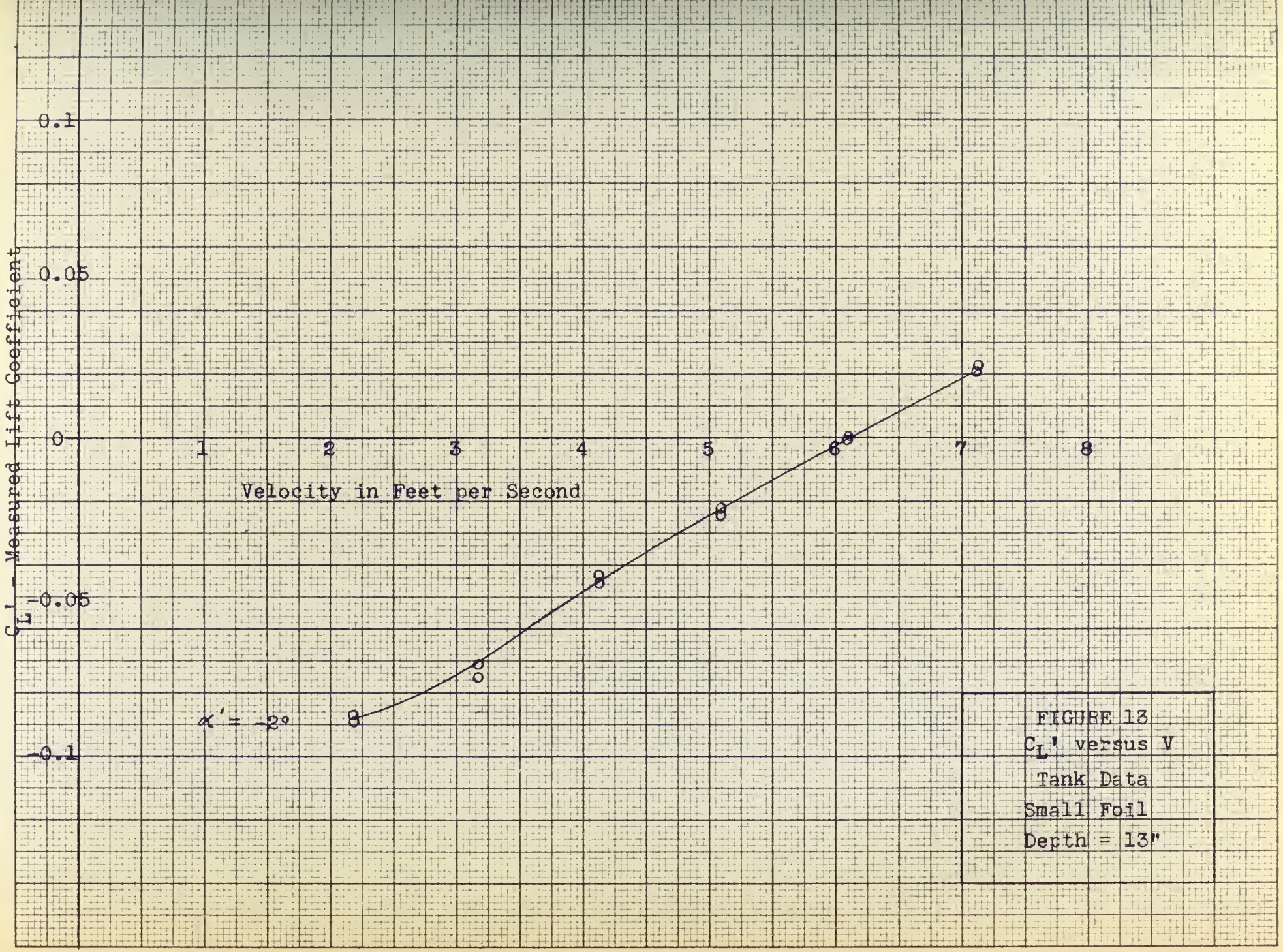

FIGURE 13
C_L' versus V
Tank Data
Small Foil
Depth = 13"

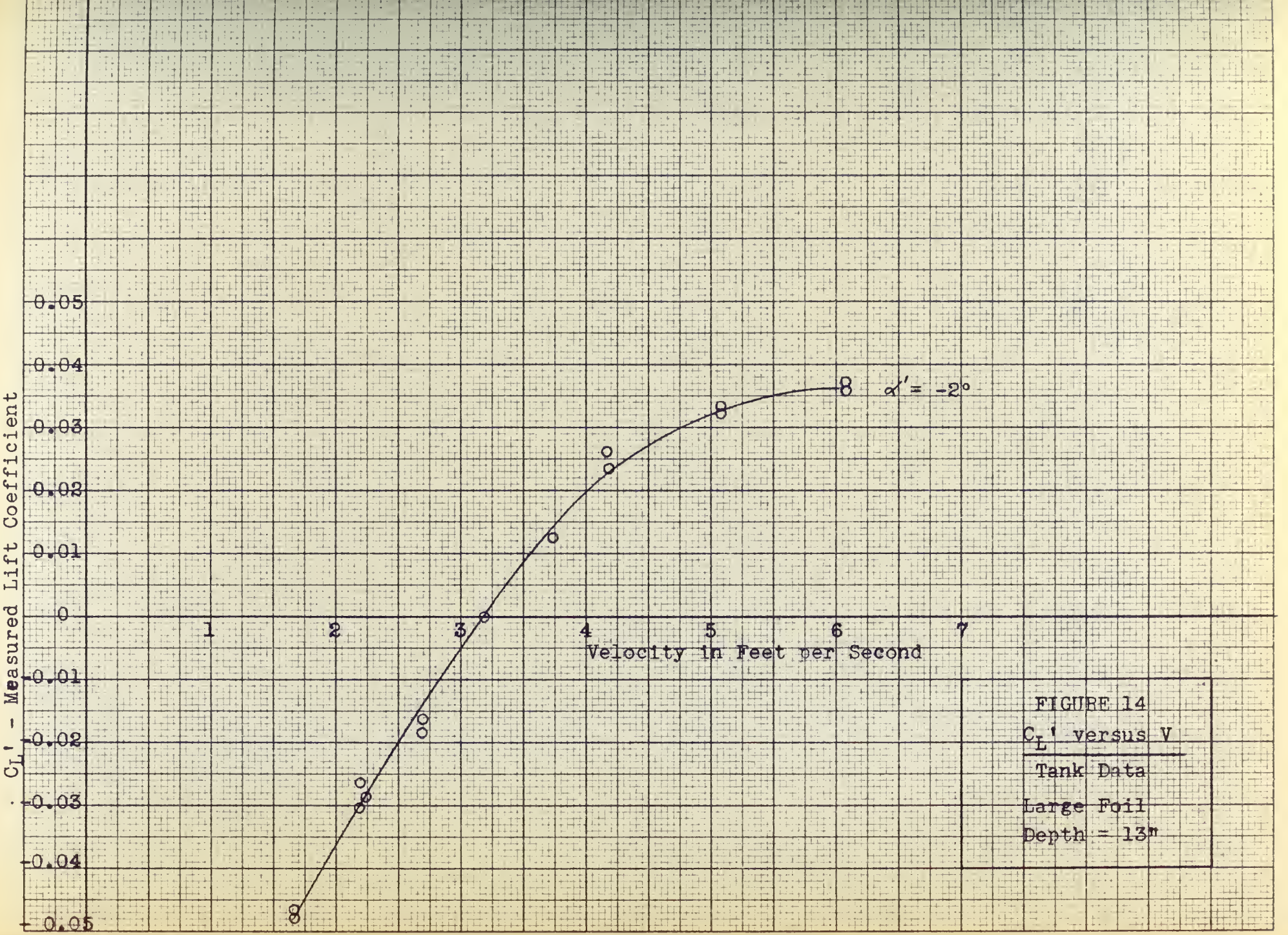

FIGURE 14

C_L' versus V

Tank Data

Large Foil

Depth = 13"

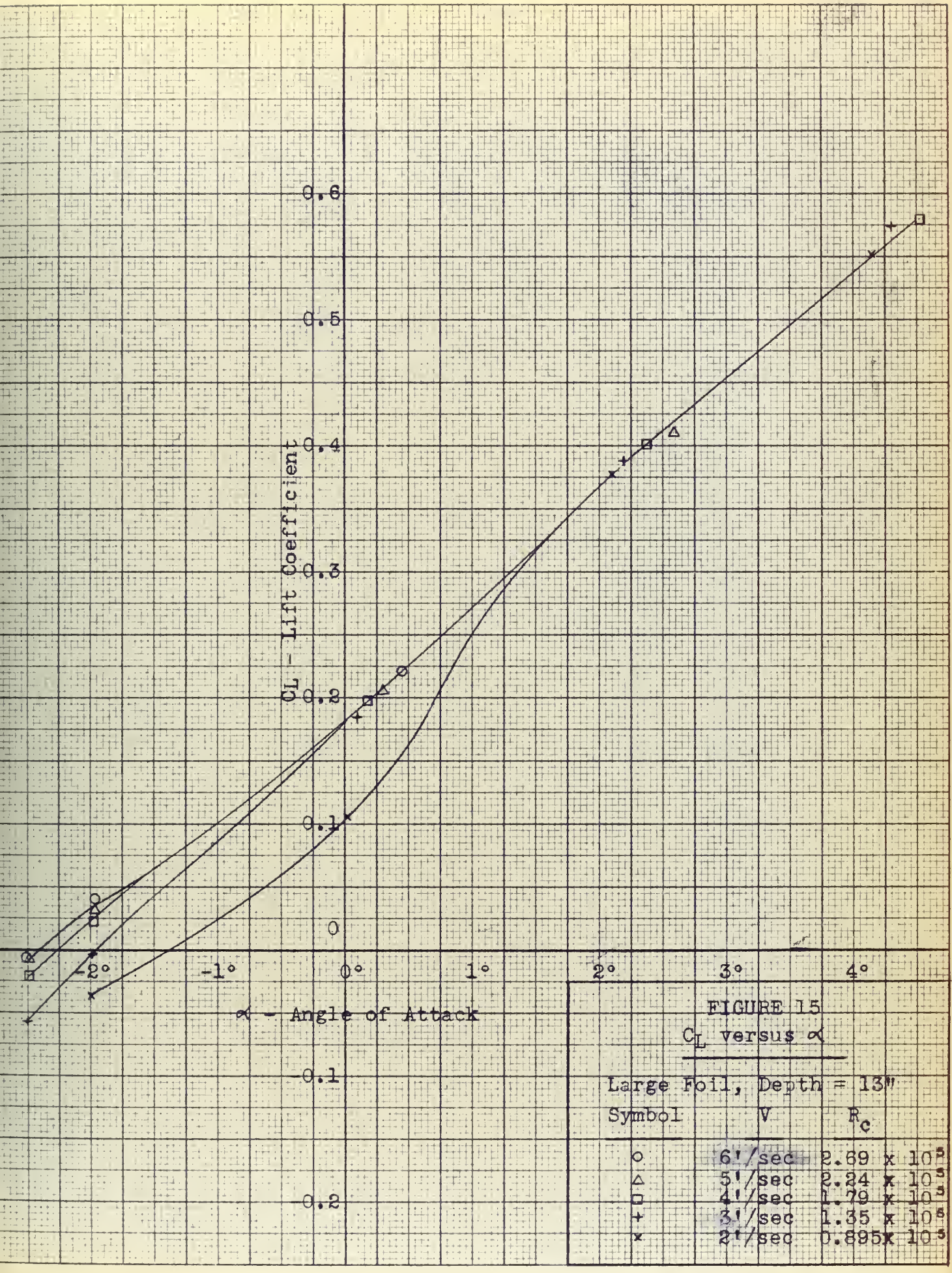

FIGURE 15

C_L versus ∝

Large Foil, Depth = 13"

Symbol	V	R_c
○	6'/sec	2.69 x 10^5
△	5'/sec	2.24 x 10^5
□	4'/sec	1.79 x 10^5
+	3'/sec	1.35 x 10^5
×	2'/sec	0.895x 10^5

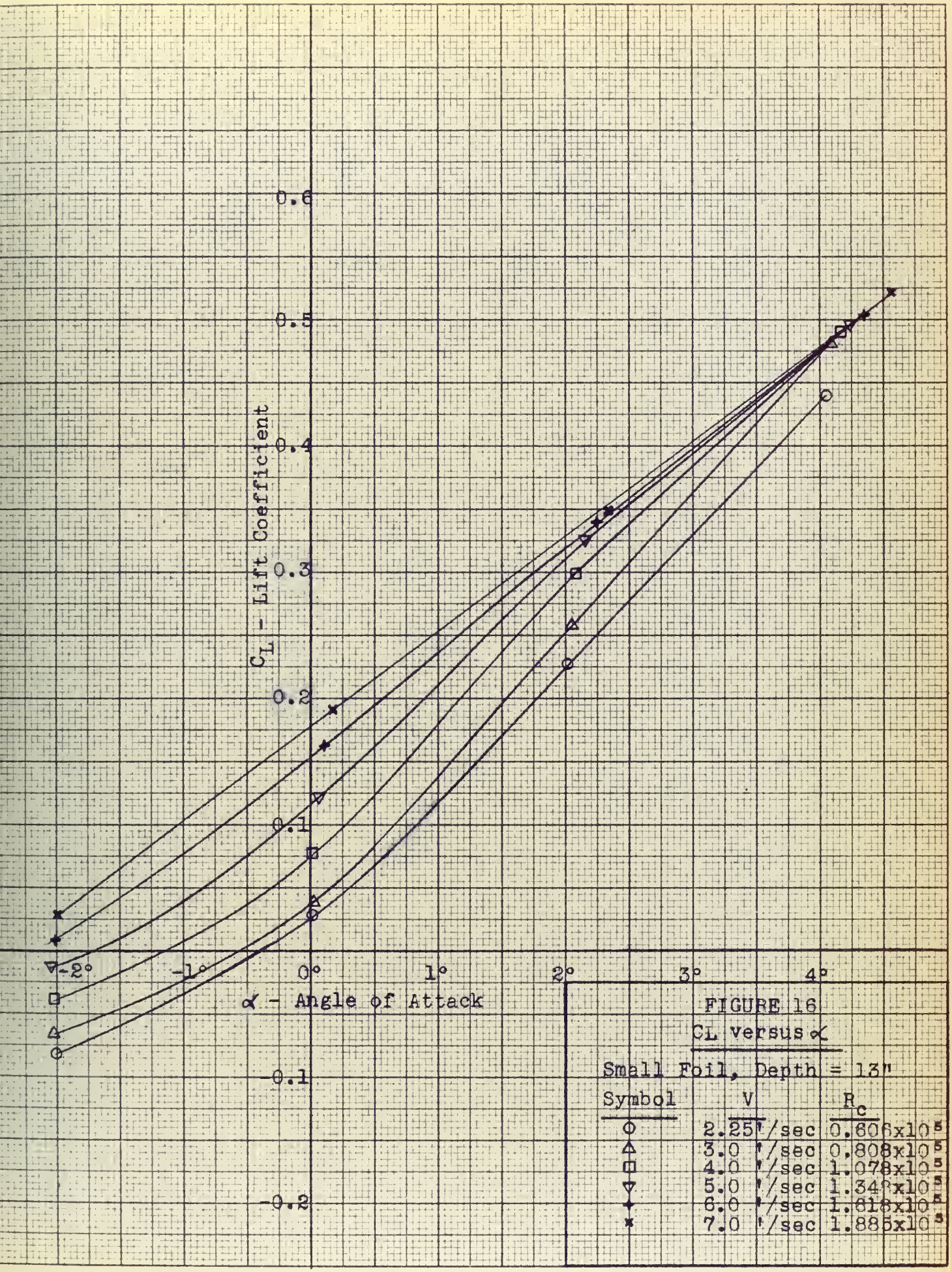

FIGURE 16

C_L versus α

Small Foil, Depth = 13"

Symbol	V	R_c
◇	2.25 ft/sec	0.606×10^5
△	3.0 ft/sec	0.808×10^5
□	4.0 ft/sec	1.078×10^5
▽	5.0 ft/sec	1.348×10^5
✦	6.0 ft/sec	1.618×10^5
*	7.0 ft/sec	1.885×10^5

FIGURE 17

C_D versus C_L

Large Foil, Depth = 13"

Symbol	V	R_c
○	6'/sec	2.69×10^5
△	5'/sec	2.24×10^5
□	4'/sec	1.79×10^5
+	3'/sec	1.35×10^5
×	2'/sec	0.895×10^5

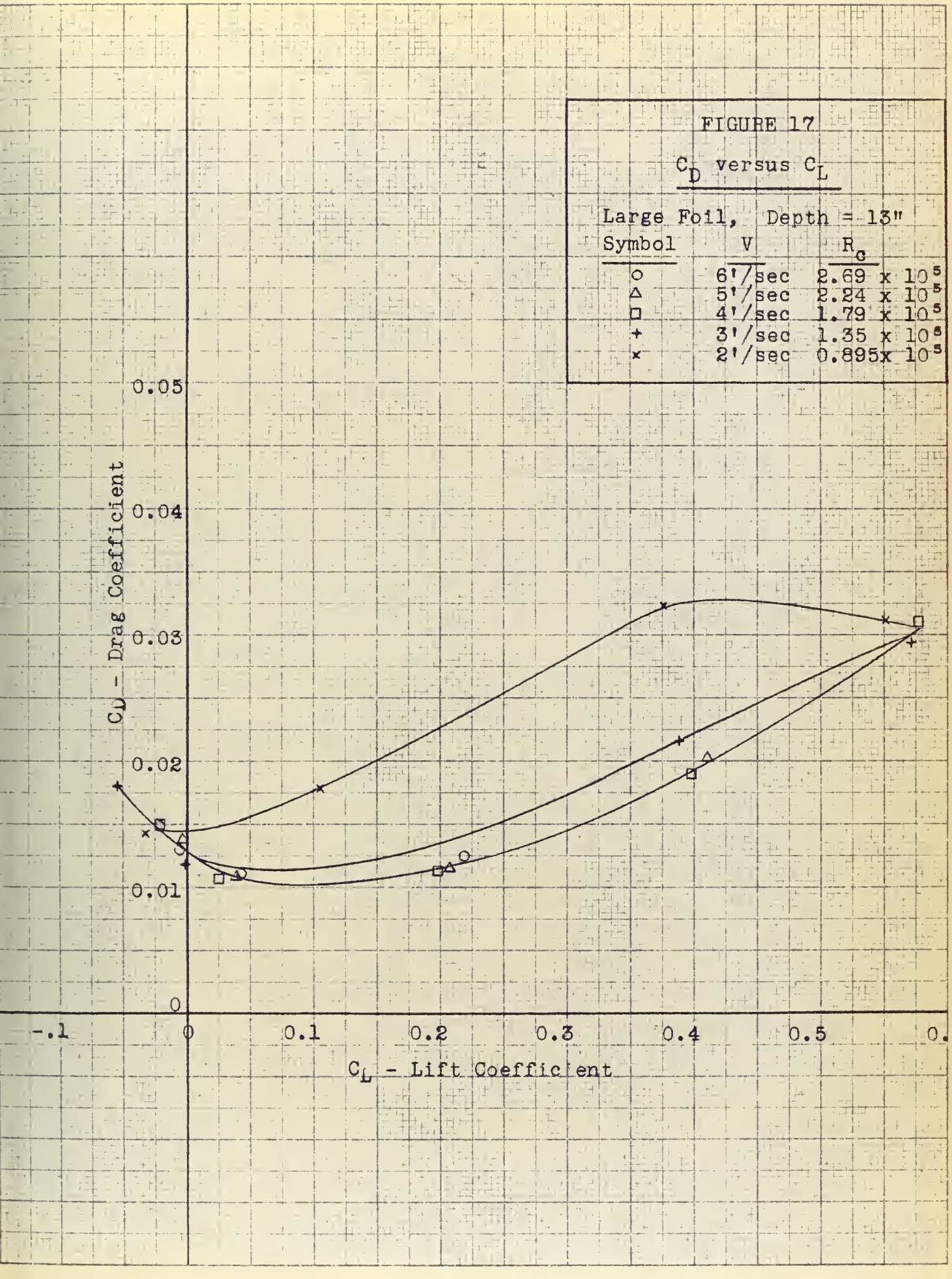

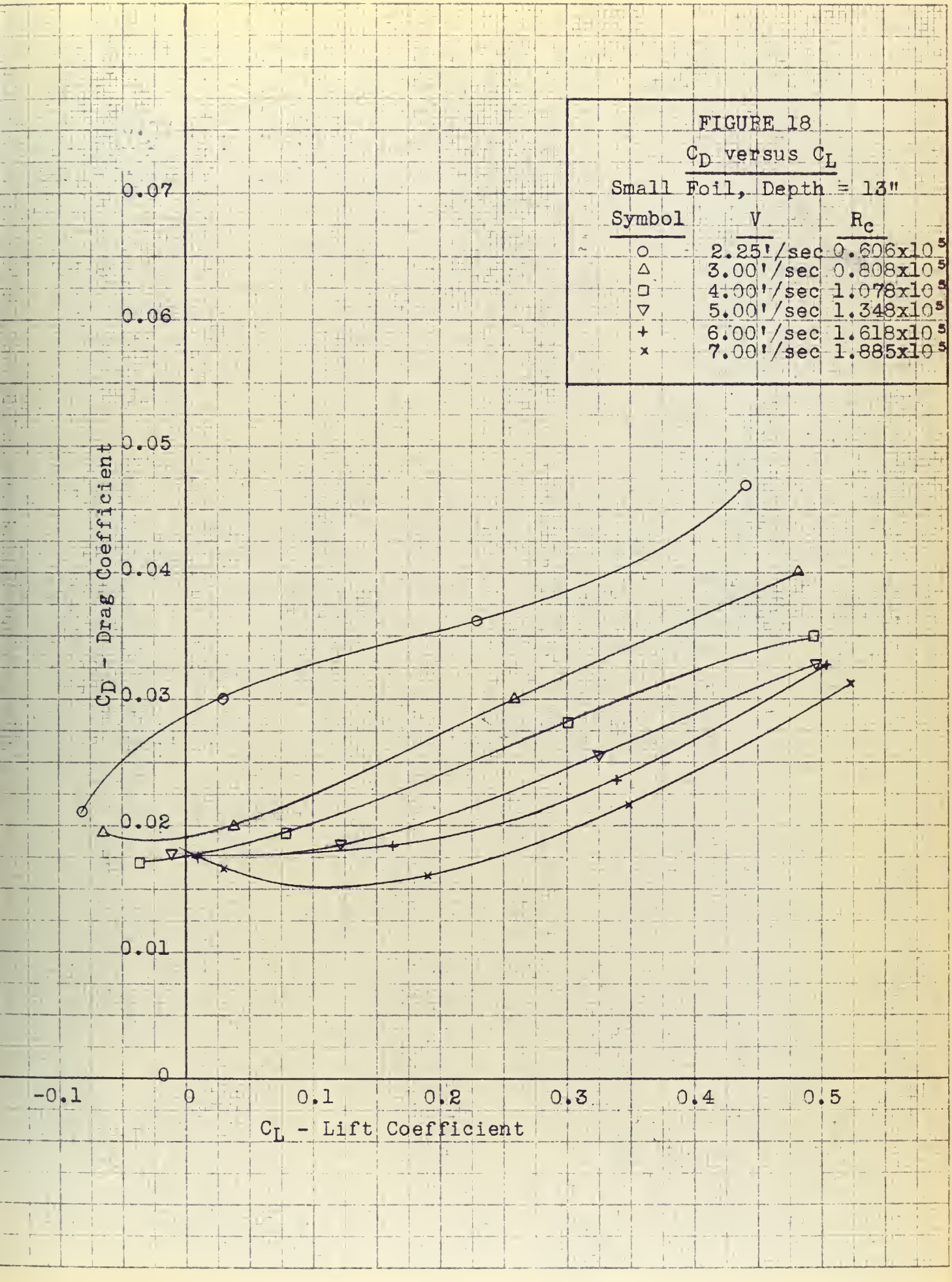
FIGURE 18
C_D versus C_L
Small Foil, Depth = 13"
Symbol V R_c
○ 2.25'/sec 0.606x10^5
△ 3.00'/sec 0.808x10^5
□ 4.00'/sec 1.078x10^5
▽ 5.00'/sec 1.348x10^5
+ 6.00'/sec 1.618x10^5
× 7.00'/sec 1.885x10^5
0.07
0.06
0.05
0.04
0.03
0.02
0.01
0
C_D - Drag Coefficient
-0.1
0
0.1
0.2
0.3
0.4
0.5
C_L - Lift Coefficient

FIGURE 19

L/D versus C_L

Large Foil, Depth = 13"

Symbol	V	R_c
◇	6'/sec	2.69 x 10^5
△	5'/sec	2.24 x 10^5
□	4'/sec	1.79 x 10^5
+	3'/sec	1.35 x 10^5
×	2'/sec	0.895x 10^5

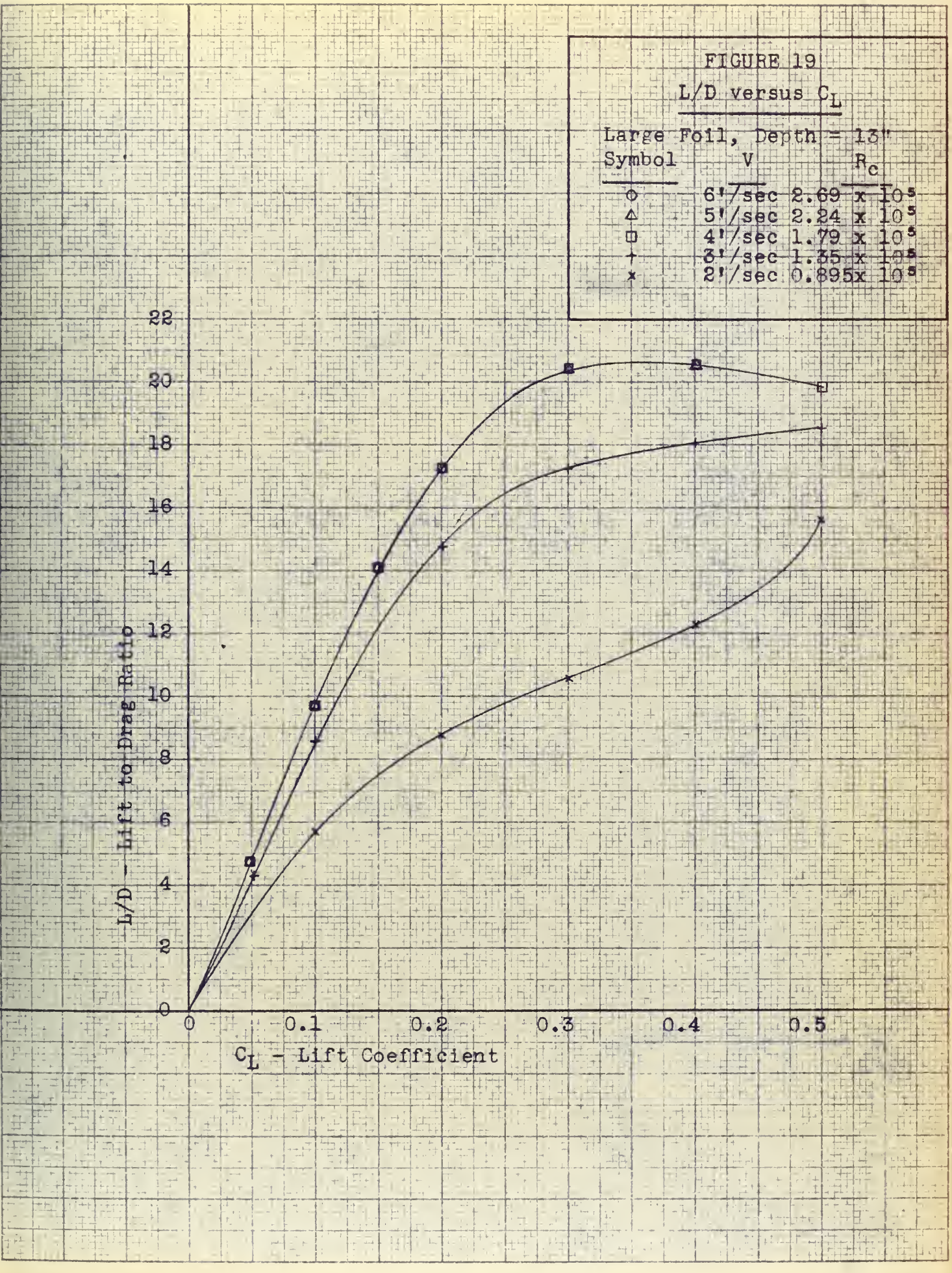

FIGURE 20

L/D versus C_L

Small Foil, Depth = 13"

Symbol	V	R_c
○	2.25'/sec	0.606×10^5
△	3.00'/sec	0.808×10^5
□	4.00'/sec	1.078×10^5
▽	5.00'/sec	1.348×10^5
+	6.00'/sec	1.618×10^5
×	7.00'/sec	1.885×10^5

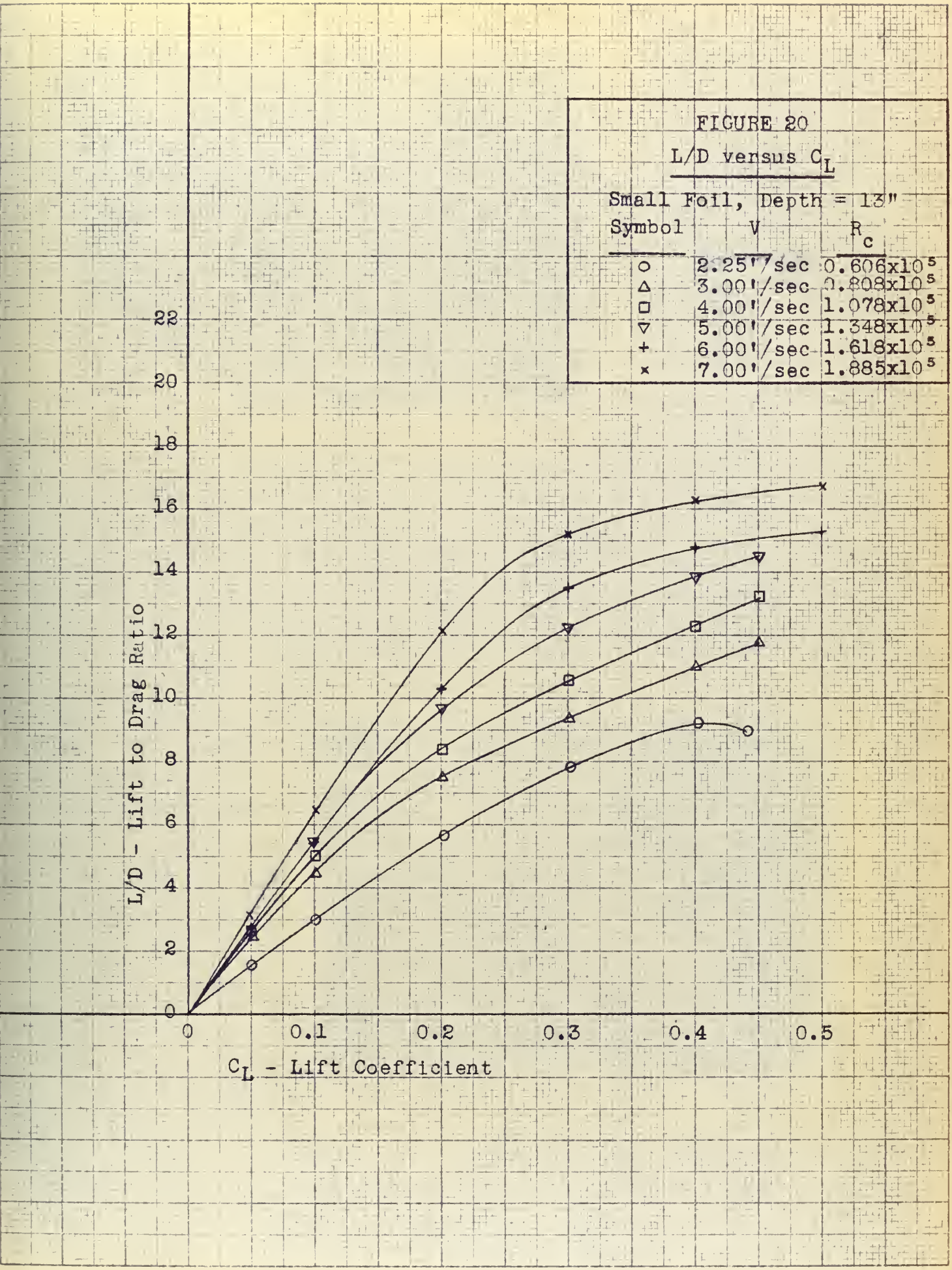

Figure 21

Large Foil: $\alpha' = 4°$,

Depth = 13",

V = 4'/sec.

Figure 22

Large Foil: $\alpha' = 4°$,

Depth = 13",

V = 4'/sec.

Figure 23

Large Foil: $\alpha' = 4^\circ$,

Depth = 13",

V = 2'/sec.

Figure 24

Large Foil: $\alpha' = 4^\circ$,

Depth = 13",

V = 2'/sec.

Figure 25

Large Foil: $\alpha' = 0°$,

Depth = 13",

V = 2'/sec.

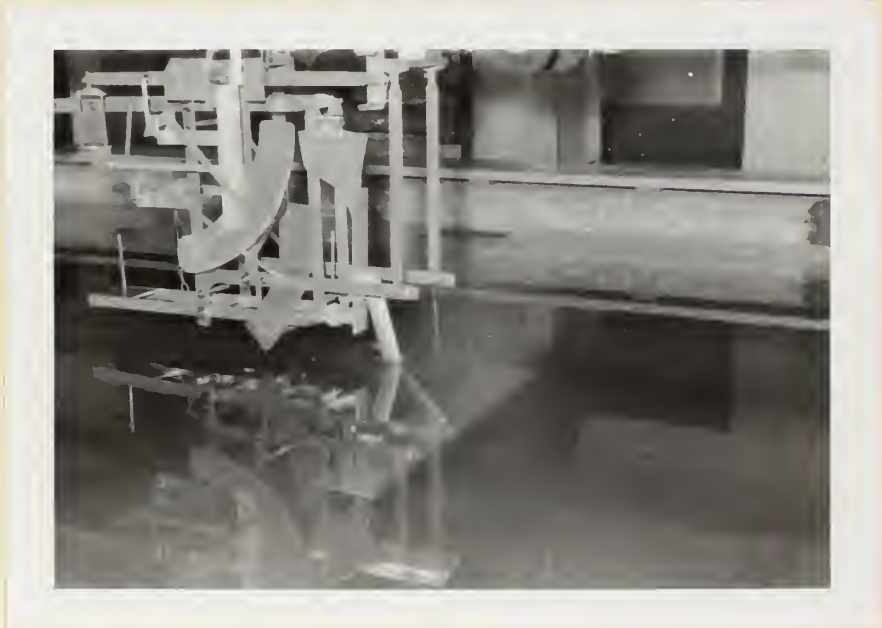

Figure 26

Large Foil: $\alpha' = 0°$,

Depth = 13",

V = 6'/sec.

IV. DISCUSSION

A. Strut Results

Although the strut was not one of the primary test vehicles, its shape compares favorably with ship appendages such as shaft supporting struts, rudders, and support struts for hydrofoil boats. As a result the authors felt a detailed analysis was warranted. Since the strut pierced the surface, part of its total resistance was due to wavemaking. In order to compare the strut profile drag coefficient with both theory and other experimental data it was necessary to obtain a value for wavemaking resistance, which could be deducted from total resistance.

In reference (5) strut wavemaking resistance was found by towing a strut at several depths. Total resistance was plotted vs depth at constant speed. These plots indicated a straight line relationship between these values. This line was extrapolated to zero depth and the value thus obtained minus a correction for tip drag was the strut wavemaking resistance. These experimental results compared very favorably with a theoretical curve proposed by Havelock (Ref. 10) at speeds below the critical wave speed of the tank. For the Webb tank the critical wave speed is

$$V = \sqrt{gh}$$

$$V = \sqrt{32.2 \times 5} = 12.79 \text{ ft./sec.}$$

All tests run were considerably below this speed.

Havelock's method applies to a strut of infinite length projecting vertically into a fluid of infinite depth. The strut in question is of finite length and raked 16.167 degrees from the vertical when the foil is at zero angle of attack. Therefore it is obvious that the results of this analysis will be approximate at best.

To simplify calculations the strut section was approximated by a parabola.

$$y = b\left(1 - \frac{x^2}{l^2}\right)$$

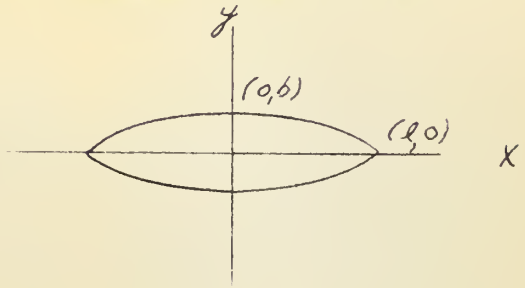

l = half length of section

L = 2l, where L in this case is the strut chordal length

b = half thickness of the section at the midpoint

Appendix I shows that the strut is actually lens-shaped, however, the assumed parabola is a close approximation.

Using the parabola in Havelock's equation we get the wavemaking drag of the strut.

$$(1)\quad D_{sw} = \frac{512}{\pi} g\rho b^2 l^2 \left\{\left(\frac{1}{144}\rho - \frac{1}{5760}\rho^3 + \cdots\right)\log\frac{2}{\gamma\rho} + \frac{7}{576}\rho - \frac{161}{2073600}\rho^3 + \cdots\right\}$$

D_{sw} = wavemaking drag in pounds

g = acceleration due to gravity

ρ = mass density of the fluid

l = half length of section in feet

γ = Euler's constant = .57722

$p = gL/V^2$

V = free stream velocity ft./sec.

The independent variable, p, is the inverse square of Froude number.

The strut angle selected for computation was 16.167 degrees which corresponds to a foil angle of attack of 0 degrees. Since the strut is raked, the actual chordal length becomes;

$L = 1.5/\cos.\ 16.167 = 1.56$ inches

$l = .78$ inches

$b = .201$ inches

Using these values the wave drag coefficient of the strut, $C_{ds,w}$, was computed and plotted in Figure 27. The wave drag coefficient was then deducted from the measured drag coefficient to obtain the profile drag coefficient, C_{dp}. It can be seen that wave drag is a relatively small value compared with profile drag.

Reference 3 states that at Reynolds numbers below the value of 1×10^6 the flow phenomenon of laminar separation begins to take place. Laminar separation is in turn accompanied by a sharp rise in drag coefficient, particularly for relatively blunt shapes. Hoerner's equation for drag due to laminar separation is

$$(2) \qquad C_{dp} = 2C_f + (t/c)^2$$

C_{dp} = profile drag coefficient

C_f = Blasius laminar skin friction

t/c = thickness ratio

Reference 3 also indicates a correction should be made to account for the tip in the three dimensional case. For this strut the correction is negative and equal to -0.0003. The theoretical equation then becomes

$$(3) \qquad C_{dp} = 2C_f + (t/c)^2 - 0.0003$$

This equation and some experimental data from reference 3 are plotted along with strut data in Figure 28. The strut data shows reasonably good correlation with both experimental data and theory. Discrepancies are no doubt due to errors in theoretical wave drag as well as the tip drag of the strut. The plots do, however, verify the fact that there is a major increase

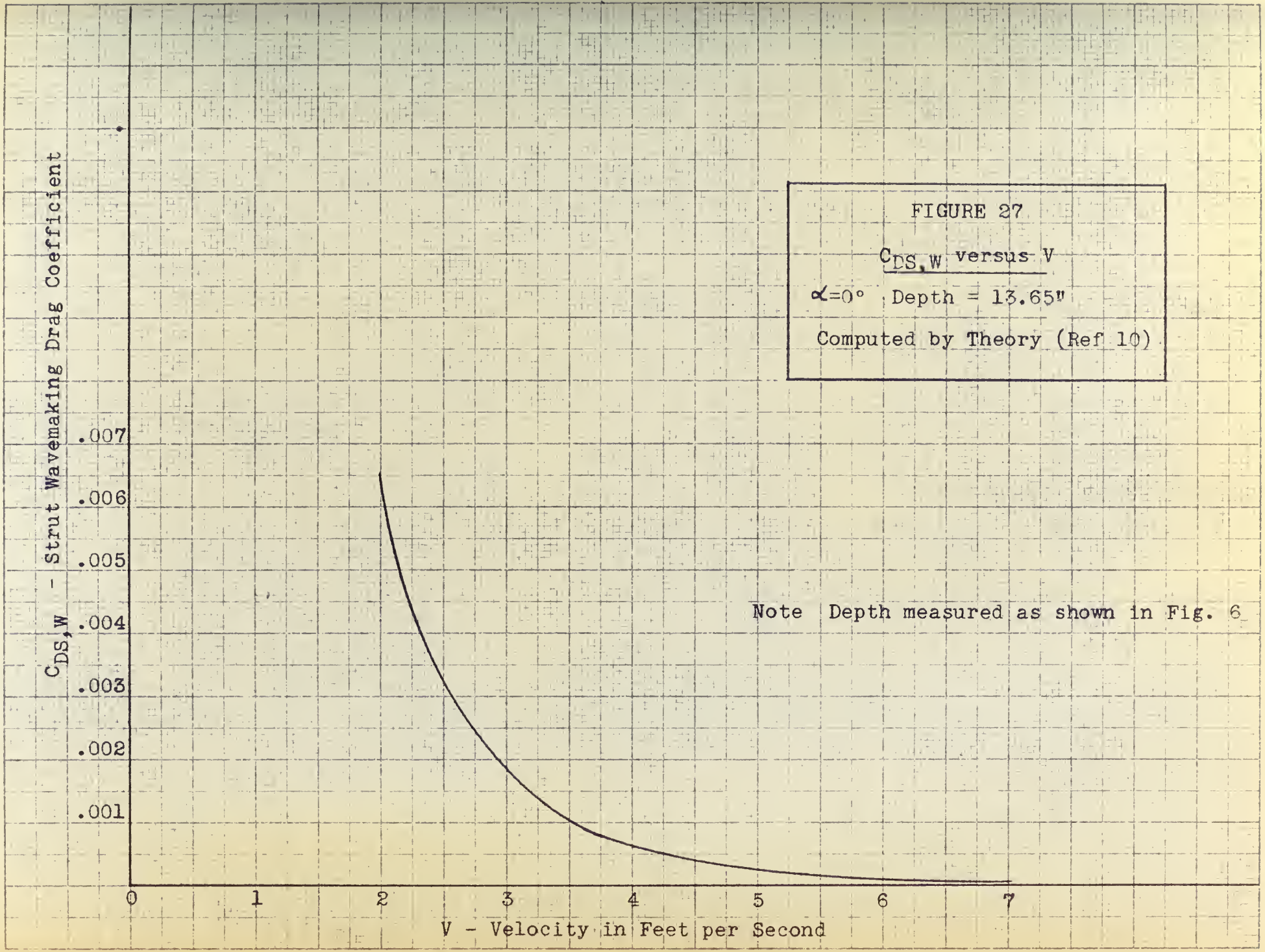

FIGURE 27

$C_{DS,W}$ versus V

α=0° Depth = 13.65"

Computed by Theory (Ref 10)

Note Depth measured as shown in Fig. 6

EXPERIMENTAL DATA
STRUT (t/c = 0.258)
OGIVAL SECTION

THEORY (REF. 3) (t/c = 0.258)
$C_{DP} = 2C_f + (t/c)^3 - .0003$

EXPERIMENTAL DATA
(REF. 3) (t/c = 0.25)

THEORY (REF. 3) (t/c = .09)
$C_{DP} = 2C_f + (t/c)^3 - .0006$

SMALL FOIL (t/c = .09)
NACA 64-409 SECTION
$C_L = 0$

NACA STRUT (t/c = 0.21)
UNPUBLISHED DATA

LARGE FOIL (t/c = .09)
NACA 64-409 SECTION
$C_L = 0$

BLASIUS LAMINAR

SCHOENHERR

WIND TUNNEL DATA
NACA 64-409
SECTION DRAG AT $C_L = 0$
(REF. 4)

C_{DP}

REYNOLDS NUMBER, R_c

FIGURE 28

VARIATIONS IN PROFILE DRAG COEFFICIENT, C_{DP} WITH REYNOLDS NUMBER FOR EXPERIMENTAL HYDROFOILS AND STRUT. INCLUDED ALSO ARE VARIOUS EXPERIMENTAL AND THEORETICAL CURVES FOR SIMILAR SHAPES

in profile drag due to laminar separation. On the same plot is included some unpublished data for the strut towed in Reference 6. It can be seen that at the higher Reynolds numbers this strut is producing drag coefficients below the turbulent friction line, however, as it reaches the transition range there is a sharp rise in drag coefficient. It is also important to note the fact that the rise in drag coefficient starts at a Reynolds number of about 10^6. Although there is no data to corroborate this fact, it seems justifiable to assume the NACA strut drag would continue to rise until it reaches a value comparable to the test strut of this investigation.

The salient point of this investigation is the fact that there is a major increase in drag coefficient once laminar separation begins. As Figure 28 shows the drag coefficient of the strut is almost 7.5 times the coefficient of friction for turbulent flow at $R_c = 10^5$. This indicates extreme care must be taken in expanding the measured resistance of appendages on ship models to the full size ship.

B. METHODS TO PREDICT LIFT AND DRAG

The experimental hydrofoil data of this report takes on more meaning when presented against a background of previous data and theory. A survey of available literature showed that NACA data and theory could be utilized most readily for this purpose. These data and theory establish a point of departure from which to discuss the results of the low Reynolds number tests. The easiest method of correcting the two dimensional wind tunnel data to three dimensional flow, was to neglect towing tank boundary effects and apply the classical method of references 1 and 2. This method is discussed first, and is used to calculate both lift and drag coefficients based on airfoil data. The second method presented is an extension of the classical method, which employs airfoil data again, but also includes corrections for tank boundaries, water surface and wave drag. This modified classical method is based on the subcritical theory of reference 7. It is used to correct the drag coefficient for boundary effects and wave drag. It is not used to make any corrections to the lift coefficient. Thirdly, a fairly rigorous theoretical method is presented to predict the lift coefficient. This method, from reference 11, can be used without previous data of any kind, but better results were obtained in this case, after an experimental angle of zero lift was substituted for the theoretical angle of zero lift.

1. The Classical Method.

Reference 4 is the source of data for the NACA 64-409 airfoil section. The data covers a range well above the range of this report. ($R_c = 0.7 \times 10^6$ to $R_c = 9.0 \times 10^6$.) The comparison of the NACA airfoil data to the hydrofoil data obtained in the present tests emphasizes Reynolds number effects. Therefore, the airfoil data was converted from two dimensional to three

dimensional coefficients, applicable to the hydrofoils. This was accomplished by the classical method given in references 1 and 2. The classical method corrects for aspect ratio by adding induced drag to section drag and induced angle of attack to the section angle of attack. Thus, the following formulae from references 1 and 2 were used to correct airfoil data for finite aspect ratio at $R_c = 0.7 \times 10^6$ and $R_c = 9.0 \times 10^6$.

$$(4)\quad C_d = cd + \frac{c_l^2}{\pi A}(1 + \delta)$$

$$(5)\quad \alpha = \alpha_o + \frac{c_l}{\pi A}(1 + \tau)$$

In which: C_d is the three dimensional drag coefficient.

c_d is the two dimensional section drag coefficient.

c_l is the two dimensional section lift coefficient.

α is the three dimensional angle of attack.

α_o is the two dimensional section angle of attack.

A is the aspect ratio. (6)

δ is the plan form correction factor to drag coefficient.

τ is the plan form correction factor to angle of attack.

For A = 6, $\delta = 0.045$ and $\tau = 0.165$ (Ref. 2)

The curves which are the solutions to equations (4) and (5) are compared to the hydrofoil experimental data in figures 33, 34, 36 and 37.

This comparison is not rigorous since no consideration is given to the effects of the free water surface or of the tank boundaries. The boundary effects are small, however, as will be shown in the theoretical method to follow, so this comparison is valuable to demonstrate the trend of the lift coefficient to decrease and the drag coefficient to increase as Reynolds number is reduced.

2. A Refinement to the Classical Method.

Since the classical method of predicting hydrofoil lift and drag did not include boundary effects or wave drag, the predictions by this method were of doubtful value. The classical method is normally used to predict aerodynamic forces on finite wings in an infinite medium of air. If the method is used in this manner, boundary effects are not a problem. Hydrofoils, however, are usually subject to boundary effects. In these tests the hydrofoils were submerged beneath a free water surface in a towing tank of finite dimensions. Therefore, predictions by the classical method could very well be inaccurate, if boundary effects and wave drag are ignored. A prediction problem of some kind exists, as may be seen by comparing the predictions based on airfoil data to the experimental data in figures 33, 34, 36 and 37. The experimental drag is noticeably higher than the predicted drag. This discrepancy could have been caused by boundary effects or by the wave drag or by both.

For this reason, the boundary effects and wave drag were evaluated theoretically using the methods of reference 7. This theory adds two additional terms to the expression for induced drag, one for boundary effects and the other for Froude number wave drag. These two additional terms should be evident by comparing equation (4) with equation (21) of reference 7, herein designated equation (6).

$$(6)\quad C_d = c_d + c_l^2 \left[\frac{(1+\delta)}{\pi A} + \frac{K_1 c (1+\delta)}{8\pi} + \frac{1}{2(V^2/gc)} \psi \right]$$

In which: C_d, c_d, c_l, δ and A have been defined previously.

V is hydrofoil speed in feet per second.

g is gravitational acceleration.

c is the hydrofoil chord in feet.

ψ is the hydrofoil submergence parameter in this case, $\psi = e^{-\frac{2}{V^2/gf}}$

f is the hydrofoil depth in feet.

K_1 is the correction factor for the induced drag due to the boundary image trailing vortices.

In selecting equation 21 from reference 7, subcritical theory was dictated, since all of the subject hydrofoil tests were conducted at speeds less than 12.76'/sec, the critical wave speed of the Webb tank.

The term $\frac{K_1 c(1+\delta)}{8\pi}$ in equation (21), reference 7, represents the contribution of the free water surface to the induced drag of the hydrofoil. A new value of K_1 was derived for use in equation (6), however, which includes tank side and bottom effects as well as the water surface effects. The same type of derivation was used to evaluate the new K_1 as is presented in reference 7 for the corresponding quantity.

The wave drag contribution to induced drag is represented by the term $\frac{1}{2(V^2/gc)}\psi$. Reference 7 gives three expressions for ψ, one for a two dimensional hydrofoil in water of infinite depth, one for a two dimensional hydrofoil in water of finite depth and another for a three dimensional hydrofoil in water of infinite depth. The authors of reference 7 found that the expression $\psi = e^{-\frac{2}{V/gf}}$, for a two dimensional hydrofoil in water of infinite depth, gave the best agreement with experimental data. This particular expression for ψ is also the least complicated of the three, and therefore, was used by the authors to evaluate the wave drag term in equation (6). It can be seen that wave drag is a function of hydrofoil depth, chord and speed. In evaluating this quantity, therefore, foil depth and chords for the test hydrofoils were used. The velocity values used were representative of low Reynolds number hydrofoil tests. The particular speeds selected correspond to $R_c = 1.5 \times 10^5$ and $R_c = 2.0 \times 10^5$.

Equation (6) was solved using the same NACA airfoil section lift and drag coefficients as were used to solve equation (4). (Ref 4, NACA 64-409

airfoil, at $R_c = 0.7 \times 10^6$.) Since the identical airfoil data were used to solve both equations (4) and (6), the difference between the two solutions represents a theoretical prediction of the portion of the total drag that is caused by wave drag and the presence of boundaries. Since the induced drag is directly proportional to the square of the lift coefficient, the increase in drag due to boundary effects and wave drag is greatest at large lift coefficients. At low lift coefficients, these effects are negligible. The discrepancy between drag coefficients predicted from airfoil data and the drag coefficients determined experimentally exists over the entire range of lift coefficients, however. Therefore, wave drag or boundary effects must be ruled out as the major cause of this difference. Laminar separation will be discussed later as a possible cause of these differences between theory and experiment.

The reader should note that the boundary and wave drag corrections of equation (6) apply only to the drag coefficient and do not effect the lift coefficient. Boundary effects on the lift coefficient will be considered in the theoretical method that follows.

3. A More Rigorous Theoretical Method

It was desirable to compare the experimental lift at low Reynolds number to the lift predicted by theory. This comparison demonstrates to what extent the circulation theory is trustworthy at low Reynolds numbers.

The most attractive theoretical method was found in reference 11, by Wadlin and Christopher. This method was particularly applicable in this instance because (1) it was independent of experimental data and (2) the theory could be modified to include tank boundary effects. Reference 11 states that the lift coefficients calculated by this method are in good

agreement with existing experimental data. The experimental data to which Wadlin and Christopher refer was taken on large foils at speeds of 25 to 30 feet per second and was carefully chosen to avoid low speeds, where some variation of lift coefficient with speed has been indicated. This method represents a fairly reliable integration of the lifting characteristics of hydrofoils at high Reynolds numbers, and, therefore, is a good yardstick to which low Reynolds number data may be compared.

The purpose of the Wadlin-Christopher method is to predict the lift of practical seaplane or small boat hydrofoil configurations in open water. For this reason, the theory includes a correction for the effects of water surface, but no attention is given to the towing tank side or bottom effects. Therefore, either the theory had to be modified to include tank boundary effects or the experimental hydrofoil data had to be corrected to open water conditions in order to properly compare theory and experiment. For this report, the theory was modified to include the effect of the proximity of the sides and bottom of the tank. Thus, the experimental data is left in its original form and the boundary corrections are applied entirely to the theory.

From reference 11, the lift coefficient of submerged zero-dihedral surfaces is calculated from the following equation:

$$(7)\quad C_l = \frac{a_o K_2 K_3 A \alpha_a}{A + 1 + \frac{K_2 a_o}{\pi}} + K_3 \frac{8}{3}\left(1 + \frac{A}{10}\right)\sin^2\alpha_a \cos\alpha_a$$

In which: a_o is the two dimensional lift curve slope (2π).

A is the aspect ratio (6).

K_2 is the two dimensional depth correction factor.

K_3 is the three dimensional depth correction factor.

α_a is the absolute angle of attack, measured from the angle of

zero lift ($\alpha_a = \alpha_{L,o} + \alpha$).

$\alpha_{L,o}$ is the angle of zero lift.

α is the geometric angle of attack.

Since this formula includes only a correction for the water sruface boundary, the factors K_2 and K_3 were modified to include the tank side and bottom effects also.

Modification of K_2.

The two dimensional correction factor K_2 was determined in references 7 and 11 by considering the effect, at the three quarter chord of a submerged two dimensional lifting surface, of an image line vortex located a distance above the water surface equal to the depth of submergence of the quarter-chord of the lifting surface. The vorticity of both the lifting surface and its image are located at their respective quarter-chords. In order to include the bottom effects in K_2, the effect of another image line vortex located a distance below the bottom equal to the height of the lifting surface above the bottom is considered at the quarter chord point of the lifting surface.

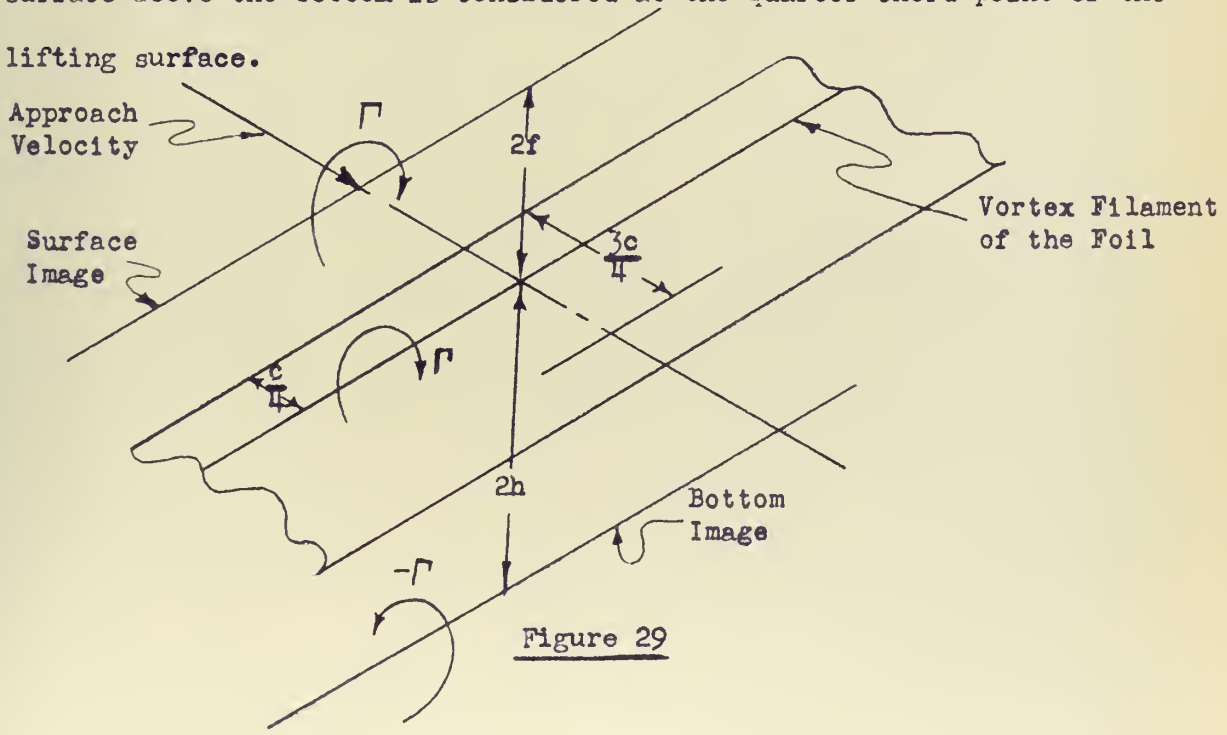

Figure 29

Using the methods of reference 7:

$$(8)\quad \frac{a_{o,1}}{a_{o,2}} = \frac{w_1 + w_2 - w_3}{w_1}$$

In which: w_1 is the downwash at $3c/4$ due to vortex filament of the foil.

w_2 is the downwash at $3c/4$ due to surface image vortex.

w_3 is the downwash at $3c/4$ due to tank bottom image vortex.

$a_{o,1}$ is the lift curve slope in an infinite fluid.

$a_{o,2}$ is the lift curve slope in an finite fluid.

Applying the Law of Biot-Savart as outlined in reference 7, the various contributions to downwash were evaluated and the following formula derived:

$$(9)\quad K_2 = \frac{a_{o,2}}{a_{o,1}} = \frac{1 + (4f/c)^2 + (4h/c)^2 + (4h/c)^2(4f/c)^2}{1 + 2(4h/c)^2 + (4f/c)^2(4h/c)^2}$$

In which: c is the foil chord.

f is the foil depth below the water surface.

h is the foil height above the bottom.

For the dimensions of the foils tested at a depth of 13.0" in the Webb Tank: (Webb Tank dimensions: 5'x10' cross section.)

$K_2 = 0.992$ for the large foil (c=5")

$K_2 = 0.997$ for the small foil (c=3")

Modification of K_3

Since the method of reference 11 only corrects the lift curve slope for the water surface boundary, a new factor, K_3, was developed to incorporate tank side, tank bottom and water surface effects in the three dimensional correction. As stated in reference 7, an infinite array of images would be necessary to arrive at an exact correction, but for the purposes used here, the following system of images was considered sufficiently accurate.

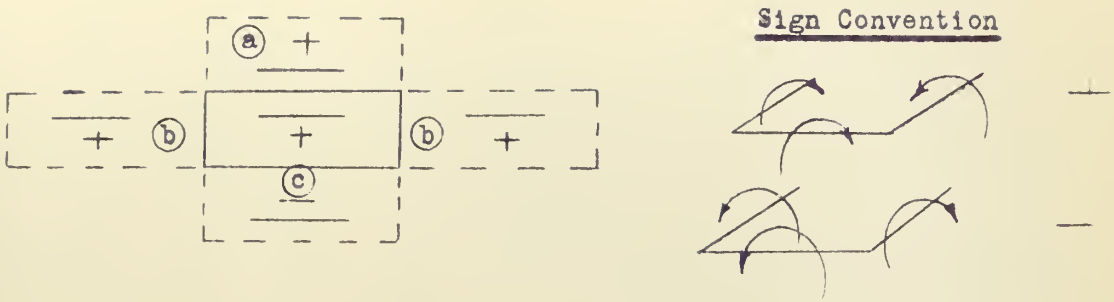

Figure 30

The image that contributes the water surface boundary condition is designated (a) and is positive. The images that contribute the tank side boundary conditions are designated (b) and are positive. The image system that contributes tank bottom boundary conditions is designated (c) and is negative.

Using the same principles as were used to obtain K_2:

$$(10)\quad K_3 = \frac{\Gamma_2}{\Gamma_1} = \frac{a_2}{a_1} = \frac{1}{1 + \frac{w_a + 2w_b - w_c}{w_4}}$$

In which: Γ_1 is the circulation of the foil horseshoe vortex system in an infinite fluid.

Γ_2 is the circulation of the foil horseshoe vortex system in a fluid with finite boundaries.

a_1 is the lift curve slope of the foil horseshoe vortex system in and infinite fluid.

a_2 is the lift curve slope of the foil horseshoe vortex system in a fluid with finite boundaries.

w_a is the downwash at the three-quarter chord point due to the water surface image.

w_b is the downwash at the three-quarter chord point due to one

tank side image.

w_c is the downwash at the three-quarter chord point due to the tank bottom image.

w_4 is the downwash at the three-quarter chord point due to the image system of the hydrofoil.

The expressions for the above downwashes were derived by substituting proper values in the equations for downwash due to horseshoe vortex systems in reference 1. The results of these derivations are:

$$(11)\quad w_a = \frac{\Gamma A}{\pi c}\left\{\frac{1}{\left[1+(4f/c)^2\right]\sqrt{1+(4f/c)^2+A^2}} + \frac{1}{\left[(4f/c)^2+A^2\right]}\left[1+\frac{1}{\sqrt{1+(4f/c)^2+A^2}}\right]\right\}$$

$$(12)\quad w_b = \frac{\Gamma}{2\pi c}\left\{\frac{(2w/c)+A}{\sqrt{1+(2w/c)^2+2(2w/c)A+A^2}} - \frac{(2w/c)-A}{\sqrt{1+(2w/c)^2-2(2w/c)A+A^2}} + \frac{1}{\left[(2w/c)+A\right]}\left[1+\frac{1}{\sqrt{1+(2w/c+A)^2}}\right] - \frac{1}{\left[(2w/c)-A\right]}\left[1+\frac{1}{\sqrt{1+(2w/c-A)^2}}\right]\right\}$$

$$(13)\quad w_c = \frac{\Gamma A}{\pi c}\left\{\frac{1}{\left[1+(4h/c)^2\right]\sqrt{1+(4h/c)^2+A^2}} + \frac{1}{\left[(4h/c)^2+A^2\right]}\left[1+\frac{1}{\sqrt{1+(4h/c)^2+A^2}}\right]\right\}$$

And from equation (6) of reference 7:

$$(14)\quad w_4 = \frac{\Gamma}{2\pi S}\left[\sqrt{1+A^2}+2\right]$$

Substituting these expressions in equation (10) and evaluating for foil dimensions at 13" depth gives the three dimensional lift curve slope correction:

$K_3 = 0.9717$ for the large foil at $f = 13.0$"

$K_3 = 0.9879$ for the small foil at $f = 13.0$"

Since the angle of attack, α_a, in equation (7) is measured from the angle of zero lift, the value of the angle of zero lift had to be determined. A theoretical angle of zero lift was calculated by the method given in reference 12. Using this value in the equation for lift coefficient, however, resulted in values of C_l too high to be consistent with either the

airfoil data of reference 4, or the experimental hydrofoil data. On the other hand, if the angle of zero lift as measured experimentally by the authors is used, the theoretical and experimental lift curves are in reasonable agreement. (Figs. 33 and 34.)

For the tabular solution of equation (7) the variable was the geometric angle of attack, and the following values were used as constants:

Term	Small Foil	Large Foil
a_o	2π	2π
A	6	6
K_2	0.997	0.992
K_3	0.9879	0.9717
α_{L_0} (measured experimentally)	-2.45°	-2.40°

A sample solution of equation (7) is given in Appendix I.

The theoretical method as modified neglects any variations in boundary effects due to the geometric angle of attack of the foil. These effects on K_2 are negligible at the depths of submergence of these tests, as shown in figure 2(e) of reference 11. Angle of attack may have a significant effect on K_3, but any variation in K_3 due to angle of attack was neglected here for the sake of simplicity. Since a reasonable agreement was obtained between theory and experiment, however, the assumption that the effect of angle of attack is negligible seems to have been valid at the small angles of attack used in the subject experiments. The use of an experimental angle of zero lift with this theory seems to be justified also, since reference 12 warns that theoretical angles of zero lift may be useful for design, but should be verified by experiment whenever possible.

Of the foregoing methods to predict lift and drag, the classical method is the easiest to calculate, but neglects boundary effects. The modification

to the classical method includes the effect of the boundaries and wave drag on the drag coefficient. Both the classical method and its modification are dependent on wind tunnel data. The Wadlin-Christopher method deals only with the lift coefficient and includes boundary effects. The combination of the three methods provides predictions of drag coefficient based on airfoil data and predictions of lift coefficient based both on airfoil data and theory. The results of these predictions are plotted in figures 33, 34, 36 and 37, where they can be compared to the experimental hydrofoil data. The discussion of these comparisons will be the subject of the next section.

C. Analysis of Experimental Results

With both experimental wind tunnel data and theoretical hydrofoil data now available in proper form, a more detailed analysis of the test results can be made. In order to obtain coefficients for each foil at the same Reynolds number, Figures 31 and 32 were plotted and faired. These figures point up one of the key results of the investigation. There are definite discrepancies in the lift and drag coefficients of both foils at the same Reynolds number. At the same angle of attack, the lift coefficients of the large foil are higher than those of the small foil, while the drag coefficients of the small foil are consistently higher than those of the large foil. These plots indicate that Reynolds numbers based solely on free stream velocity and chordal length do not completely define flow similarity in the laminar flow range.

C_l vs α curves for both foils are plotted in Figures 33 and 34. Included on these plots are wind tunnel data from reference 4. As previously explained, classical airfoil theory (Ref. 1) was used to convert from two dimensional to three dimensional flow. The Reynolds numbers selected (0.7×10^6 and 9×10^6) represent the extremes available for the NACA 64-409 series. The theoretical lift curve as calculated for the test hydrofoils is also plotted for reference.

These curves have several interesting features. First, the lift curves of the small and large foils at equivalent Reynolds numbers do not coincide. Secondly, both foils show a depression in the lift curve in the region of $\alpha = 0^\circ$. This hollow becomes more pronounced at the lower Reynolds numbers. This leads one to suspect laminar separation as one of the main causes of this effect. There is no clear explanation as to why the effect is accented at $\alpha = 0^\circ$.

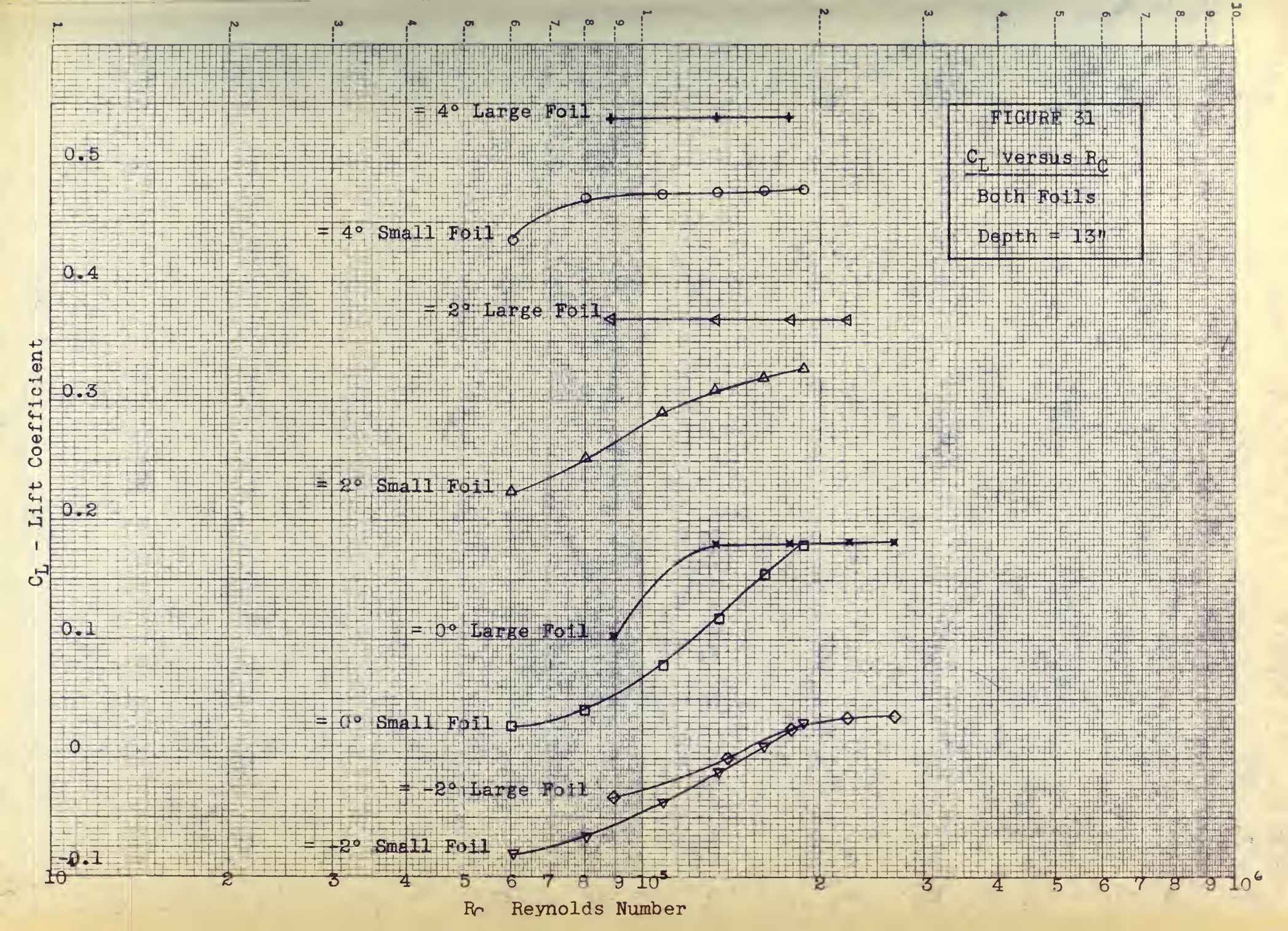
FIGURE 31
C_L versus R_C
Both Foils
Depth = 13"
= 4° Large Foil
= 4° Small Foil
= 2° Large Foil
= 2° Small Foil
= 0° Large Foil
= 0° Small Foil
= -2° Large Foil
= -2° Small Foil
0.5
0.4
0.3
0.2
0.1
0
-0.1
C_L - Lift Coefficient
10^5
10^6
R_C Reynolds Number

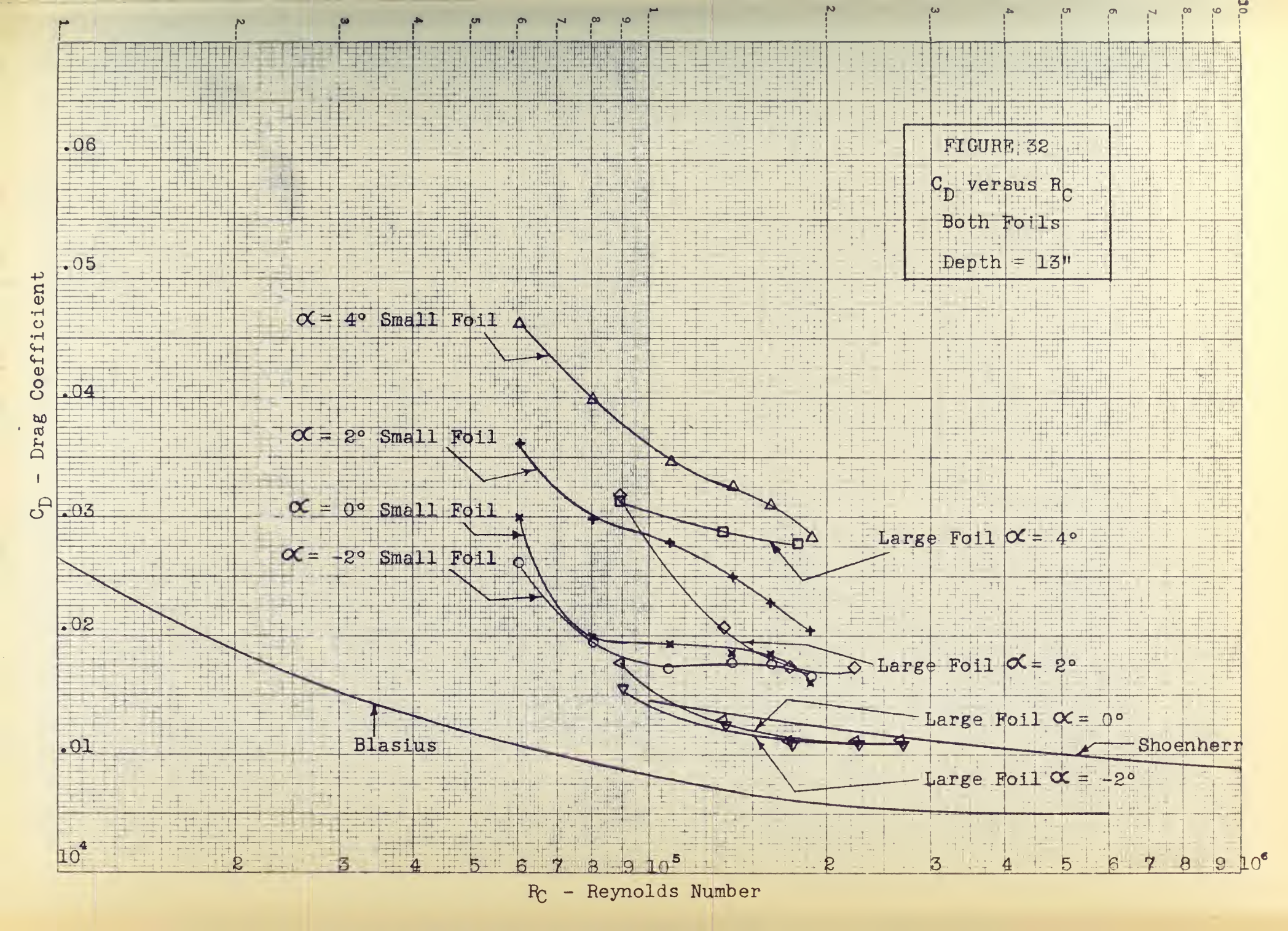
FIGURE 32
C_D versus R_C
Both Foils
Depth = 13"
C_D - Drag Coefficient
R_C - Reynolds Number
.06
.05
.04
.03
.02
.01
10^4
10^5
10^6
α = 4° Small Foil
α = 2° Small Foil
α = 0° Small Foil
α = -2° Small Foil
Large Foil α = 4°
Large Foil α = 2°
Large Foil α = 0°
Large Foil α = -2°
Blasius
Shoenherr

FIGURE 33

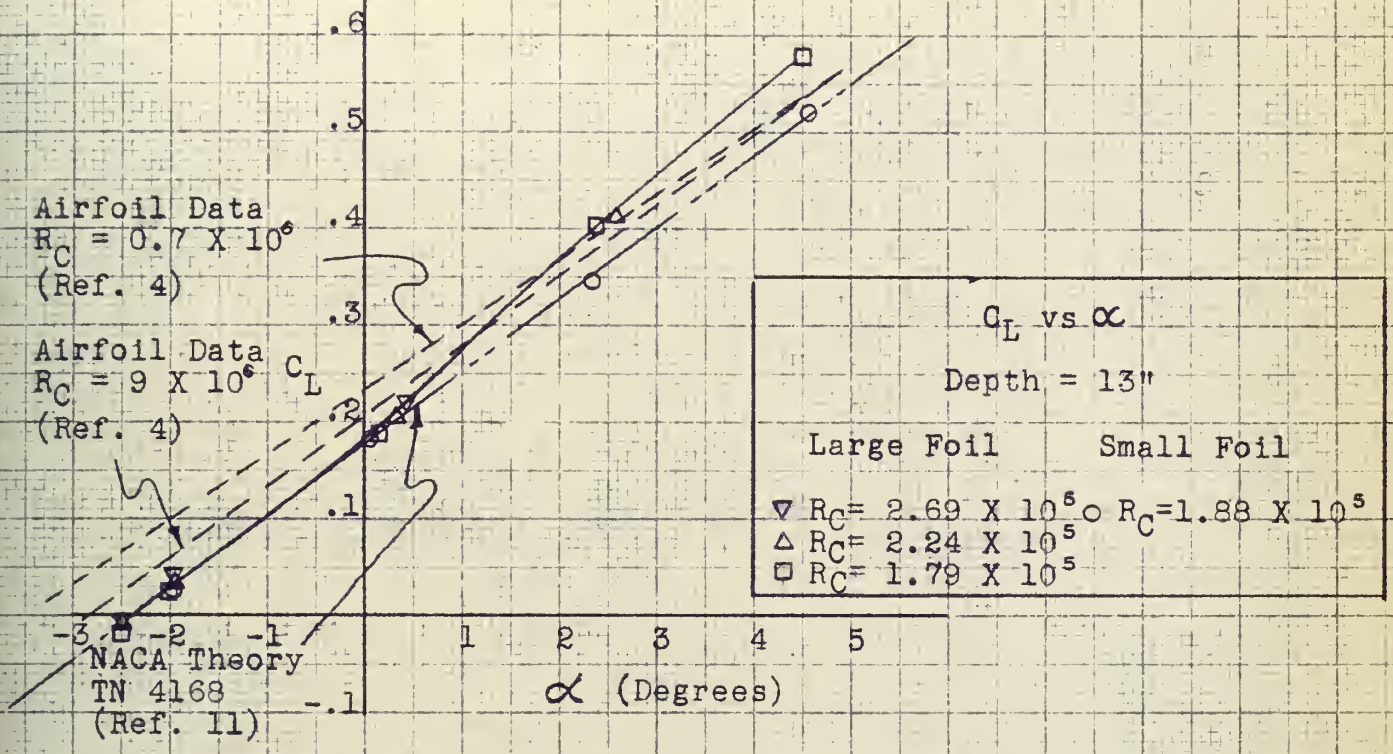
.6
.5
.4
.3
.2
.1
-.1
-3
-2
-1
1
2
3
4
5
C_L
α (Degrees)
Airfoil Data
R_C = 0.7 X 10^6
(Ref. 4)
Airfoil Data
R_C = 9 X 10^6
(Ref. 4)
NACA Theory
TN 4168
(Ref. 11)
C_L vs α
Depth = 13"
Large Foil
Small Foil
R_C= 2.69 X 10^5
R_C= 2.24 X 10^5
R_C= 1.79 X 10^5
R_C=1.88 X 10^5

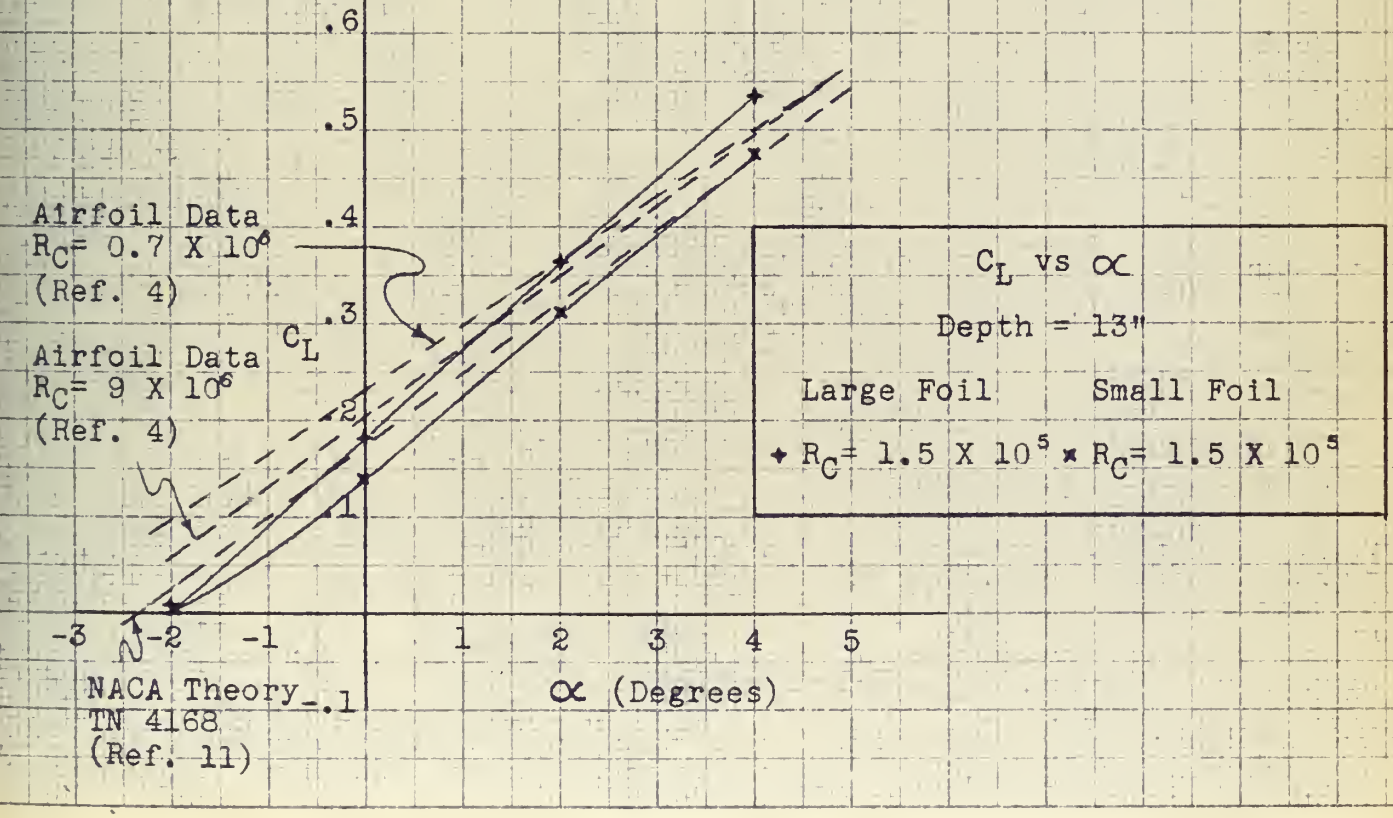
.6
.5
.4
.3
.2
.1
-.1
-3
-2
-1
1
2
3
4
5
C_L
α (Degrees)
Airfoil Data
R_C= 0.7 X 10^6
(Ref. 4)
Airfoil Data
R_C= 9 X 10^6
(Ref. 4)
NACA Theory
TN 4168
(Ref. 11)
C_L vs α
Depth = 13"
Large Foil
Small Foil
R_C= 1.5 X 10^5
R_C= 1.5 X 10^5

FIGURE 34

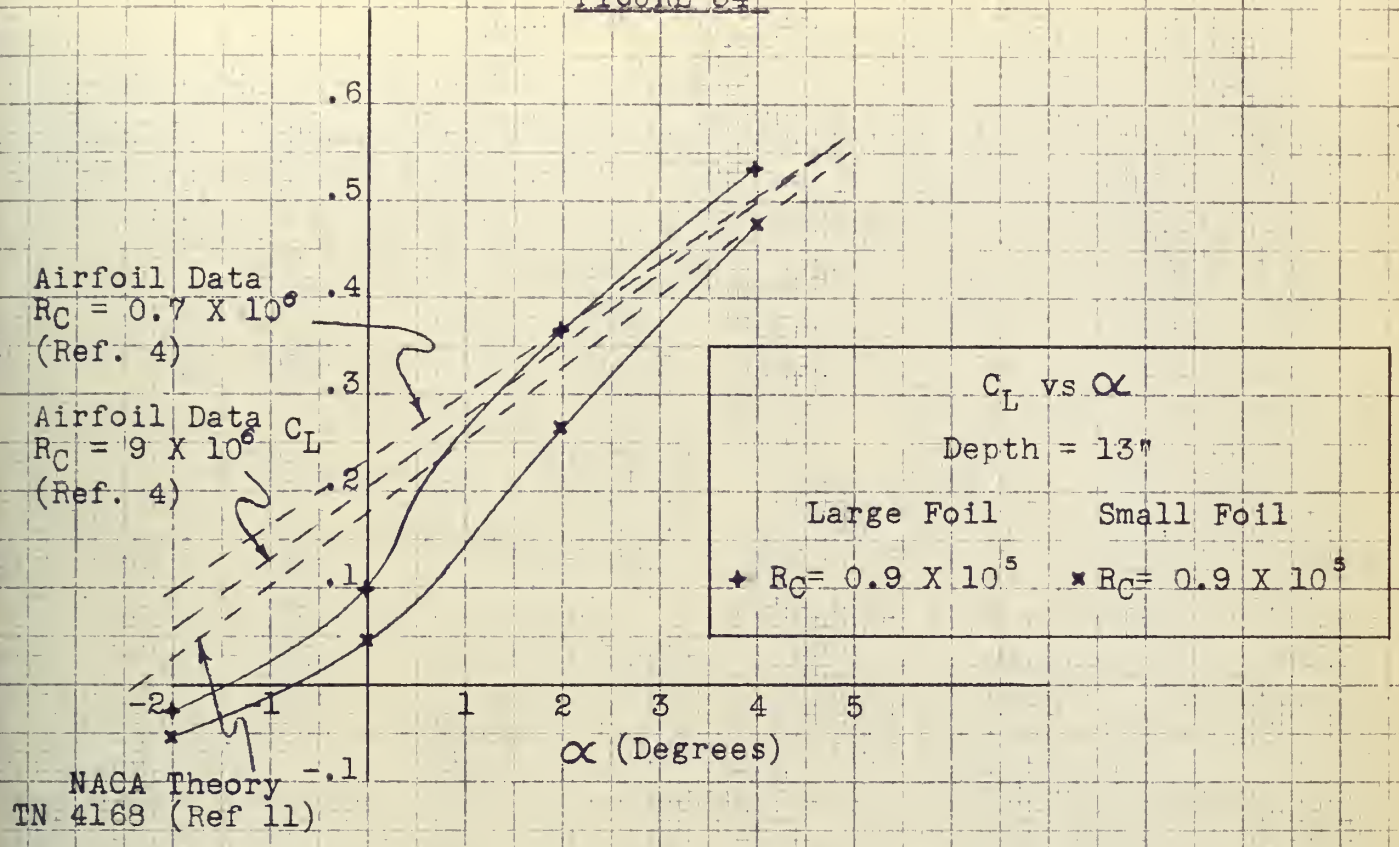
.6
.5
.4
.3
.2
.1
-.1
Airfoil Data
R_C = 0.7 X 10^6
(Ref. 4)
Airfoil Data
R_C = 9 X 10^6
(Ref. 4)
C_L
-2
-1
1
2
3
4
5
α (Degrees)
NACA Theory
TN 4168 (Ref 11)
C_L vs α
Depth = 13"
Large Foil
Small Foil
R_C= 0.9 X 10^5
R_C= 0.9 X 10^5

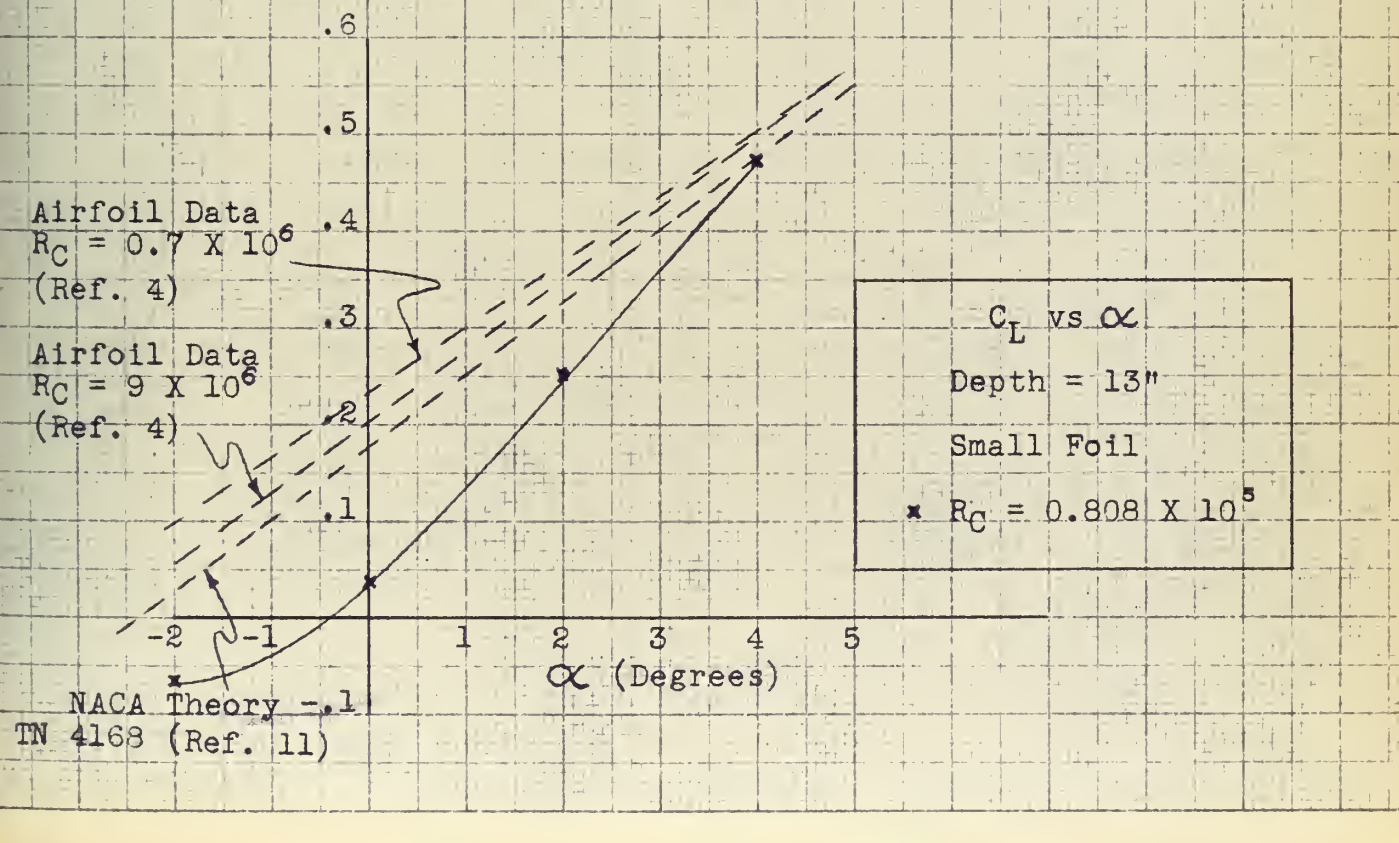
.6
.5
.4
.3
.2
.1
-.1
Airfoil Data
R_C = 0.7 X 10^6
(Ref. 4)
Airfoil Data
R_C = 9 X 10^6
(Ref. 4)
-2
-1
1
2
3
4
5
α (Degrees)
NACA Theory
TN 4168 (Ref. 11)
C_L vs α
Depth = 13"
Small Foil
R_C = 0.808 X 10^5

The foils display rather marked departures from wind tunnel data, particularly at the lower Reynolds numbers. The wind tunnel experiments show two trends resulting from Reynolds numbers variations. First, the slope of the lift curve decreases with decreasing Reynolds numbers. Second, the angle of zero lift becomes more negative with decreasing Reynolds numbers. Laminar separation has produced exactly the opposite effect in the case of the hydrofoils. The angle of zero lift has become less negative with decreasing Reynolds number while the average slope of the lift curve has increased. Figure 35 shows the change in angle of zero lift due to Reynolds number.

At the higher Reynolds numbers the theoretical method gives the best correlation with experimental results. It must be remembered, however, that an experimental angle of zero lift as measured on the test foils was used in conjunction with the theory. As Reynolds number is lowered the foils depart farther from theory until at $R_c = .808 \times 10^5$ the small foil shows a lift coefficient of .035 at $\alpha = 0$, while theory predicts $C_l = .178$. Thus over the Reynolds number range tested the experimental results show that in general theoretical methods are not even a good approximation of hydrofoil performance. This seems logical since all theoretical methods still retain the classical circulation theory as their basis. The authors feel that laminar separation in its essence dictates a change in certain assumptions which form the basis for the circulation theory. For example, if separation has already occured, it does not necessarily follow that the after stagnation point must remain at the trailing edge of the airfoil.

The foil drag coefficients are plotted in Figures 36 and 37. Wind tunnel data corrected to three dimensional flow is also shown. In Figure 36

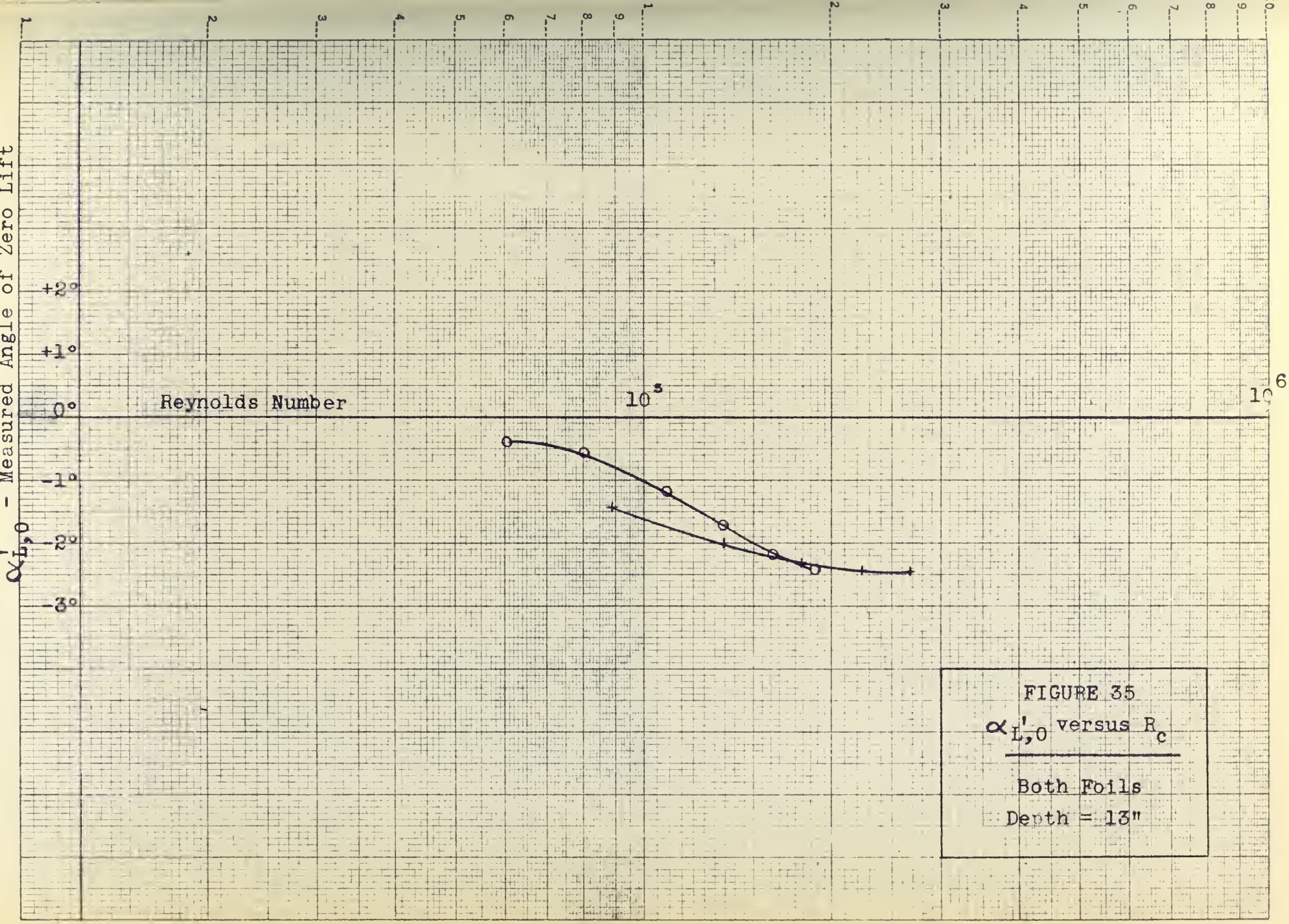

FIGURE 35

$\alpha'_{L,0}$ versus R_c

Both Foils

Depth = 13"

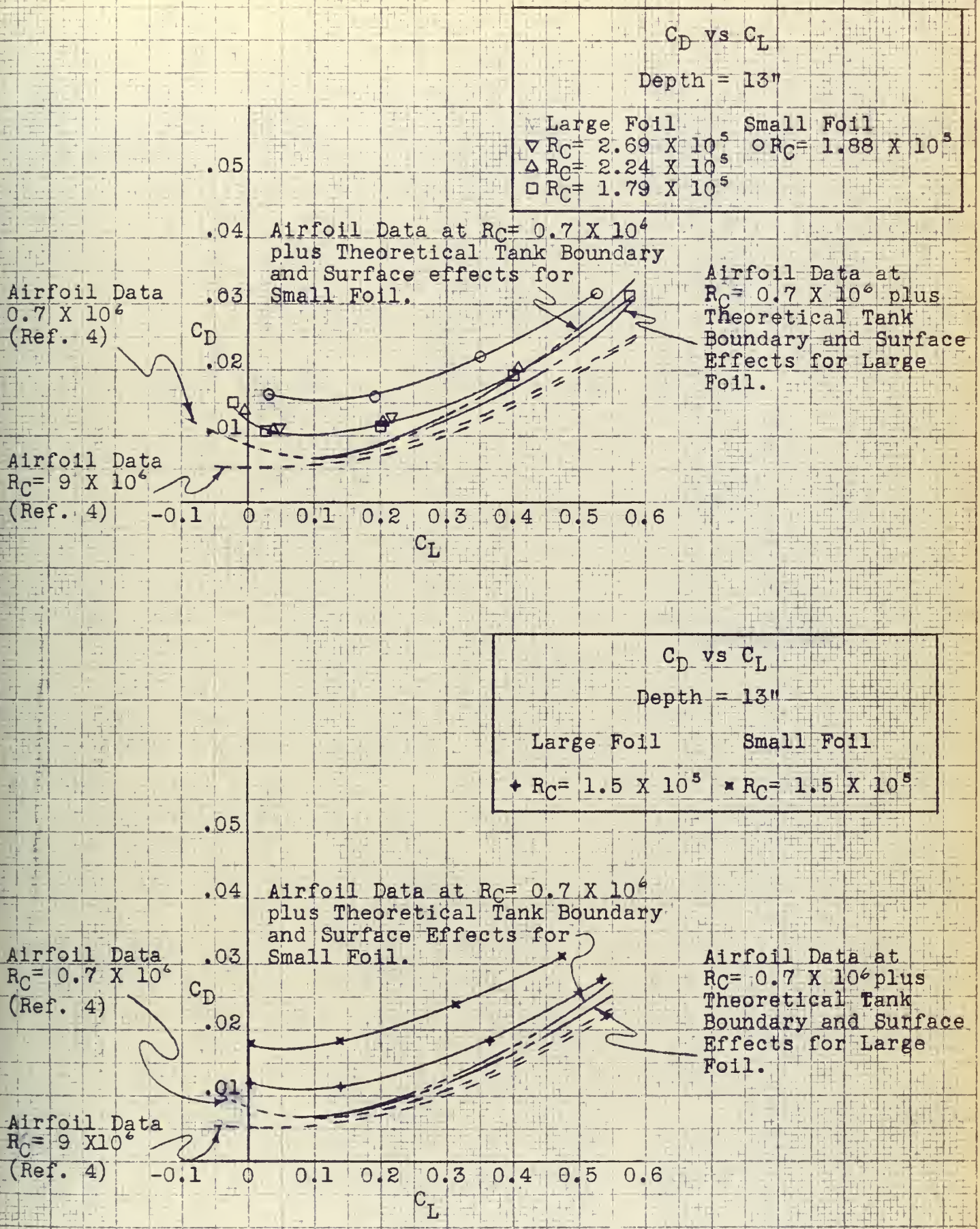
C_D vs C_L
Depth = 13"
Large Foil
▽ R_C= 2.69 X 10^5
△ R_C= 2.24 X 10^5
□ R_C= 1.79 X 10^5
Small Foil
○ R_C= 1.88 X 10^5
Airfoil Data at R_C= 0.7 X 10^6 plus Theoretical Tank Boundary and Surface effects for Small Foil.
Airfoil Data at R_C= 0.7 X 10^6 plus Theoretical Tank Boundary and Surface Effects for Large Foil.
Airfoil Data 0.7 X 10^6 (Ref. 4)
Airfoil Data R_C= 9 X 10^6 (Ref. 4)
C_D
.05
.04
.03
.02
.01
-0.1 0 0.1 0.2 0.3 0.4 0.5 0.6
C_L
C_D vs C_L
Depth = 13"
Large Foil
✦ R_C= 1.5 X 10^5
Small Foil
✖ R_C= 1.5 X 10^5
Airfoil Data at R_C= 0.7 X 10^6 plus Theoretical Tank Boundary and Surface Effects for Small Foil.
Airfoil Data at R_C= 0.7 X 10^6 plus Theoretical Tank Boundary and Surface Effects for Large Foil.
Airfoil Data R_C= 0.7 X 10^6 (Ref. 4)
Airfoil Data R_C= 9 X 10^6 (Ref. 4)
C_D
.05
.04
.03
.02
.01
-0.1 0 0.1 0.2 0.3 0.4 0.5 0.6
C_L

FIGURE 36

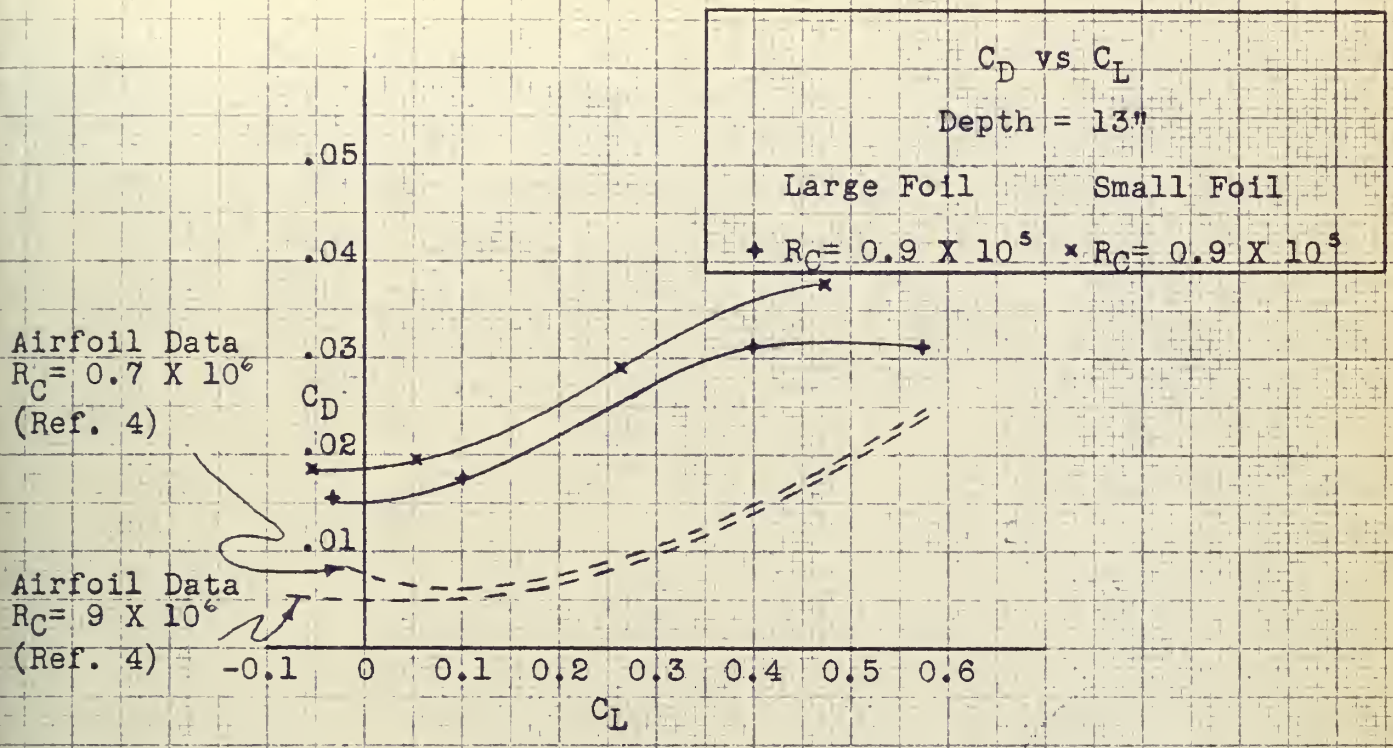
C_D vs C_L
Depth = 13"
Large Foil
Small Foil
+ R_C= 0.9 X 10^5
× R_C= 0.9 X 10^5
Airfoil Data
R_C= 0.7 X 10^6
(Ref. 4)
Airfoil Data
R_C= 9 X 10^6
(Ref. 4)
.05
.04
.03
.02
.01
C_D
-0.1
0
0.1
0.2
0.3
0.4
0.5
0.6
C_L

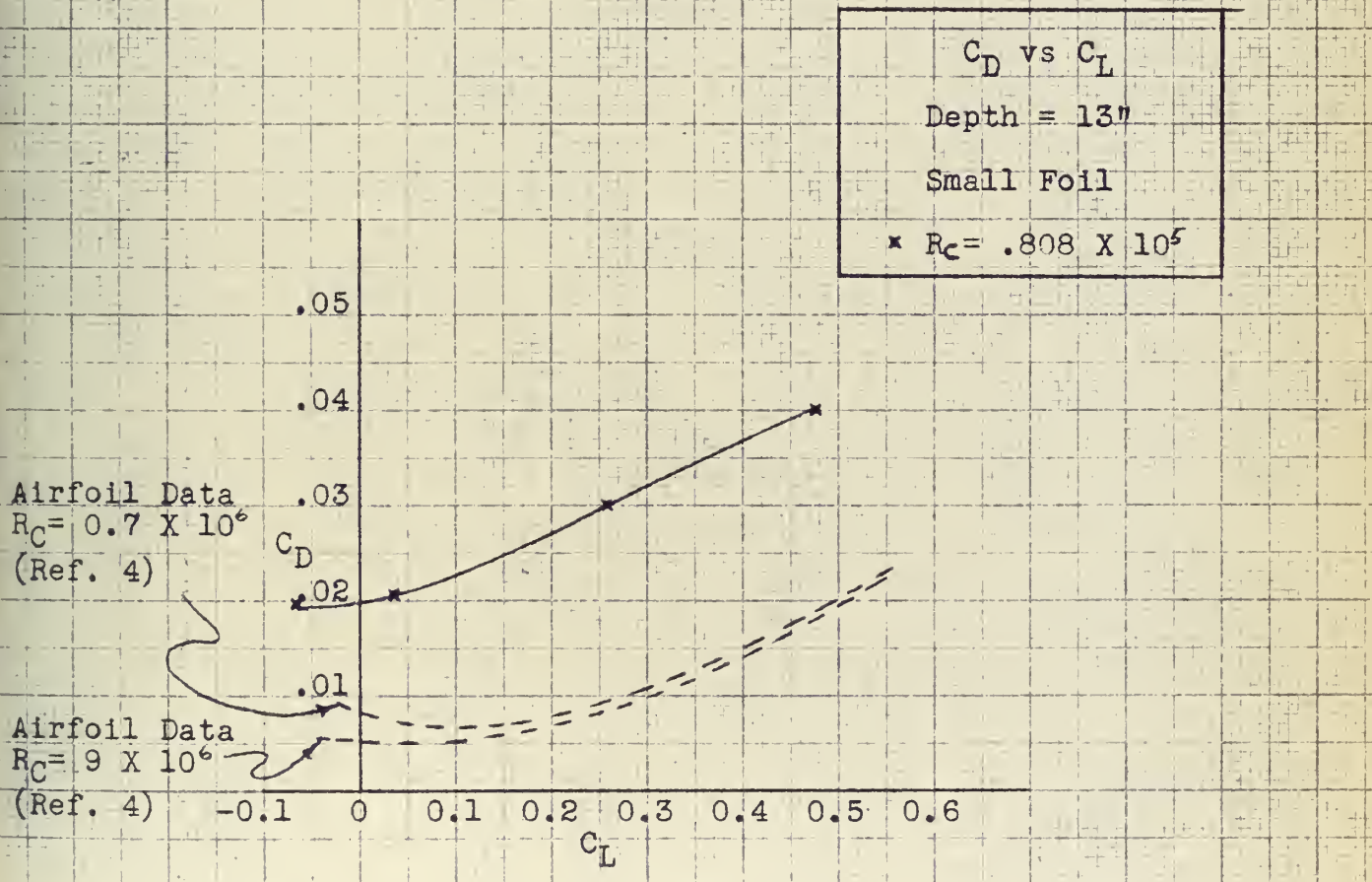
C_D vs C_L
Depth = 13"
Small Foil
× R_C= .808 X 10^5
Airfoil Data
R_C= 0.7 X 10^6
(Ref. 4)
Airfoil Data
R_C= 9 X 10^6
(Ref. 4)
.05
.04
.03
.02
.01
C_D
-0.1
0
0.1
0.2
0.3
0.4
0.5
0.6
C_L

FIGURE 37

wind tunnel data as measured at $R_c = 0.7 \times 10^6$ has been altered to also include the effects of tank boundary and wavemaking. To make these corrections foil velocities corresponding to foil Reynolds numbers of 2.0×10^5 and 1.5×10^5 were used. Both foils have drag coefficients which are consistently higher than the wind tunnel drag obtained at higher Reynolds numbers. Furthermore, the small foil drag coefficient is consistently higher than that of the large foil, and for a given Reynolds number this difference is almost constant for all lift coefficients.

The wind tunnel data corrected to include tank boundary and surface wavemaking effects begins to approach the foil drag coefficients at the higher lift coefficients. Since the boundary effects are small, this might lead one to suspect surface wavemaking as the cause of increased hydrofoil drag. The wave drag is, of course, a function of Froude number. Since, when operating at equal Reynolds numbers, the foils have quite different Froude numbers, wave drag could also be responsible for the differences in drag on the two foils. The theory, however, states that surface wavemaking is a function of circulation and therefore would not affect the drag at the angle of zero lift. Moreover, at the angle of zero lift, there is no induced drag.

The foil drag coefficients at $C_l = 0$ are plotted in Figure 28. Since there is still a large discrepancy in drag coefficients for the small foil as opposed to the large foil, we must conclude that surface wavemaking effects have not produced this anomaly. It is also interesting to note that the drag coefficient curves for both foils are initially flat and do not rise with decreasing Reynolds number parallel to either the Shoenherr or Blasius friction lines. Neither do they appear to be an extension of the

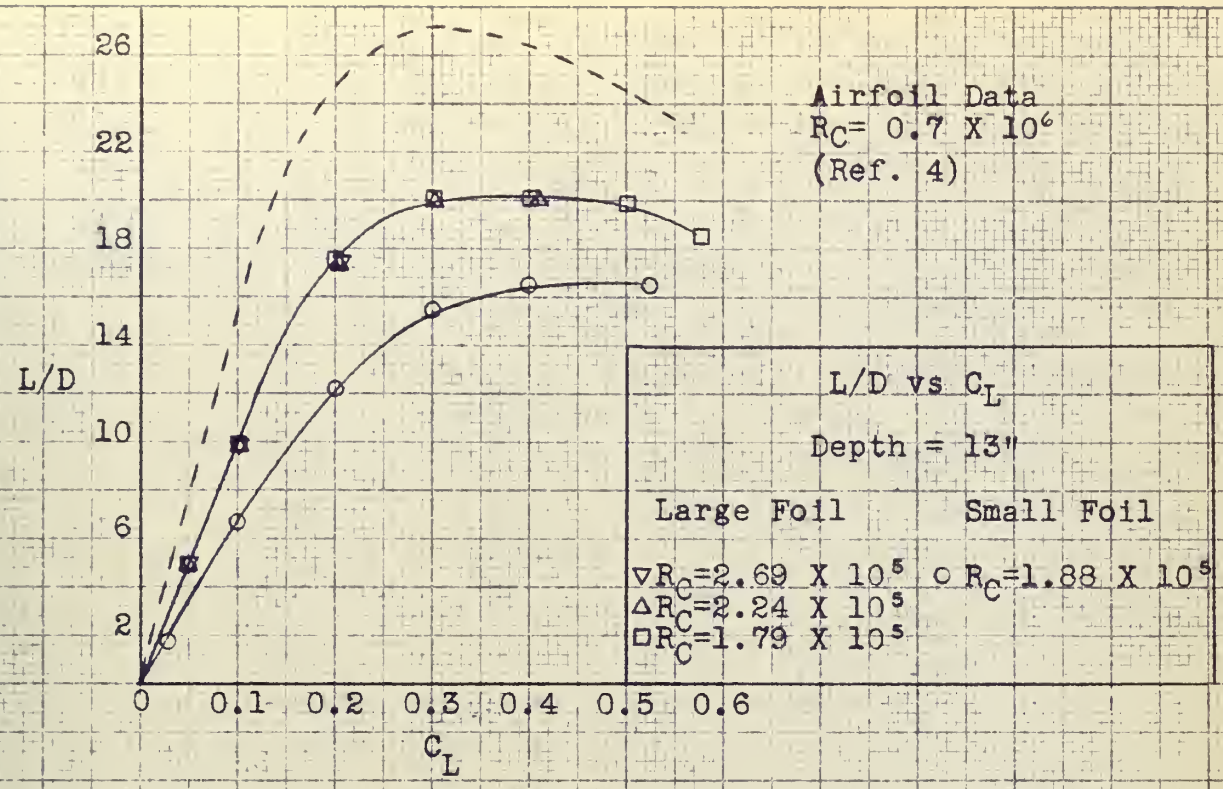
26
22
18
14
10
6
2
L/D
0
0.1
0.2
0.3
0.4
0.5
0.6
C_L
Airfoil Data
R_C= 0.7 X 10^6
(Ref. 4)
L/D vs C_L
Depth = 13"
Large Foil
Small Foil
▽R_C=2.69 X 10^5
△R_C=2.24 X 10^5
□R_C=1.79 X 10^5
○ R_C=1.88 X 10^5

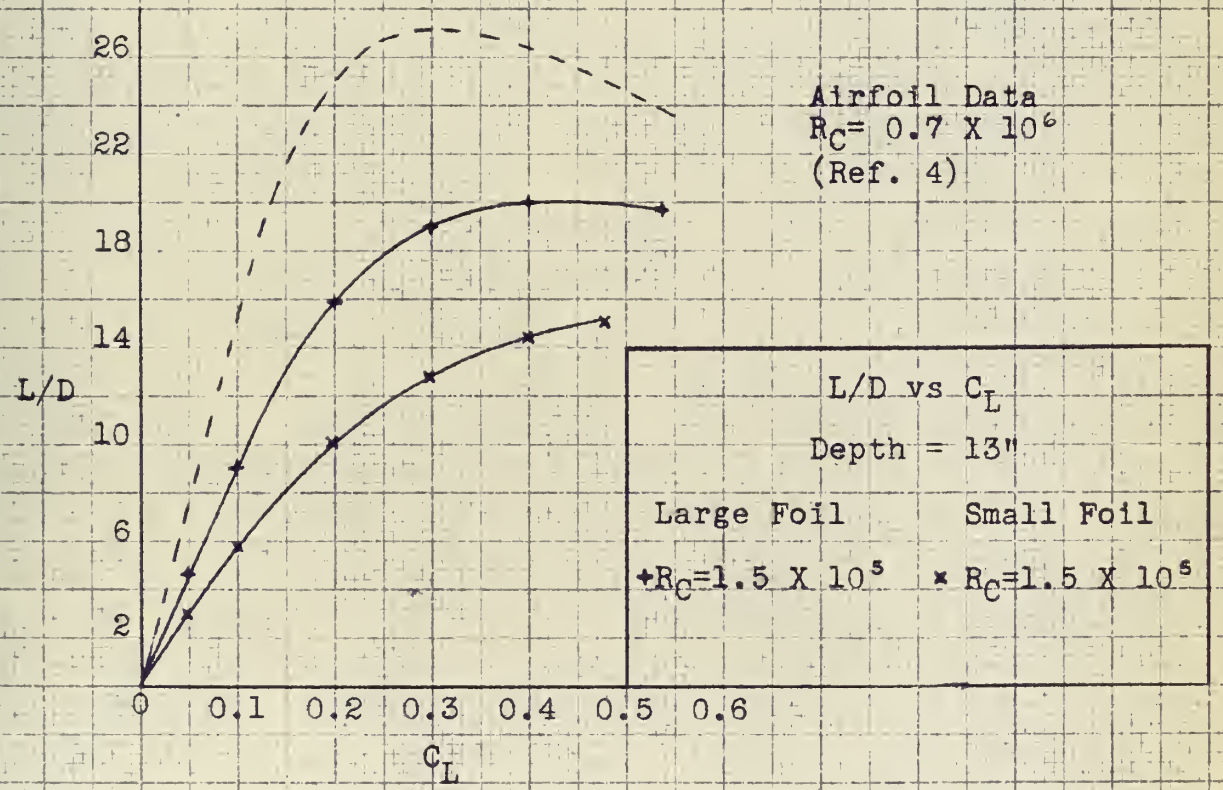
26
22
18
14
10
6
2
L/D
0
0.1
0.2
0.3
0.4
0.5
0.6
C_L
Airfoil Data
R_C= 0.7 X 10^6
(Ref. 4)
L/D vs C_L
Depth = 13"
Large Foil
Small Foil
+R_C=1.5 X 10^5
× R_C=1.5 X 10^5

FIGURE 38

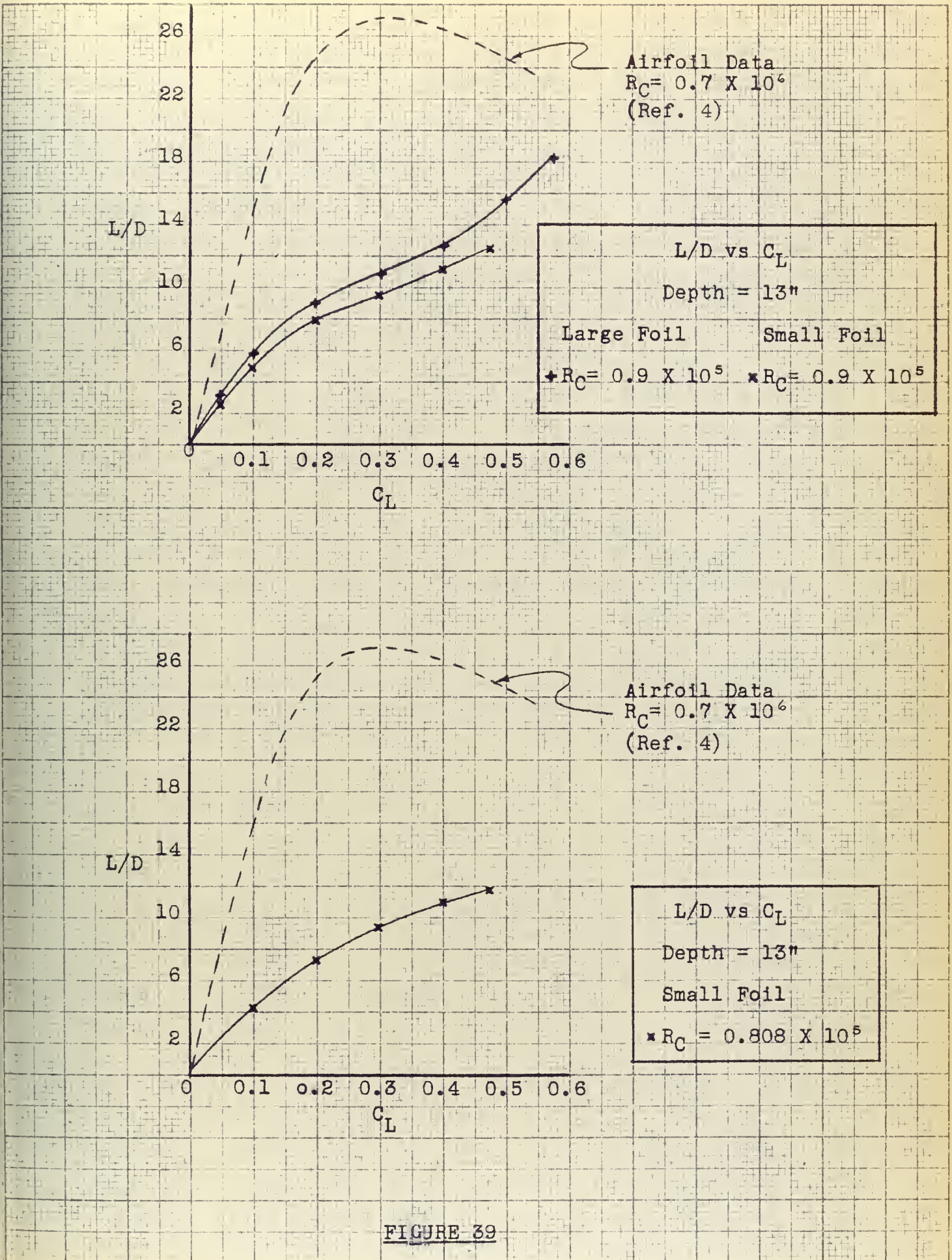
26
22
18
14
10
6
2
0
L/D
0.1
0.2
0.3
0.4
0.5
0.6
C_L
Airfoil Data
R_C= 0.7 X 10^6
(Ref. 4)
L/D vs C_L
Depth = 13"
Large Foil
Small Foil
+ R_C= 0.9 X 10^5
× R_C= 0.9 X 10^5
Airfoil Data
R_C= 0.7 X 10^6
(Ref. 4)
L/D vs C_L
Depth = 13"
Small Foil
× R_C = 0.808 X 10^5

FIGURE 39

wind tunnel tests of the same section at higher Reynolds numbers. Figure 28 also shows that laminar flow, contrary to popular opinion, does not always produce drag coefficients of less magnitude than turbulent flow even on extremely thin bodies.

The curves of possibly the greatest interest are shown in Figures 38 and 39. These figures portray most vividly the overall influence of laminar separation on airfoil performance. At the design lift coefficient (C_l = .4) the L/D ratio varies from a maximum of 20 for the large foil at R_c = 2.69 X 10^5 to 11 for the small foil at R_c= .808 X 10^5. A glance at the Reynolds number range calculated for the model propeller used in the Series 60 tests (page 2) indicates that experiments conducted at higher Reynolds numbers could not accurately predict the performance of the propeller behind the model. The test results also indicate that laminar separation could cause a marked reduction in the L/D ratio of a ship model rudder or control fin. Therefore, care must be exercised in expanding the results of maneuvering tests directly to the full size ship

V. CONCLUSIONS

1. Neither two dimensional airfoil data taken at high Reynolds numbers nor current hydrofoil theory were adequate to predict the hydrodynamic characteristics of the test hydrofoils in the range $R_c = 0.8 \times 10^5$ to $R_c = 2.7 \times 10^5$. The marked variations in lift, drag and angle of zero lift due to laminar separation caused the predictions based on theory and airfoil data to be inaccurate. The lift coefficient versus angle of attack curve is normally a straight line in wind tunnel tests. In these tests, however, a hollow developed in the vicinity of $\alpha = 0^\circ$, which became more pronounced as Reynolds number decreased. For example, at $\alpha = 0^\circ$, the lift coefficient of the small foil varied from $C_l = 0.18$ at $R_c = 1.89 \times 10^5$ to $C_l = 0.04$ at $R_c = 0.8 \times 10^5$. Corresponding lift coefficient predictions by theory and from airfoil data were $C_l = 0.18$ and $C_l = 0.232$ respectively. Where lift predictions were generally higher than experimental values, the drag predictions were low. At the design lift coefficient, $C_l = 0.4$, the drag prediction based on airfoil data was $C_d = 0.015$. Experimental drag varied from $C_d = 0.036$ at $R_c = 0.8 \times 10^5$ down to $C_d = 0.019$ at $R_c = 2.7 \times 10^5$. The prediction problem is further complicated by the variation in the angle of zero lift. In these tests the angle of zero lift varied from -2.48° at $R_c = 2.7 \times 10^5$ to -0.6° at $R_c = 0.8 \times 10^5$. In general, the investigations lead one to believe that certain assumptions which form the basis for the circulation theory are no longer valid in the laminar flow region.

2. At a Reynolds number of 1.75×10^5 the small foil had a drag coefficient of 0.0176 at $C_l = 0$, while the large foil had a drag coefficient of 0.01275 at $C_l = 0$. This variation was almost constant over a Reynolds number range

of 0.9×10^5 to 1.9×10^5. Since the lift coefficient is zero, there is theoretically no wave drag or induced drag present. One must conclude, therefore, that equal Reynolds numbers based on free stream velocity and chordal length of geometrically similar shapes do not dictate flow similarity. This adds another variable to describe fluid flow in the laminar flow range. At present, there is no explanation of this apparent anomaly. The authors believe the first efforts of future research in this field should be directed toward the solution of this problem.

3. Experimental results for both strut and foils verify the fact that there is a major increase in profile drag due to laminar flow and subsequent laminar separation. This is contrary to the common belief that laminar flow always produces a reduction in drag. In the case of the strut at $R_c = 10^5$, the drag coefficient was 7.5 times the value given for turbulent skin friction by the Schoenherr line. This indicates that extreme care must be taken in expanding the resistance values of appendages on ship models. Heretofore, appendage resistance has been a small percentage of the total, but with more recent additions such as stabilizing fins, anti-pitch fins, and large sonar domes in the case of Naval vessels, this percentage is bound to increase.

4. The L/D ratios of the hydrofoils at design lift coefficient ($C_l = 0.4$) varied from a maximum of 20 on the large foil at $R_c = 2.69 \times 10^5$ to 11 for the small foil at $R_c = 0.808 \times 10^5$. The wind tunnel data indicates an L/D ratio of 26 at $R_c = 0.7 \times 10^6$. This Reynolds number range is representative of that found from root to tip over a ship model propeller blade. It is apparent, therefore, that model propeller experiments conducted at higher Reynolds numbers cannot accurately predict the propeller performance in the laminar

flow range. It is also apparent that laminar separation could cause a marked reduction in the L/D ratio of a ship model rudder or control fin. Therefore, care must be exercized in expanding the results of manuevering tests directly to the full size ship.

REFERENCES

AND

APPENDICES

****

REFERENCES

1. Glauert, H.: The Elements of Aerofoil and Airscrew Theory. Second ed., Cambridge University Press, 1947 (Reprinted 1948)

2. Reid, Elliott G.: Applied Wing Theory. First ed., McGraw-Hill Book Co., Inc., 1932.

3. Hoerner, S. F.: Aerodynamic Drag. The Otterbein Press, 1951.

4. Loftin, Lawrence K., Jr., and Smith, Hamilton A.: Aerodynamic Characteristics of 15 NACA Airfoil Section at Seven Reynolds Numbers 0.7×10^6 to 9.0×10^6. NACA TN 1945, 1949.

5. Ramsen, John A. and Vaughan, Victor L., Jr.: Hydrodynamic Tares and Interference Effects for a 12-Percent-Thick Surface-Piercing Strut and an Aspect-Ratio-0.25 Lifting Surface. NACA TN 3420, 1955.

6. Coffee, Claude W., Jr. and McKann, Robert E.: Hydrodynamic Drag of 12- and 21-Percent-Thick Surface-Piercing Struts. NACA TN 3092, 1953.

7. Wadlin, Kenneth L., Shuford, Charles L. and McGehee, John R.: A Theoretical and Experimental Investigation of the Lift and Drag Characteristics of Hydrofoils at Subcritical and Supercritical Speeds. NACA Report 1232, 1955.

8. Wadlin, Kenneth L., Fontana, Rudolph E. and Shuford, Charles L., Jr.: The Effect of End Plates, End Struts, and Depth of Submergence on the Characteristics of a Hydrofoil. NACA RM L51B13, 1951.

REFERENCES (Continued)

9. Wadlin, Kenneth L., Ramsen, John A. and McGehee, John R.: Tank Tests at Subcavitation Speeds of an Aspect-Ratio-10 Hydrofoil with a Single Strut. NACA RML9K14a, 1950.

10. Havelock, T. H.: Studies in Wave Resistance: Influence of the Form of the Water-Plane Section of the Ship. Proc. Roy. Soc. (London), ser. A, vol. 103, 1923.

11. Wadlin, Kenneth L. and Christopher, Kenneth W.: A Method for Calculation of Hydrodynamic Lift for Submerged and Planing Rectangular Lifting Surfaces. NACA TN 4168, 1958.

12. Abbott, Ira H., von Doenhoff, Albert E., and Stivers, Louis S., Jr.: Summary of Airfoil Data. NACA Report 824, 1945.

13. Quinn, John H., Jr. and Tucker, Warren A.: Scale and Turbulence Effects on the Lift and Drag Characteristics of the NACA 65_3-418, a = 1.0 Airfoil Section: NACA WR L-138, 1944. (Formerly NACA ACR L4H11.)

14. Wieghardt, Karl: Chordwise Load Distribution of a Simple Rectangular Wing. NACA TM 963, 1940.

15. Soracco, David L.: Design and Construction of a Two-Force Towing Balance for the Robinson Model Basin. 1957.

16. von Doenhoff, Albert E. and Horton, Elmer A.: A Low Speed Experimental Investigation of the Effect of a Sandpaper Type of Roughness on Boundary-Layer Transition. NACA TN 3858, 1956.

REFERENCES (Continued)

17. Hadler, J. B., Stuntz, G. R., and Pierr, P. C.: Propulsion Experiments on Single Screw Merchant Ship Forms - Series 60. SNAME - Transactions Vol. 62, 1954.

18. Murray, A. B., Korvin - Kroukovsky B. V., and Lewis, E. V.: Self Propulsion Tests with Small Models. SNAME Transactions Vol. 59, 1951.

APPENDIX I

STRUT AND FOIL DIMENSIONS AND SAMPLE CALCULATIONS

Appendix I contains a drawing of the strut and foil assembly, the hydrofoil offsets and sample calculations which show examples of the various arithmetic processes used in the main body of the report. They are arranged as follows:

A. Strut and Foil Dimensions.

1. Figure 1, a drawing of the strut and foil assembly.
2. Table of offsets for each foil.

B. Sample Calculations.

1. Strut Tests.
2. Foil Tests.
3. Calculations to Correct Experimental Foil Data to Final Plots.
4. Theoretical Strut Wave Drag.
5. Calculation of Strut Profile Drag.
6. Theoretical Strut Profile Drag.
7. The Classical Method for Correction of Airfoil Data.
8. The Modified Classical Method.
9. Two Dimensional Boundary Correction Factor, K_2.
10. Three Dimensional Boundary Correction Factor, K_3.
11. Theoretical Prediction of Lift Coefficient.

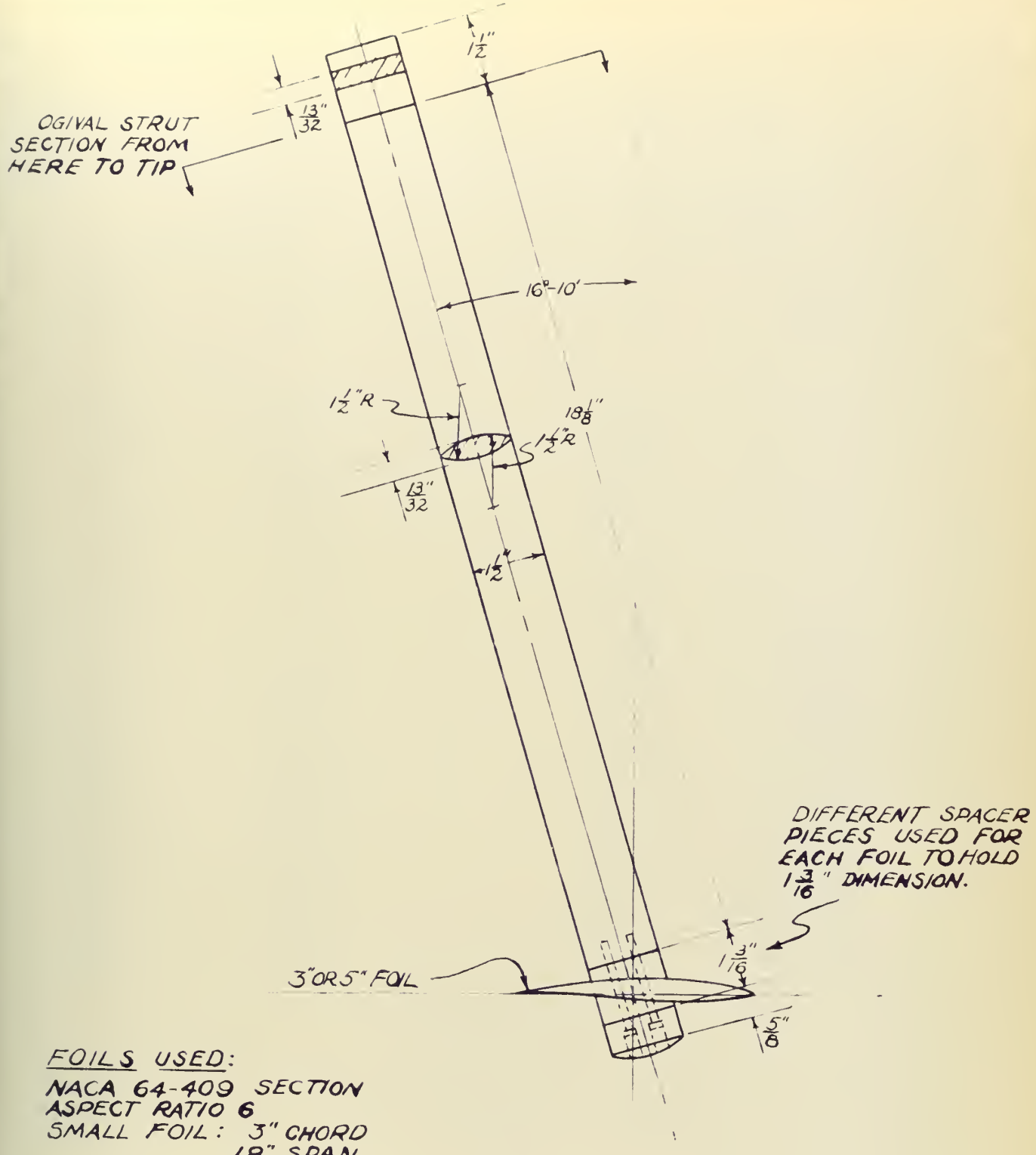

FOILS USED:

NACA 64-409 SECTION
ASPECT RATIO 6
SMALL FOIL: 3" CHORD
18" SPAN
LARGE FOIL: 5" CHORD
30" SPAN

FIGURE 1 - APPENDIX I
STRUT & FOIL ASSEMBLY
SCALE: 1/3" = 1" 21 MAY 1958
L.F. HICKS W.J. MAHONY

Ordinates for NACA 64-409 Airfoil Section

(From Reference 15)

Chord = 3" Span = 18" Foil tips rounded off

UPPER SURFACE		LOWER SURFACE	
Station (in.)	Ordinate (in.)	Station (in.)	Ordinate (in.)
0	0	0	0
0.0113	0.02487	0.0187	-0.01887
0.0184	0.03063	0.0266	-0.02223
0.0328	0.03993	0.0422	-0.02709
0.0696	0.05685	0.0803	-0.03453
0.1441	0.08196	0.1559	-0.04404
0.2189	0.10149	0.2311	-0.05061
0.2939	0.11775	0.3061	-0.05571
0.4443	0.14388	0.4557	-0.06312
0.5949	0.16368	0.6051	-0.06817
0.7456	0.17871	0.7544	-0.07131
0.8965	0.18945	0.9035	-0.07281
1.0473	0.19614	1.0526	-0.07254
1.1983	0.19896	1.2017	-0.07044
1.3492	0.19662	1.3508	-0.06522
1.5000	0.19026	1.5000	-0.05790
1.6501	0.18048	1.6493	-0.04908
1.8013	0.16782	1.7986	-0.03930
1.9518	0.15255	1.9482	-0.02895
2.1021	0.13512	2.0979	-0.01848
2.2522	0.11574	2.2478	-0.00834
2.4021	0.09462	2.3979	+0.00090
2.5518	0.07239	2.5483	+0.00837
2.7013	0.04932	2.6987	+0.01272
2.8506	0.02574	2.8494	+0.01218
3.0000	0	3.0000	0

Leading edge radius = 0.01737 inches

Slope of radius through leading edge = 0.00504

Ordinates for NACA 64-409 Airfoil Section

(From Reference 15)

Chord = 5" Span = 30" Foil tips rounded off

UPPER SURFACE		LOWER SURFACE	
Station (in.)	Ordinate (in.)	Station (in.)	Ordinate (in.)
0	0	0	0
0.01885	0.04145	0.03115	-0.03145
0.03065	0.05105	0.04435	-0.03705
0.05475	0.06655	0.07025	-0.04515
0.11610	0.09475	0.13390	-0.05755
0.24015	0.13660	0.25985	-0.07340
0.36485	0.16915	0.38515	-0.08435
0.48990	0.19625	0.51010	-0.09285
0.74050	0.23980	0.75950	-0.10520
0.99150	0.27280	1.0085	-0.11360
1.24270	0.29785	1.2573	-0.11885
1.49410	0.31575	1.5059	-0.12135
1.7456	0.32690	1.7544	-0.12090
1.9971	0.33160	2.0029	-0.11740
2.2486	0.32770	2.2514	-0.10870
2.5000	0.31710	2.5000	-0.09650
2.7512	0.30080	2.7488	-0.08180
3.0022	0.27970	2.9977	-0.06550
3.2530	0.25425	3.2470	-0.04825
3.5034	0.22520	3.4965	-0.03080
3.7536	0.19290	3.7464	-0.01390
4.0034	0.15770	3.9965	+0.00150
4.2529	0.12065	4.2470	+0.01395
4.5021	0.08220	4.4978	+0.02120
4.7510	0.04290	4.7489	+0.02030
5.0000	0	5.0000	0

Leading edge radius = 0.02895 inches

Slope of radius through leading edge = 0.00840

SAMPLE CALCULATIONS

1. Strut Tests

$\alpha = 0°$ (Strut positioned to give a foil angle of attack of 0°)

f = 13.65" (Immersed area corresponds to a foil depth of 13")

Strut Drag

Run	Time (sec)	V ft/sec	V^2	Scale Reading	Spring Force (lb)	Pan Wt. (lb)	Total Drag (lb)	D_S= 0.87 Total (lb)	D_S/V^2
7	8.72	4.01	16.1	-0.1	.147	0.15	0.297	0.259	.016

Strut Lift

Run	Time (sec)	V ft/sec	V^2	Scale Reading	Spring Force (lb)	Pan Wt. (lb)	L_S* (lb)	L_S/V^2
13	8.66	4.04	16.4	0	.139	-.07	.069	.00421

* All Lift forces measured on the strut are negative

2. Foil Tests

Large Foil $\alpha = 0°$ f = 13" Tank Temp = 80° F

S = 150 in^2 $\frac{1}{2}\rho S$ = 1.006 $lb\text{-}sec^2/ft^2$ $C_l' = L'/\frac{1}{2}\rho SV^2$

Lift

Run	Time (sec)	V ft/sec	V^2	Scale Reading	Spring Force (lb)	Pan Wt. (lb)	L' (lb)	L'/V^2	C_l'
12	8.60	4.07	16.6	0	.157	3.1	3.257	.1965	.1961

Drag $C' = D'/\frac{1}{2}\rho SV^2$

Run	Time (sec)	V ft/sec	V^2	Scale Reading	Spring Force (lb)	Pan Wt. (lb)	Total Drag (lb)	D'/V^2 0.87 Total/V^2	C_d'
9	8.65	4.04	16.4	+1.7	.315	.2	.515	.0273	.0272

3. Calculations to correct Experimental Foil Data for final plots

Large Foil $\alpha' = 0°$ f = 13" Tank Temp. = 80°F

Speed (ft/sec)	4	
C_1'	.194	From faired plot of Experimental Data
L_s/V^2	.00418	Figure 8
$\frac{1}{2}\rho S$	1.006	$\frac{1}{2}\rho S = \frac{1}{2} \times 1.9336 \times 150/144 = 1.006$
C_{ls}	.00416	$C_{ls} = L_s/V^2 \times 1/\frac{1}{2} S$
C_1	.1982	$C_1 = C_1' + C_{ls}$
L (lb)	3.18	$L = C_1 \frac{1}{2}\rho S V^2$
C_d'	.0273	From faired plot of Experimental Data
D_s/V^2	.0161	Figure 7
C_{ds}	.01605	$C_{ds} = D_s/V^2 \times \frac{1}{2} S$
C_d	.0112	$C_d = C_d' - C_{ds}$
D (lb)	.180	$D = C_d \frac{1}{2}\rho S V^2$
$\Delta\alpha_o°$	-.025	Figure 1
$\Delta\alpha_L°$	+.200	Figure 1
$\Delta\alpha_T°$	+.175	$\Delta\alpha_T = \Delta\alpha_L \pm \Delta\alpha_o$
$\alpha'°$	0	From Test Data
$\alpha°$	+.175	$\alpha = \alpha' \pm \Delta\alpha_T$
R_c	1.79×10^5	$R_c = Vc/\nu$

L/D vs C_1 Plots can be obtained very simply from the Plot of C_d vs C_1. $L/D = C_1/C_d$

4. Theoretical Strut Wavemaking Drag

Wavemaking drag was computed for the strut at $\alpha = 0°$, and f = 13.65" which gives an immersed area corresponding to a foil depth of 13". For the above conditions the projected strut area, S_s, is 22 sq. in.

b = .201 in

1 = .78 in

Basic Strut Equation:

$$D_{sw} = \frac{512}{\pi} g \rho b^2 l^2 \left\{ \left(\frac{1}{144} p - \frac{1}{5760} p^3 + \cdots \right) \log \frac{2}{\gamma p} + \frac{7}{576} p - \frac{161}{2073600} p^3 + \cdots \right\}$$

Col.	V (ft/sec)	4
	p	.261
(1)	$p \times 10^3/144$	1.81
(2)	$-p^3 \times 10^3/5760$	-
(3)	(1) -(2)	1.81
(4)	$\log 2/\gamma p$	2.59
(5)	(4)X (1)-(2)	4.68
(6)	$7p \times 10^3/576$	3.17
(7)	(5) + (6)	7.85
(8)	$161p^3/2073600$	-
(9)	(7) - (8)	7.85
(10)	$512/\pi$	163
(11)	(9) X (10) = $\frac{D_{sw} \times 10^3}{g \rho b^2 l}$	1280

4. (cont.)

$$D_{sw} = \frac{1280 \times 32.2 \times 1.9336 \times (.201)^2 \times .78}{10^3 \times 1728}$$

$$= .001451 \text{ lbs}$$

$$C_{ds,w} = D_{sw} / \tfrac{1}{2} \rho S V^2 = \frac{.001451 \times 144}{\frac{1}{2} \times 1.9336 \times 22 \times 16}$$

$$= .000614$$

$$R_c = 2V1/\nu = \frac{4 \times 1.56}{12 \times .92969 \times 10^{-5}} = .559 \times 10^5$$

5. Calculation of Strut Profile Drag

V (ft/sec)	4
D_s/V^2	.01610
C_{ds}	.1088
D_{sw}	.00145
$C_{ds,w}$	.000614
C_{dp}	.1082
R_c	$.559 \times 10^5$

Figure 7

$C_{ds} = D_s / \tfrac{1}{2} \rho S_s V^2$ (In this case S_s = 22")

$C_{dp} = C_{ds} - C_{ds,w}$

6. Theoretical Strut Profile Drag

$$C_{dp} = 2C_f + (t/c)^2 - .0003$$

Where: C_f = Blasius Friction coefficient for laminar flow

$$C_f = 1.328/\sqrt{R_c}$$

Note that $2C_f$ is used since all calculations are based on projected strut area.

$$(t/c)^2 = (.402/1.56)^2 = (.258)^2 = .0665$$

7. The Classical Method for Correction of Airfoil Data for Aspect Ratio.

A sample solution of equations (4) and (5):

$$(4)\quad C_d = c_d + \frac{c_l^2}{A}(1+\delta)$$

$$(5)\quad \alpha = \alpha_o + \frac{c_l}{A}(1+\tau)$$

For both foils: A = 6, = 0.045, and = 0.165.

$$R_c = 9.0 \times 10^6$$

c_l	α_o(Deg.)	α_o(Rad.)	$0.618c_l$	α(Rad.)	α(Deg.)	c_d	$0.0554c_l^2$	C_d
0.68	4.0°	0.0696	0.0421	0.1117	6.42°	0.0069	0.0256	0.0325

8. The Modified Classical Method.

A sample solution of Equation (6):

$$(6)\quad C_d = c_d + c_l^2\left[\frac{(1+\delta)}{\pi A} + \frac{K_{1c}(1+\delta)}{8\pi} + \frac{1}{2V^2/gc}\psi\right]$$

For large foil at V = 4.45'/sec, c_l = 0.68.

It was necessary to solve first for the term $\frac{1}{2V^2/gc}\psi$

V	V^2	f'	f'g	$F = V^2/fg$	-2/F	$\psi = e^{-2/F}$	c	gc	V^2/gc	$\frac{1}{2V^2/gc}\psi$
4.45	19.82	1.0833	34.88	0.568	-3.52	0.0294	0.4167	13.418	1.478	0.0095

Note that f' is foil depth in feet.

Then the solution for C_d:

①	②	③	④	⑤	⑥	⑦	⑧	⑨	⑩	⑪	⑫	⑬
V	c_l	c_l^2	c_d	1+δ	$\frac{1+\delta}{\pi A}$	K_{1c}	$\frac{⑦ \times ⑤}{8\pi}$	$\frac{1\cdot\psi}{2V^2/gc}$	⑥ + ⑧ + ⑨	③ × ⑩	C_d = ④ + ⑪	$R_o \times 10^{-5}$
4.45	0.68	0.463	0.0108	1.045	.0554	0.1273	.00529	.00950	.07023	.0325	.0433	2.0

9. The Two Dimensional Boundary Correction Factor, K_2.

Sample solution for equation (9):

$$(9)\quad K_2 = \frac{a_{o,2}}{a_{o,1}} = \frac{1 + (4f/c)^2 + (4h/c)^2 + (4h/c)^2(4f/c)^2}{1 + 2(4h/c)^2 + (4f/c)^2(4h/c)^2}$$

For the large foil: $f = 13"$, $c = 5"$, $h = 47"$

$$f/c = 2.6,\ (4f/c)^2 = 4x(2.6)^2 = (10.4)^2 = 108.16$$

$$h/c = 9.4,\ (4h/c)^2 = 4x(9.4)^2 = (37.6)^2 = 1413.76$$

$$K_2 = \frac{1 + (108.16) + (1413.76) + (1413.76)(108.16)}{1 + 2(1413.76) + (1413.76)(108.16)}$$

$$K_2 = \frac{154,435.20}{155,640.80} = \underline{0.992}$$

10. Three Dimensional Boundary Correction Factor, K_3

Sample solutions for equations (10), (11), (12), (13) and (14)

$$(11)\quad w_a = \frac{\Gamma A}{\pi c}\left\{\frac{1}{\left[1+(4f/c)^2\right]\sqrt{1+(4f/c)^2+A^2}} + \frac{1}{\left[(4f/c)^2+A^2\right]}\left[1+\frac{1}{\sqrt{1+(4f/c)^2+A^2}}\right]\right\}$$

For the large foil: $A = 6$, $(4f/c)^2 = 108.16$

$$w_a = \frac{\Gamma 6}{\pi c}\left\{\frac{1}{(109.16)\sqrt{145.16}} + \frac{1}{(144.16)}\left[1+\frac{1}{\sqrt{145.16}}\right]\right\}$$

$$w_a = \frac{\Gamma}{\pi c}\ (0.049632)$$

$$(12)\quad w_b = \frac{\Gamma}{2\pi c}\left\{\frac{(2w/c)+A}{\sqrt{1+(2w/c)^2+2(2w/c)A+A^2}} - \frac{(2w/c)-A}{\sqrt{1+(2w/c)^2-2(2w/c)A+A^2}}\right.$$

$$\left. + \frac{1}{\left[(2w/c)+A\right]}\left[1+\frac{1}{\sqrt{1+(\left[2w/c\right]+A)^2}}\right] - \frac{1}{\left[(2w/c)-A\right]}\left[1-\frac{1}{\sqrt{1+(\left[2w/c\right]-A)^2}}\right]\right\}$$

For the large foil: $2w/c = 48$, $(2w/c)^2 = 2304$

10. (Cont.)

Combing the effects of both sides:

$$2w_b = \frac{\Gamma}{\pi c}\left\{\frac{54}{\sqrt{37 + 2304 + 576}} - \frac{42}{\sqrt{37 + 2304 - 576}} + \frac{1}{(54)}\left[1 + \frac{1}{\sqrt{1 + 2916}}\right] - \frac{1}{(42)}\left[1 + \frac{1}{\sqrt{1 + 1724}}\right]\right\}$$

$$2w_b = \frac{\Gamma}{\pi c}\ (-0.005404)$$

$$(13)\quad w_c = \frac{\Gamma A}{\pi c}\left\{\frac{1}{\left[1+(4h/c)^2\right]\sqrt{1+(4h/c)^2+A^2}} + \frac{1}{\left[(4h/c)^2+A^2\right]}\left[1+\frac{1}{\sqrt{1+(4h/c)^2+A^2}}\right]\right\}$$

$$w_c = \frac{6\Gamma}{\pi c}\left\{\frac{1}{(1414.76)\sqrt{1450.76}} + \frac{1}{(1449.76)}\left[1+\frac{1}{\sqrt{1450.76}}\right]\right\}$$

$$w_c = \frac{\Gamma}{\pi c}\ (0.004410)$$

$$(14)\quad w_4 = \frac{\Gamma}{2\pi S}\left[\sqrt{1 + A^2} + 2\right]$$

For the large foil:

$$w_4 = \frac{\Gamma}{2\pi S}\left[\sqrt{37} + 2\right] = \frac{\Gamma}{2\pi S}\left[6.083 + 2\right] = \frac{\Gamma}{2\pi S}\ (8.083)$$

Then the three dimensional boundary correction factor for the large foil is:

$$(10)\quad K_3 = \frac{\Gamma_2}{\Gamma_1} = \frac{a_2}{a_1} = \frac{1}{1 + \frac{w_a + 2w_b - w_c}{w_4}}$$

$$K_3 = \frac{1}{1 + \frac{\frac{\Gamma}{\pi c}\ (0.049632 - 0.004410 - 0.005404)}{\frac{\Gamma}{2\pi S}\ (8.083)}}$$

Since $2S/c = A = 6$: $\quad K_3 = \dfrac{1}{1 + \frac{6(0.039818)}{8.083}} = \dfrac{1}{1.02956} = \underline{0.9717}$

11. Theoretical Prediction of Lift Coefficient.

Sample solution of equation (7):

$$(7)\quad C_l = \frac{a_o A K_2 K_3 \alpha_a}{A + 1 + \frac{a_o K_2}{\pi}} + K_3 \frac{8}{3} (1 - A/10) \sin^2\alpha_a \cos\alpha_a$$

For the large foil: (Using theoretical angle of zero lift, $\alpha_{L,o}$.)

①	②	③	④	⑤	⑥	⑦	⑧	⑨	⑩
α (Deg)	α (Rad)	$\alpha_{L,o}$ (Rad)	α_a ②+③	K_2	K_3	A	a_o	$\frac{a_o K_2}{\pi}$	A+1+$\frac{a_o K_2}{\pi}$ ⑦+⑨+1
4.0°	0.0698	0.0638	0.1336	0.992	0.9717	6	6.283	1.984	8.984

⑪	⑫	⑬	⑭	⑮	⑯	⑰
$\frac{a_o A K_2 K_3 \alpha_a}{A + 1 + \frac{a_o K_2}{\pi}}$ ⑧⑤⑥⑦④÷⑩	$\sin\alpha_a$	$\sin^2\alpha_a$	$\cos\alpha_a$	A/10	(1-A/10)	$K_3\frac{8}{3}(1-A/10)\sin^2\alpha_a\cos\alpha_a$ ⑥·8/3·⑯·⑬·⑭
0.5401	.1329	0.0176	0.9859	0.6000	0.4000	0.0180

⑱
C_l ⑪+⑰
0.5581

Appendix II

MODIFICATIONS TO THE BALANCE

The authors are indebted to Lt. D. L. Soracco for his foresight and ingenuity in designing the Two Force Towing Balance used to conduct the tests which are the subject of this thesis. We can also appreciate the long hours of tedious work that he spent constructing, assembling and aligning the balance. Where we had four hands, he had two, which had to work very hard to bring the balance to the high state of development that we inherited. (See reference 15 for the description of the balance as completed by Lt. Soracco.) Since Lt. Soracco was unable to give his balance a thorough test, certain modifications and adjustments had to be accomplished before actual testing of hydrofoils could proceed. These modifications are the subject of this Appendix.

1. Installation of Stops and Clamps for Both Lift and Drag Sections.

Preliminary tank tests showed that the arcs of travel of both lift and drag sections were larger than was necessary for full scale pointer deflections. This excess travel allowed undesirable oscillations to build up at the beginning and end of each run. The oscillations were particularly objectionable in the drag section. In order to limit the arc of travel of the drag section, upper and lower stops were installed. The motion of the lift section was limited by the installation of an upper lift stop, the lower lift stop having been installed previously by Lt. Soracco. (Ref. 15)

The drag section was clamped at the mid-scale position by means of a long, knurl-headed screw that can be easily inserted or removed by hand. A clamp was made for the lift section, which positions the lift section at

mid-scale. This clamp securely holds the lower lift arm to the lower lift stop. An aluminum spacer block is inserted between the lift stop and lift section arm to properly position the lift force measuring mechanism. The lower lift stop was stiffened by the addition of a flange to prevent deflections caused by large lift forces. After the flange addition, it was necessary to move the stop aft in order to keep it clear of the spray from the strut.

2. Lift Section Calibration Knife Edge

A knife edge was installed on the upper arm of the lift section on which calibration weights could be hung. (See figure 5 of Appendix III demonstrating the lift section calibration.)

3. Lift and Drag Scales

Lift and drag scales were inked on glass drafting cloth and glued to plexiglass backings. These scales were then varnished, which increased their resistance to moisture and dirt. It is recommended that these scales be replaced by aluminum scales on which the markings have been inscribed and painted with a legible color. These scales should read from "0" at the lower extreme of pointer deflection to a large number at the upper extreme. The present presentation is confusing since the scales read both up and down from the "0" reading at mid-scale. The drag scale divisions should be spread to a larger interval if these scales are redesigned. Scale reading would be easier also, if both pointers were painted black.

4. Redesign of the Drag Counterbalance Arm

Lt. Soracco designed and installed an arm to support a counterbalance weight. The purpose of this attachment is to raise the center of gravity

of the balance to a point near the main fulcrum. The center of gravity was raised to improve the sensitivity of the balance. The arm as originally installed was canted forward, which not only moved the center of gravity vertically upward, but also horizontally forward. It was determined that the vertical movement of the center of gravity was all that could be controlled satisfactorily, so the counterbalance arm was repositioned to a vertical attitude.

During preliminary tank tests, the authors discovered aggravating shifts in the balance calibration between successive runs. These calibration shifts were caused by undesirable movement of balance components relative to each other. Joints between structural members of the balance were not as rigid as they should have been. Consequently, shifts of weights within the balance mechanism caused the calibration to be erratic. A portion of this erratic calibration was caused by the lack of rigidity of the counterbalance arm and of its attachment to the balance. The redesign of the arm embodied fixing the proper amount of counterbalance weight permanently to the tip of the arm and developing a more rigid method of attachment of the arm to the balance.

5. Installation of a Stiffening Bracket to Improve the Rigidity of the Drag Section.

The alterations to the counterbalance arm reduced, but did not eliminate, the calibration shifts. These puzzling jumps of the calibration curve persisted until the stiffening bracket pictured here was installed.

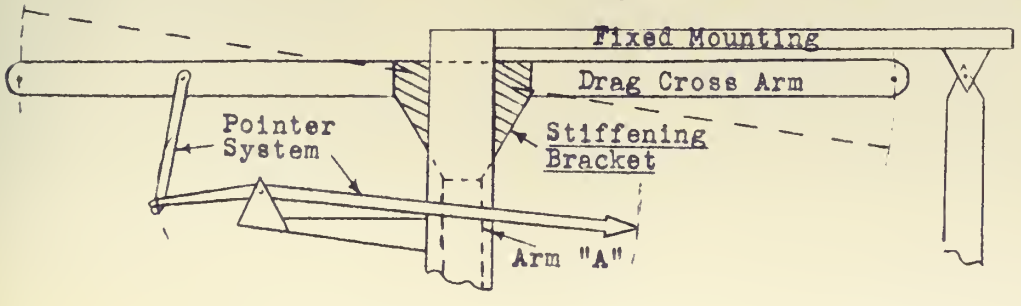

Schematic of Drag Force Measuring Mechanism Illustrating Stiffening Bracket Installation.

The drag cross arm was rotating relative to arm "A". (Ref. 15, page 20.) The rotation was caused by the high accelerations or decelerations at either the beginning or end of the runs. The bracket stiffened the joint enough to absorb these dynamic forces without rotation. Since the rigidity of this joint is a necessary condition for consistent calibration, religious attention should be given to maintaining the tightness of the screws which fix the bracket to the balance.

6. Securing the Lift Pointer to its Actuator Arm.

The lift pointer as originally designed was rotated by the force transmitted to it through a set screw on a small shaft. Since this joint was not sufficiently rigid, rotation of the pointer occured relative to its lever actuator. The pointer was firmly attached to this actuator arm by two small screws tapped into a flange type coupling. Since this same difficulty has been experienced occasionally with the drag pointer, it is recommended that it be altered similarly.

7. Strut Bracket Alteration to Permit Addition of Weights at High Angles of Attack.

It was found that the bracket, by which the angle of attack is adjusted, interfered with the addition of pan-weights to the lift section. Therefore, this bracket was cut to a shape that permitted the use of ten pounds on the positive lift peg.

8. Extension of the Lift Counterbalance Arm to Reduce Required Counterbalance Weight.

The foil-strut assembly has to be counterbalanced in the lift section to eliminate the weight of the assembly from the lift force measurement.

To facilitate this, while at the same time limiting the weight required, the upper lift arm was extended to lengthen the lever arm of the counterbalance weight. This extension reduced the amount of counterbalance weight required to balance the weight of the foil-strut assembly.

9. Provision of an Accurate Means to Measure the Angle of Attack.

During the preliminary testing, the accuracy of the angle of attack setting was dubious. Since the scribe marks on the angle of attack bracket were rough settings at best, some positive, accurate means to measure angle of attack had to be developed. The first attempt was a template to fit over the foil profiles. A pair of hook gauges were attached to the template, which were used to measure the level of the water surface. The angle of attack of the foils was calculated from the hook gauge measurements of the position of the water surface relative to the foils. It was impossible, however, to measure the strut angle of attack with this device, unless one of the foils were attached. Neither was the device considered sufficiently reliable to give the desired accuracy of $\pm 0.1^{\circ}$.

The NACA deserves the acknowledgement for suggesting the use of a gunner's quadrant to measure the angle of attack. The standard method used in the NACA tanks is to measure the strut incidence with a gunner's quadrant or similar device, and convert this reading to an angle of attack for the hydrofoil. Strut incidence is a function of the foil angle of attack, since the strut and foil intersect at a fixed angle. The angle of intersection between the chord lines of the test hydrofoils and the leading edge of the strut was measured with great care and found to be $73^{\circ}-50'$. ($\pm 0.1^{\circ}$). With this value known, it is quite convenient to convert the strut incidence angle to foil angle of attack.

While an accurate, rigid adjustment of angle of attack can be made with the present arrangement, the authors have experienced difficulty in making this adjustment. Therefore, an alteration to this mechanism would be highly desirable. A mechanism similar to that used to adjust the angle of an ordinary marine sextant could be adapted to the balance. This modification would save a great deal of the set-up time now required.

10. Installation of a Negative Lift Force Balance Weight Peg.

The installation of the negative lift force balance weight peg enabled the authors to balance the negative lift forces that were developed by the foils at negative angles of attack. Since this peg exhibits no parallel motion, its use was limited to small weights and to pointer deflections near mid-scale.

With the completion of the above modifications, the balance was used to obtain reliable results with the accuracy limits tabulated in Appendix III. The balance, as modified to the date of this writing, is shown in the following figures:

Figure 1

Balance with large foil attached as viewed from right - front.

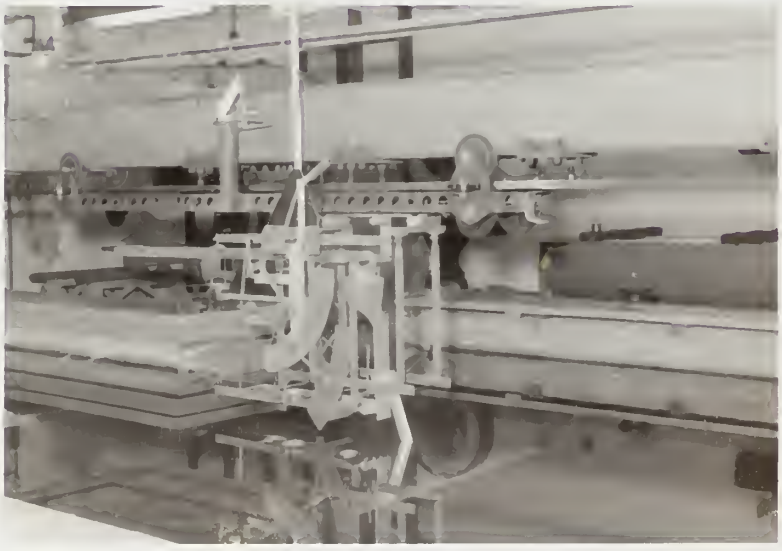

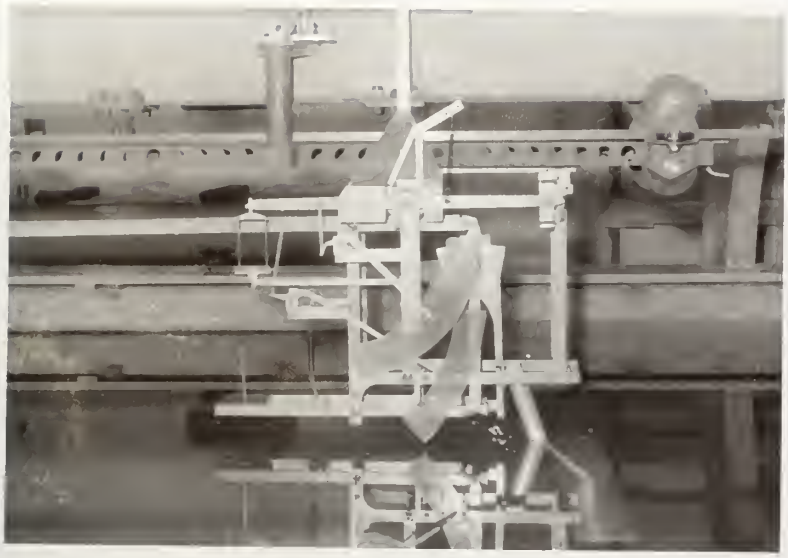

Figure 2

Balance with large foil attached as viewed from right side.

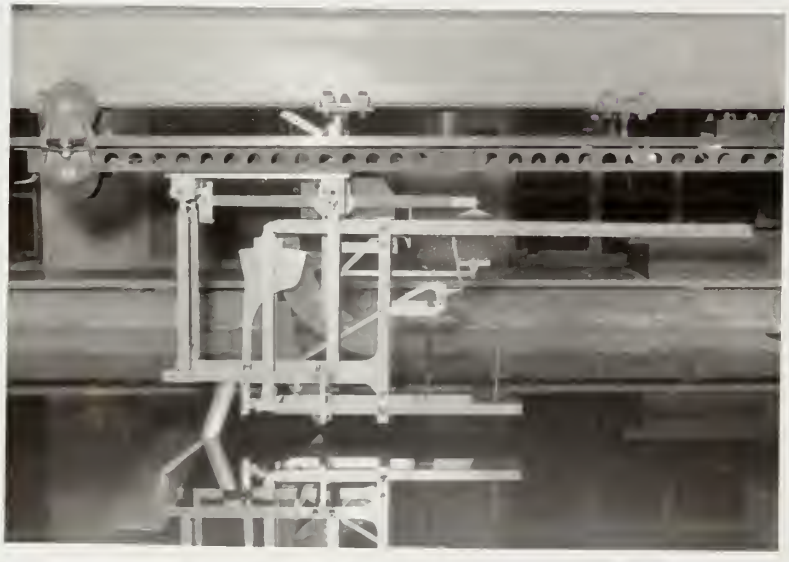

Figure 3

Balance with large foil attached as viewed from left side.

Now that confidence can be placed in the balance, previously non-essential alterations become highly desirable. These recommended alterations are explained in the text above and are here summarized.

Summary of Recommended Alterations

1. Increase scale legibility by

    a. Redesign and replace both lift and drag scales. The new scales should read from "0" at the lower extreme of pointer deflection, and the new drag scale should display a larger scale interval.

    b. Paint both pointer tips black.

2. Modify the angle of attack adjustment mechanism to include a vernier type movement.

3. Secure the drag pointer more firmly to its actuator arm.

4. Insure that the drag section stiffening bracket is performing its intended purpose, which is to rigidly fix the intersection of the two arms to which it is attached. Additional testing may show that the bracket should be enlarged, or that larger screws should be used to secure it to the arms of the drag section.

APPENDIX III

Stated simply, the problem facing the designer of the balance was to produce an instrument which could accurately measure small forces on a hydrofoil. This problem has heretofore precluded experiments of this type in all experimental model basins. Most tanks employ a strain gauge type balance for measuring hydrofoil forces. The advantages of this type of balance are obvious, however, its major disadvantage is relative inaccuracy. To insure good relative accuracy the forces measured must be large. This in turn dictates large foils and high speeds. Both of these factors produce high Reynolds numbers.

The balance as designed is sound, however, it must be emphasized that the adherence of the operator to a careful and rather detailed test procedure is mandatory. Due to the configuration, certain unavoidable errors in data will arise unless careful compensations are made. Although these compensations may seem trivial, the operator must bear in mind that errors of the order of magnitude of .005 pounds can produce scatter in the data at low speeds.

It is with future operators of the balance in mind that the authors have set forth here a detailed test procedure which the experience of over a thousand test runs indicates should produce the most reliable results.

TEST PROCEDURE

A. Preliminary Details

1. Bearings should be oiled and adjusted. Light machine oil in the tank equipment cabinet is adequate for this purpose. See Ref. 15 for a detailed description of the bearings and alignment procedures. This operation need not be performed before each testing period, however, periodic checks should be made.
2. All screw fastenings should be checked for tightness. Care must be exercised in tightening machine screws particularly where they are set in tapped holes in aluminum parts. Excessive force can strip the threads.
3. Make sure the bracket on the drag section T-arm is tight. Any play at this joint can produce erroneous readings. For a more detailed explanation of the reasons for these errors see Appendix II. It is also important to check this bracket frequently. Any errors in drag readings can generally be traced to this point.
4. Check the locking pins in the lift section bearings. These lock the upper arms to the shaft. They can work loose after many runs.

B. Assembly and Rigging of the Balance

1. Remove the counterbalance arm and loosen the top screws on the drag section spring holder so that the arm can be rotated to a horizontal position. Figure 1 shows the correct condition of the balance for placing it on the carriage.
2. Remove the lower rear wheel on the carriage to permit projections on the balance to pass this point. This wheel need not be replaced during testing, but must be replaced when tests have been completed. Figure 1

Figure 1

Placing balance on carriage

again shows this detail.

3. Slide the balance onto the carriage and secure the four locking screws. The fore and aft position of the balance is not critical provided the drag spring holder and counterbalance arm are clear. Figure 2 shows a good position. After the foil has been installed the balance can be rotated slightly to adjust the position of the foil so that its leading edge is normal to the towing line.
4. Secure the drag spring holder and counterbalance arms. Make sure the counterbalance arm is not canted either inboard or outboard. In the first case it will strike the timing switches on the tank and in the second case it may bind on the drag spring holder. It is essential that the counterbalance is rigidly attached, since any slight shift in the weight will produce errors in the drag readings. See Appendex II

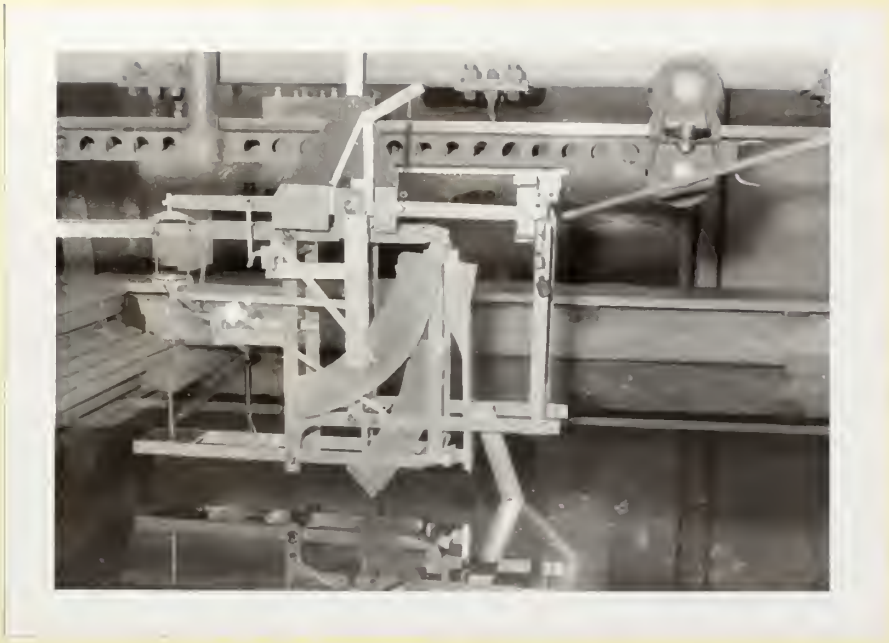

Figure 2

Drag calibration

for further details on this component.

5. Assemble the strut and hydrofoil. A detailed description of this assembly can be found in Ref. 15. Note that the spacers apply to one foil only. Again care should be exercised in tightening screws to avoid stripping the tapped threads in the strut. Before each testing period the strut and foil should be polished with some type of metal polish. The authors used "Doxon" aluminum polish. This will keep the surface condition as uniform as possible for all tests.
6. Install the strut and hydrofoil assembly. See Ref. 15 for details.

C. Calibration

1. Set the approximate angle of attack of the foil. The authors found that the most accurate method of accomplishing this calibration is with a standard Navy Gunner's Quadrant. The angle of attack of the

foil is actually measured by finding the strut angle. Sketch below indicates the method.

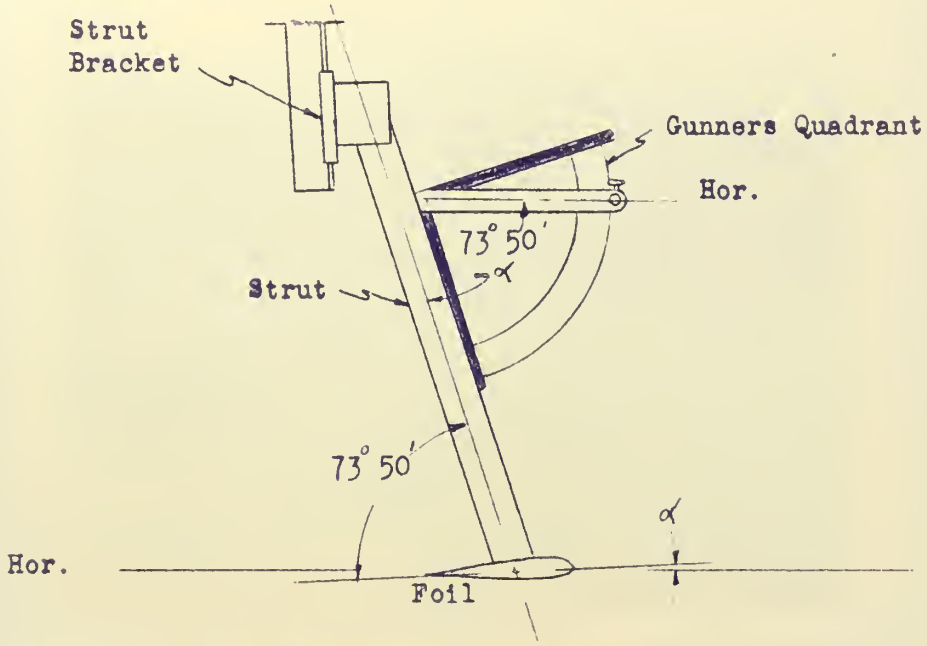

Figure 3 also shows the setting of angle of attack. Easiest method is with one man adjusting the foil angle and the other holding the Gunner's Quadrant. After the angle of attack has been set

Figure 3

Setting angle of attack

approximately, set the depth of foil. Figure 4 clearly shows this

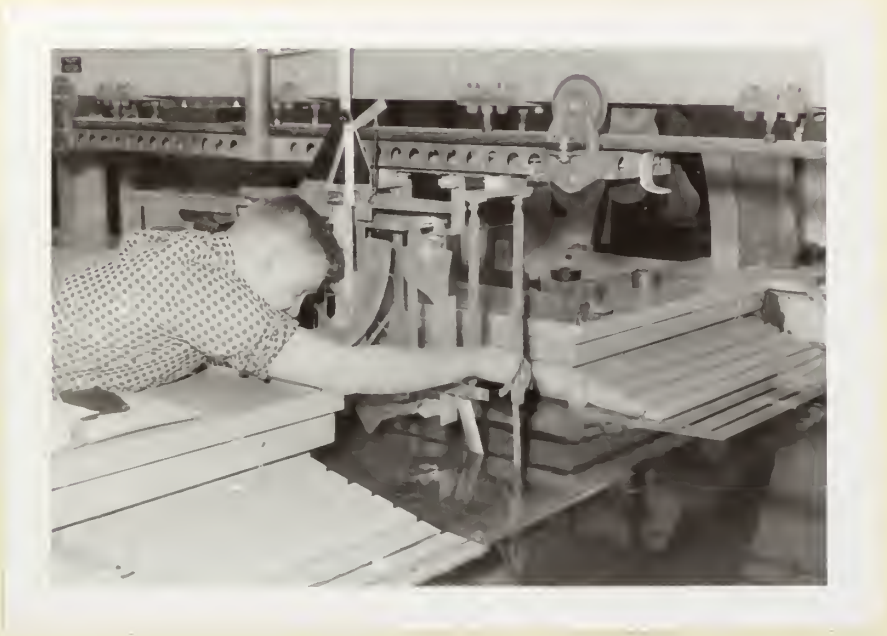

Figure 4

Setting depth

detail. Depth of foil is measured perpendicularly from the water surface to the midpoint of the intersection of the strut and the foil. After the depth has been set, make a final adjustment of the angle of attack. These operations must be performed before calibrating the lift and drag sections.

2. Install the springs on the lift and drag sections. For details, see Ref. 15. The size of spring depends on the size of the force to be measured and the accuracy desired. Although the lighter springs give better sensitivity they are more subject to the internal friction of the balance. The heavy springs were used almost exclusively on the lift section and often on the drag section. The light spring was used in the drag sections for measuring strut drag and drag on the

small foil at low angles of attack. The springs can be adjusted in tension by the use of adapters provided.

4. The drag section is clamped while calibrating the lift section. Adjust the lift counterbalance weight and the spring tension so that full scale readings can be made, however, in the unloaded condition the lift section should not touch the upper stop. Calibrating weights are placed on the knife edge as indicated in Figure 5. The position

Figure 5

Lift calibration

of the pan weights when testing is described in Ref. 15. Prior to actual calibration always make sure the pointer is zeroed and tightened. When measuring negative lift the spring tension and counterbalance weight are adjusted for full scale readings in the opposite direction. Calibrating weights are placed in the lift pan, and pan weights are placed on the pan provided at the opposite end of the lift arm.

The brass dowel for holding these weights can be seen in Figure 5 just below the calibration weights. It is not advisable to attempt to measure large negative lift forces, since the parallel motion feature of the balance is lost during this operation. Also the spring assists rather than balances a negative force.

5. The lift section is clamped when calibrating the drag section. Here again spring tension should be adjusted to give full scale readings, but at the same time it must not pull the T-arm against the upper stops. Calibrating weights are placed as indicated by the pointer in Figure 2. The pointer should be again zeroed and tightened. Probably the most important feature in the operation of the drag section is the effect of lift on drag readings. A lift force either positive or negative will produce a change in the drag reading. This can be readily demonstrated by placing a weight in the lift pan while the drag section is swinging free. During testing a positive lift force can be accurately balanced by a weight placed in the pan. For this reason lift data on the foil must be known before testing for drag. If the lift force is negative it cannot be balanced, and therefore must be corrected by calibration. To do this calibrate first with no lift force. Then insert a pan weight of the same magnitude as the maximum negative lift force to be expected and recalibrate. This procedure will give two calibration curves, describing the extreme conditions. During testing drag values can be interpolated from these curves for intermediate lift forces. This method can only be used for relatively small forces since the calibration curves will diverge too widely for large negative lift forces.

6. It is important to note that new calibration curves for both lift and drag must be drawn for each setting of angle of attack. Since the strut is raked forward, a change in angle of attack will produce a change in depth. When depth is reset to the correct value, a larger or smaller portion of the strut will be exposed, depending on the direction of change. This in turn will produce a shift in calibration curves due to a buoyancy change. When calibrating either the lift or drag section tap the balance or carriage lightly and oscillate the pointers. This tends to minimize frictional effects. The accuracies to be expected when testing are tabulated in Table 1 at the end of the Appendix.

D. Test Procedure

(This procedure is intended only as a supplement to standard procedures outlined for the Webb Towing Tank.)

1. When testing at high speeds a point will be reached when the spray roach from the strut begins to strike the strut plate. When this occurs data is no longer accurate.
2. Due to the light construction of the balance the authors feel lift forces should be limited to ten pounds.
3. Since lift data must be known before testing for drag, the authors found the best testing sequence was to test for lift first at a given angle of attack and then immediately test for drag at the same angle of attack. As previously mentioned each change in angle of attack requires recalibration. It is felt that this sequence reduces calibration time to a minimum.
4. Appendix I, sample calculations, shows method used by authors in

in recording rough data and reducing it to final form. There is one important point to be noted with regard to drag forces. A close look at the balance will reveal that the actual drag force is acting on a longer moment arm than the pan weights. For this reason pan weight forces must be multiplied by 0.87 to get actual drag forces.

Table 1

Accuracy of Lift and Drag Force Measurements

	Force Component	Type Spring	Accuracy
Strut	Drag	Light	± .004#
	Lift	Medium	± .005#
Small Foil	Drag	Light	± .0055#
	Drag	Medium	± .010#
	Lift	Medium	± .0055#
Large Foil	Drag	Medium	± .013#
	Lift	Medium	± .006#

The above table was obtained by averaging the slopes of all calibration curves used during testing. These slopes were in turn multiplied by a factor which included possible reading errors plus estimated frictional errors. It is felt that the accuracies err on the safe side and can be used as a guide for future experimentation. The springs described as light and

medium are sketched below.

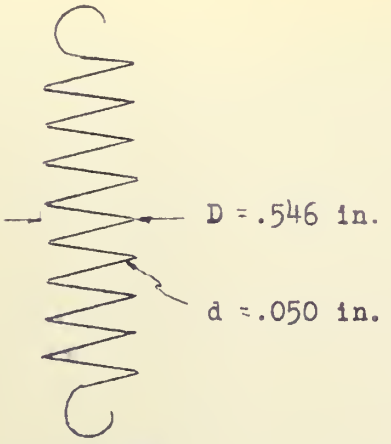

Medium

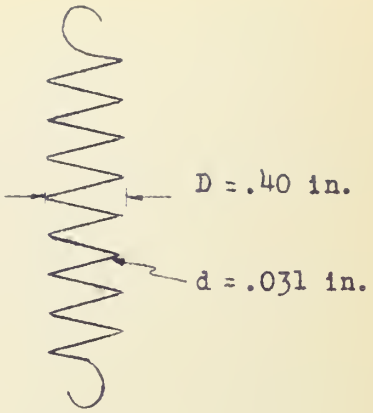

Light

Other Accuracy Factors

Angle of attack = 0.10 degrees

Depth of foil = 0.10 inches